LUND UNIVERSITY

Nanowire devices for X-ray detection

Chayanun, Lert

2020

Link to publication

Citation for published version (APA):
Chayanun, L. (2020). *Nanowire devices for X-ray detection*. [Doctoral Thesis (compilation), Faculty of Science]. Lund University.

Total number of authors:
1

General rights
Unless other specific re-use rights are stated the following general rights apply:
Copyright and moral rights for the publications made accessible in the public portal are retained by the authors and/or other copyright owners and it is a condition of accessing publications that users recognise and abide by the legal requirements associated with these rights.
- Users may download and print one copy of any publication from the public portal for the purpose of private study or research.
- You may not further distribute the material or use it for any profit-making activity or commercial gain
- You may freely distribute the URL identifying the publication in the public portal

Read more about Creative commons licenses: https://creativecommons.org/licenses/

Take down policy
If you believe that this document breaches copyright please contact us providing details, and we will remove access to the work immediately and investigate your claim.

LUND UNIVERSITY

PO Box 117
221 00 Lund
+46 46-222 00 00

Nanowire devices for X-ray detection

LERT CHAYANUN
DEPARTMENT OF PHYSICS | FACULTY OF SCIENCE | LUND UNIVERSITY

Printed by Media-Tryck, Lund 2020 NORDIC SWAN ECOLABEL 3041 0903

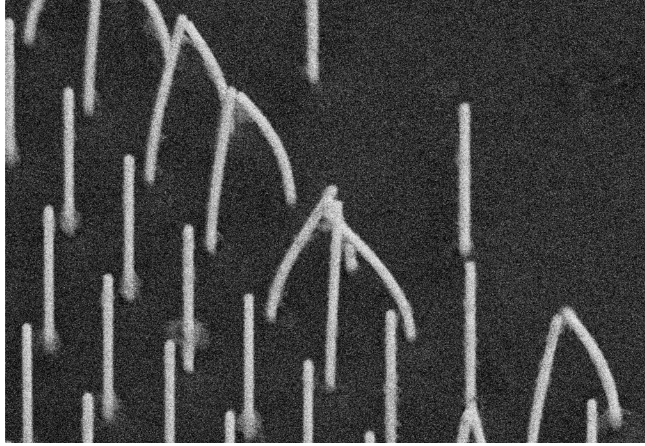

LUND UNIVERSITY

Faculty of Science
Department of Physics
Division of Synchrotron Radiation Research
Lund University
ISBN 978-91-7895-680-7

Nanowire devices for X-ray detection

Lert Chayanun

DOCTORAL DISSERTATION

by due permission of the Faculty Science, Lund University, Sweden.
To be defended on Friday, the 4th December, 2020, at 9:15 in the Rydberg lecture hall at the Department of Physics, Professorsgatan 1, Lund, Sweden.

Faculty opponent
Prof. Carsten Ronning

Institute of Solid State Physics, Friedrich-Schiller-University of Jena, Germany

Organization
LUND UNIVERSITY
Division of Synchrotron Radiation Research
Department of Physics, Box 118, SE-22100 Lund, Sweden
Author:Lert Chayanun

Document name
Doctoral thesis

Date of disputation
4 December 2020

Sponsoring organization

Title and subtitle Nanowire devices for X-ray detection

Abstract

High spatial resolution X-ray microscopy has become a dedicated tool to study nanocrystals and nanostructure devices in recent years. In general, the spatial resolution of X-ray microscopy depends on the spot size of the X-ray beam and the pixel size of X-ray detectors. High-resolution X-ray detection ideally requires a minimal active region with a sufficient thickness for the X-ray absorption, which leads to nanowire-shaped structures. This thesis made use of semiconductor nanowires to create a single-pixel X-ray detector at nanoscale resolution.

The basic interaction between X-rays and nanowire devices can best be investigated by choosing a sample geometry where the nanowire is oriented in-plane with the substrate and orthogonal to the beam. X-ray beam induced current (XBIC), which is the physical process used in X-ray detectors, was used as the primary method to investigate the electrical response from nanowire devices. Different aspects of the XBIC process were investigated in two nanowire materials, InP and InGaP, with two types of doping profiles, *n-i-n* and *p-i-n*.

The spectrally resolved XBIC measurements shed light on the underlying XBIC signal generation process in nanowire devices, showing that the XBIC signal originates at the atomic level with photoelectric absorption. Then, the X-ray flux variation revealed that the n^{+}-i-n^{+} doped InGaP nanowire devices were affected by charge trapping leading to photogating and photodoping effects. In contrast, both kinds of *p-i-n* doped nanowire devices illustrated a linear response as function of the X-ray photon flux, which makes this doping profile more suitable for X-ray detectors. The XBIC measurements of this thesis could reveal the spatially resolved charge collection efficiency (CCE) or internal quantum efficiency (IQE) of the nanowire device. This result emphasizes the key ability of XBIC to be used in the development of nanowire solar cells. Furthermore, calculations based on the finite element method (FEM) was used to get a better understanding of the XBIC results.

Although the in-plane nanowire devices can be used for understanding of the XBIC process at the nanoscale, they are not ideal for X-ray detection. The spatial resolution is still limited by the length of the active region, and the diameter of the nanowire limits the absorbing length. A novel fabrication process was therefore developed for a single vertical nanowire device where standing as-grown nanowires were turned into single pixel devices. With this configuration, the incident X-rays can be absorbed along the nanowire axis instead of the diameter. The nanowire used for this device is a *p-i-n* doped InP nanowire with a diameter of 60 nm as pixel size. Unlike the horizontal NW devices, the flux variation XBIC measurement reveals a sub-linear behaviour.

The vertical nanowire device was used to make a high-resolution 3D image of a 90 nm nanofocused X-ray beam by scanning the device in different planes along the beam. The measurements reveal details of the intensity distribution that agree well with calculations based on ptychography. Instead of the nanowire diameter, the spatial detection was limited to about 100 nm due to the stability of the measurement system and X-ray absorption in the top contact. In the future, the device design with as-grown nanowires could scale up into multi-pixel array detectors operating much like conventional X-ray detectors.

Key words Nanowires, Nanowire solar cells, X-ray detectors, X-ray beam induced current

Classification system and/or index terms (if any)

Supplementary bibliographical information		**Language** English
ISSN and key title		**ISBN** 978-91-7895-680-7 (print) 978-91-7895-681-4 (pdf)
Recipient's notes	**Number of pages** 156	Price
	Security classification	

I, the undersigned, being the copyright owner of the abstract of the above-mentioned dissertation, hereby grant to all reference sources permission to publish and disseminate the abstract of the above-mentioned dissertation.

Signature Lert Chayanun Date 2020-11-10

Nanowire devices for X-ray detection

Lert Chayanun

LUND
UNIVERSITY

Front cover: The SEM image shows nanowires in a dense array. The SiO_2 passivation layer and the Au particles were removed at the nanowire tips. These nanowires were used during the development of the fabrication process.

Back cover: The SEM image shows bending nanowires, forming an arc and a tent structure, after the isolation layer was removed.

Copyright pp. i-xii, 1-95, front cover, back cover (Lert Chayanun)

Paper 1 © published by IOP Publishing, CC-BY

Paper 2 © published by International Union of Crystallography (IUCr), CC-BY

Paper 3 © published by MDPI journals, CC-BY

Paper 4 © published by ACS Publications, CC-BY

Division of Synchrotron Radiation Research
Department of Physics, Faculty of Science
Lund University
SE-221 00, Lund
Sweden

ISBN:
978-91-7895-680-7 (print)
978-91-7895-681-4 (pdf)

Printed in Sweden by Media-Tryck, Lund University
Lund 2020

Media-Tryck is a Nordic Swan Ecolabel
certified provider of printed material.
Read more about our environmental
work at www.mediatryck.lu.se

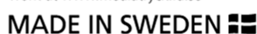

Abstract

High spatial resolution X-ray microscopy has become a dedicated tool to study nanocrystals and nanostructure devices in recent years. In general, the spatial resolution of X-ray microscopy depends on the spot size of the X-ray beam and the pixel size of X-ray detectors. High-resolution X-ray detection ideally requires a minimal active region with a sufficient thickness for the X-ray absorption, which leads to nanowire-shaped structures. This thesis made use of semiconductor nanowires to create a single-pixel X-ray detector at nanoscale resolution.

The basic interaction between X-rays and nanowire devices can best be investigated by choosing a sample geometry where the nanowire is oriented in-plane with the substrate and orthogonal to the beam. X-ray beam induced current (XBIC), which is the physical process used in X-ray detectors, was used as the primary method to investigate the electrical response from nanowire devices. Different aspects of the XBIC process were investigated in two nanowire materials, InP and InGaP, with two types of doping profiles, *n-i-n* and *p-i-n*.

The spectrally resolved XBIC measurements shed light on the underlying XBIC signal generation process in nanowire devices, showing that the XBIC signal originates at the atomic level with photoelectric absorption. Then, the X-ray flux variation revealed that the n^{+}-i-n^{+} doped InGaP nanowire devices were affected by charge trapping leading to photogating and photodoping effects. In contrast, both kinds of *p-i-n* doped nanowire devices illustrated a linear response as function of the X-ray photon flux, which makes this doping profile more suitable for X-ray detectors. The XBIC measurements of this thesis could reveal the spatially resolved charge collection efficiency (CCE) or internal quantum efficiency (IQE) of the nanowire device. This result emphasizes the key ability of XBIC to be used in the development of nanowire solar cells. Furthermore, calculations based on the finite element method (FEM) was used to get a better understanding of the XBIC results.

Although the in-plane nanowire devices can be used for understanding of the XBIC process at the nanoscale, they are not ideal for X-ray detection. The spatial resolution is still limited by the length of the active region, and the diameter of the nanowire limits the absorbing length. A novel fabrication process was therefore developed for a single vertical nanowire device where standing as-grown nanowires were turned into single pixel devices. With this configuration, the incident X-rays can be absorbed along the nanowire axis instead of the diameter. The nanowire used for this device is a *p-i-n* doped InP nanowire with a diameter of 60 nm as pixel size. Unlike the horizontal NW devices, the flux variation XBIC measurement reveals a sub-linear behaviour.

The vertical nanowire device was used to make a high-resolution 3D image of a 90 nm nanofocused X-ray beam by scanning the device in different planes along the

beam. The measurements reveal details of the intensity distribution that agree well with calculations based on ptychography. Instead of the nanowire diameter, the spatial detection was limited to about 100 nm due to the stability of the measurement system and X-ray absorption in the top contact. In the future, the device design with as-grown nanowires could scale up into multi-pixel array detectors operating much like conventional X-ray detectors.

Popular science

One of the most powerful tools in scientific research is X-rays. Similar to radio waves, microwaves, and visible or ultraviolet light, X-rays are also electromagnetic waves, but with a very short wavelength and high energy. The wavelength of X-rays can be as short as 0.01 nanometer (1 nm = 0.000 000 001 m), which is less than the size of atoms. The short wavelength allows the X-ray to penetrate through most kinds of materials. In addition, the X-ray energy can be as high as the binding energy of the electrons within atoms. With these properties, X-rays can interact with materials at the atomic level in a unique way.

X-rays are best known from their clinical applications, where they are used extensively to diagnose patients. Broken bones or cancer can be observed in patients using radiography and computing tomography (CT). Another example of X-ray applications is the use at security checks at airports. X-ray images from these applications originate from the different X-ray absorption of materials. The X-ray absorption can also lead to characteristic radiation, known as X-ray fluorescence, which has a unique energy for each element. However, the interaction between X-rays and materials is not limited only to the absorption. In the case of solid-state materials, the periodic atomic structure scatter X-rays at a certain angle, known as the Bragg angle, unveiling the crystal structure of materials. These interactions make X-rays a powerful tool for scientific research in many fields.

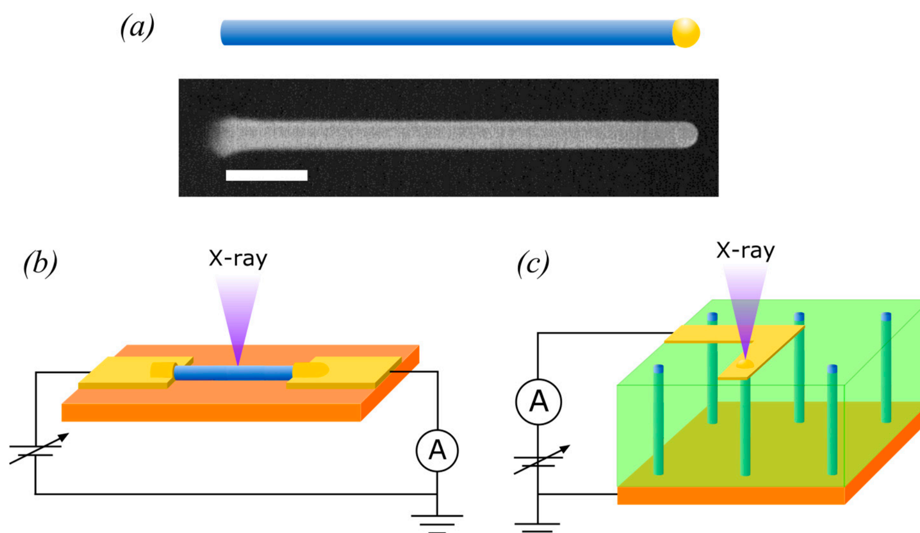

Figure 1 Scanning electron microscopy (SEM) images and schematic of semiconductors nanowires and nanowire devices. a) Single semiconductor nanowire. Scale bar 200 nm. The top schematic drawing shows the structure of the NW where there is a gold particle at one end. b) Horizontal single contacted nanowire device, in which there are metal contacts on both ends of the nanowire. c) Vertical single nanowire device with the metal top contact.

High spatial resolution X-ray images are required to observe small details of objects. For instance, a high-resolution CT scan could map a full three-dimensional neural network improving the understanding of how our brain and nervous system operate. This requires a small focused X-ray beam with an X-ray detector that has a relevant resolution. X-ray beams can be focused down to 5 nm by state-of-the-art X-ray lenses. However, X-ray detectors currently only have a resolution of about 0.5 micrometer (μm), which is a hundred times larger than the size of the focused X-ray beam.

The ideal high-resolution X-ray detection requires a minimal active area with a sufficient thickness for X-ray absorption. These requirements lead to a shape known as semiconductor nanowire. Nanowires are formed as a cylinder with a diameter from a few tens to a few hundreds of nm with a length that could be more than hundreds of μm. Figure 1(a) shows a scanning electron microscopy (SEM) image and schematic drawing of a nanowire. On the right side of this nanowire, there is a gold particle that was used in the nanowire synthesis. Due to their promising optical and electrical properties, nanowires have extensively been studied and developed for many advanced electronic devices, such as light emitting diodes (LED), lasers, transistors, photodetectors, and solar cells.

The first studies in this thesis use a nanowire device in a horizontal configuration where the nanowire was oriented in-plane to the surface, as shown in Figure 1(b). The horizontal nanowire devices were prepared by making metal contacts on both ends of the nanowire for electrical measurements. The interaction between nanowires and X-rays was evaluated in terms of an electrical response using the technique called X-ray beam induced current (XBIC). The XBIC measurement was done by scanning the sample through the X-ray beam. At each position of the scan, the X-ray beam would locally generate an electrical signal. The XBIC was measured as a function of time, X-ray energy, X-ray photon flux (photons per second), and applied voltage on the nanowire. Three kinds of nanowires, which have different material compositions, were investigated in the studies. In turn, XBIC could also reveal spatially resolved functionalities of those nanowire devices, such as generation and collection mechanisms of the induced signal.

With the horizontal nanowire devices as X-ray detectors, the spatial resolution and the absorption length is still limited by nanowire's length and diameter, respectively. However, nanowire devices can be made in a vertical configuration, where a standing as-grown nanowire is turned into a device, as shown in Figure 1(c). The nanowire is parallel to the X-ray beam during the measurement. With this configuration, the diameter of the nanowire limits the spatial resolution of the measurement. Furthermore, X-ray absorption can take place through the length of the nanowire instead of the diameter in the horizontal nanowire device. Consequently, both higher spatial resolution and higher X-ray absorption can be expected from vertical nanowire devices for X-ray detectors.

The vertical nanowire devices were fabricated from nanowires with a diameter of 60 nm, and were tested by mapping them in a 90 nm-diameter focused X-ray beam. Then, the vertical nanowire device was used to two-dimensionally scan various planes along the optical axis resulting in a high-resolution 3D image of the X-ray beam. The result showed the distribution of the beam intensity, which has never been measured at this length scale before. In the future, these devices could be made with even smaller diameters for higher spatial resolution, and formed into arrays for multi-pixel devices.

List of publications

This thesis is based on the following publications, which will be referred to as Paper I – IV:

I. Spectrally resolved X-ray beam induced current in a single InGaP nanowire

L. Chayanun, V. Dagyte, A. Troian, D. Salomon, M. T. Borgström, J. Wallentin, *Nanotechnology* **29** (2018) 454001
DOI: https://doi.org/10.1088/1361-6528/aadc76

I was responsible for analysing the data and for writing the paper.

II. Nanoscale mapping of carrier collection in single nanowire solar cells using X-ray beam induced current

L. Chayanun, G. Otnes, A. Troian, S. Hammarberg, D. Salomon, M. T. Borgström, J. Wallentin, *Journal of Synchrotron Radiation* **26** (2019) 102-108
DOI: https://doi.org/10.1107/S1600577518015229

I fabricated the horizontal nanowire devices and performed the experiment at the synchrotron facility. I was also responsible for analysing the data and for writing the paper.

III. Combining Nanofocused X-Rays with Electrical Measurements at the NanoMAX Beamline

L. Chayanun, S. Hammarberg, H. Dierks, G. Otnes, A. Björling, M. T. Borgström, J. Wallentin, *Crystals* **9** (2019) 432
DOI: https://doi.org/10.3390/cryst9080432

I fabricated the horizontal nanowire devices and performed the experiment at the synchrotron facility. I was responsible for analysing the STXM, XRF, and XBIC data, and for writing the paper.

IV. Direct 3D imaging of an X-ray nanofocus using a single 60 nm-diameter nanowire device

L. Chayanun, L. Hrachowina, A. Björling, M. Borgström, J. Wallentin, *Nano Letters* (In press)
DOI: https://dx.doi.org/10.1021/acs.nanolett.0c03477

I designed and fabricated the vertical nanowire devices for the experiment. I was the main responsible for the experiment at the synchrotron facility. I was also responsible for analysing the data and for writing the paper.

Papers not included in this thesis, to which I have contributed:

V. Nanobeam X-ray fluorescence dopant mapping reveals dynamics of in situ Zn-doping in nanowires

A. Troian, G. Otnes, X. Zeng, L. Chayanun, V. Dagyte, S. Hammarberg, D. Salomon, R. Timm, A. Mikkelsen, M. T. Borgström, J. Wallentin, *Nano Letters* **18** (2018) 6461–6468
DOI: https://doi.org/10.1021/acs.nanolett.8b02957

VI. High resolution strain mapping of a single axially heterostructured nanowire using scanning X-ray diffraction

S. Hammarberg, V. Dagyte, L. Chayanun, M. O. Hill, A. Wyke, A. Björling, U. Johansson, S. Kalbfleisch, M Heurlin, L. J. Lauhon, M. T. Borgström, J. Wallentin, *Nano Research* **13** (2020) 2460-2468
DOI: https://doi.org/10.1007/s12274-020-2878-6

List of recurrent abbreviations and symbols

ALD	atomic layer deposition
BOE	buffered oxide etch
CCE	charge collection efficiency
DIP	dual in-line pin
DPC	differential phase contrast
EBIC	electron beam induced current
EBL	electron beam lithography
EQE	external quantum efficiency
ESRF	European synchrotron radiation facility
EXAFS	extended X-ray absorption fine structure
FEM	finite element method
FWHM	full width half maximum
IPA	isopropyl alcohol
IQE	internal quantum efficiency
I-V	current – voltage
KB	Kirkpatrick-Baez
LED	light emitting diode
MIBK	methyl isobutyl ketone
MOCVD	metalorganic chemical vapor phase deposition
MZP	multilayer zone plate
NIL	nano-imprint lithography
NW	nanowire
OSA	order sorting aperture
PCB	printed circuit board
PMMA	polymethyl methacrylate
RIE	reactive ion etch
SD	standard deviation
SEM	scanning electrical microscope
SPCM	scanning photocurrent microscopy
SRH	Shockley-Read-Hall
STXM	scanning X-ray transmission microscopy
XANES	X-ray absorption near edge spectroscopy
XAS	X-ray absorption spectroscopy

XBIC	X-ray beam induced current
XRD	X-ray diffraction
XRF	X-ray fluorescence
p_{abs}	X-ray absorption probability
η	Electron-hole pair generation yield
Φ	X-ray photon flux

Acknowledgment

First of all, I would like to thank Jesper Wallentin for his dedicated work as the main supervisor. I have learned a good practice in research and science from him through many discussions during the past years. I am very thankful for his help with writing papers and this thesis. In addition, his advice regarding my future career after the Ph.D. study is very appreciated.

I would like to thank my co-supervisor, Magnus Borgström, and the great support from his group at NanoLund, Lund University, Sweden. The first part of this thesis could not be done without nanowires from Vilgaile Dagyte and Gaute Otnes. Their inputs from nanowire characteristics are very useful for my work. Thank you Yuwei Zhang to teach me several nanofabrication processes that have been used to develop the vertical nanowire device. Furthermore, I would like to thank Lukas Hrachowina for his help with the nanowire synthesis for the vertical nanowire device and the EBIC measurement.

I very much appreciate the help from Rainer Timm, my second co-supervisor, for his help in administration and reviewing this thesis.

Thank you Susanna Hammarberg, Andrea Troian, and Hanna Dierks for being part of my experiment and being my co-authors. I very much appreciate the support from the beamline scientists, Damien Salomon at ID-16B, ESRF, France, and Alexander Björling at the NanoMAX beamline, MAX IV, Sweden.

It is my pleasure to have had experiments at the P10 beamline, PETRA III, Germany, in collaboration with Markus Osterhoff and Jakob Soltau from Tim Salditt's group at the Institute of X-ray physics, University of Göttingen, Germany.

I would also acknowledge the great support from all of the staff at Lund Nano Lab, Lund University, Sweden, who made sure that I always have operating machines in the cleanroom for device processing.

Moreover, I would like to thank Patrik Wirgin and Anne Petersson Jungbeck for their administration work. Thank you Yen-Po Liu, Yi Liu, Foqia Rehman, and other fellow Ph.D. students for a great time at Synchrotron radiation research, Lund University, Sweden.

Finally, I would like to thank my wife, my son, and my family for their indulgence and for always being there for me.

Table of Contents

Abstract ..... **i**

Popular science ..... **iii**

List of publications ..... **vi**

List of recurrent abbreviations and symbols ..... **viii**

Acknowledgment ..... **x**

1 Introduction **1**

2 X-ray detectors **5**

2.1 X-rays and refractive index 5

2.2 X-ray absorption 7

2.2.1 X-ray fluorescence (XRF) 8

2.2.2 X-ray absorption spectroscopy (XAS) 9

2.2.3 Photogenerated secondary electrons in semiconductors 11

2.3 Semiconductor photodetectors 12

2.3.1 Photoconductors 14

2.3.2 Photodiodes and *p-n* junctions 14

2.4 Indirect and direct X-ray detectors 17

3 Nanowire device fabrication and preliminary evaluation **19**

3.1 Nanowire synthesis 19

3.2 Horizontal single contacted nanowire devices 20

3.2.1 Predefined Si_3N_4 membrane substrate 21

3.2.2 Metal contacts for a single horizontal nanowire 23

3.3 Vertical single contacted nanowire devices 25

3.3.1 Large pitch array for NW growth using EBL 25

3.3.2 Nanowire passivation and isolation layer 26

3.3.3 Bond pads and top contacts 28

3.4 Chip mounting and wire bonding 30

3.5 Preliminary device characterization 31

3.5.1 Electron beam induced current (EBIC) measurement 31

3.5.2 Electrical characterization with a probe station 32

3.5.3 Simplified photocurrent measurement ... 32

4 X-ray characterization methods ... 35

4.1 X-ray beam induced current (XBIC) ... 35

4.1.1 XBIC measurement system ... 36

4.1.2 Internal electronic noise in the XBIC measurement system ... 38

4.2 Complementary X-ray methods ... 39

4.2.1 Scanning transmission X-ray microscopy (STXM) ... 39

4.2.2 Scanning X-ray fluorescence (XRF) ... 40

4.2.3 Scanning X-ray diffraction (XRD) ... 40

4.3 Synchrotron radiation sources and beamlines ... 42

4.3.1 ID16B beamline, ESRF, Grenoble, France ... 42

4.3.2 NanoMAX beamline, MAX IV, Lund, Sweden ... 43

4.3.3 P10 beamline, PETRA III – DESY, Hamburg, Germany ... 43

4.4 Finite element method (FEM) with Comsol ... 45

5 X-ray characterization results ... 47

5.1 Simultaneous XBIC and XRF imaging ... 47

5.1.1 Horizontal single contacted nanowire devices ... 47

5.1.2 Vertical *p-i-n* doped InP nanowire devices ... 49

5.2 Spectrally resolved XBIC and XRF ... 50

5.3 X-ray photon flux variation ... 51

5.3.1 Photogating and photodoping in n^+-*i*-n^+ doped nanowire device ... 51

5.3.2 Escaping secondary electrons in horizontal *p-i-n* doped nanowire devices ... 52

5.3.3 Sub-linear XBIC behaviour with X-ray photon flux variation ... 54

5.4 Bias dependent XBIC and spatial charge collection efficiency (CCE) ... 55

5.5 Finite element method modelling of XBIC ... 56

5.6 Axial XBIC distribution and carrier transport ... 57

6 Imaging of nanofocused X-rays using nanowire devices ... 59

6.1 MZP focus measured with a horizontal nanowire ... 59

6.2 3D imaging of the NanoMAX focus ... 61

7 Conclusion and outlook ... 65

8 References ... 69

1 Introduction

One of the most useful tools in scientific research is X-rays, which is used to study advanced materials down to the atomic level. X-rays, which are electromagnetic waves with relatively high energy (1-100 keV), were discovered and named by Wilhelm Röntgen in 1895 [1]. Later, he was awarded the first Nobel prize in physics in 1901 for this discovery. Since then, X-rays have been applied in clinical use with radiography and later tomography. Thanks to the difference in X-ray absorption between bones and soft tissue, radiography helps doctors to diagnose patients in vivo observing bone and internal organs. In terms of solid materials, the diffraction of X-rays was key for understanding the crystalline structure with Bragg's law and the Laue equation. Finally, the high energy of X-rays is also sufficient to interact with the core electron states of atoms, which can be investigated by controlling the energy of the exciting and emitted X-rays. This method is called X-ray spectroscopy and was pioneered by Manne Siegbahn during his time at Lund University.

The examples mentioned above of X-rays' applications are based on four main interactions between X-rays and matter: photoelectric absorption, Thomson (elastic) scattering, Compton (inelastic) scattering, and pair production [2]. In photoelectric absorption, the X-ray energy is absorbed by an inner core electron of an atom, exciting this core electron from the atom through photoelectric emission. Alternatively, an X-ray photon can scatter with an electron bound to the atom. In the elastic scattering, the X-ray photon energy is unchanged after the scattering. In contrast, some of the energy of the X-ray photon is transferred to an electron in the inelastic scattering. Finally, very high energy X-rays can lead to pair production of an electron and its antiparticle, a positron.

In the discovery of W. Röntgen, the X-rays originated in his electrical experiment with a vacuum tube, and later this kind of generation source became known as an X-ray tube. Electrons are emitted from the cathode of the X-ray tube and hit the target material at the anode to generate X-rays. Nowadays, X-ray tubes are still used in laboratories and hospitals. Much more powerful X-ray beams are generated from large facilities known as synchrotrons. The radiation is generated by electrons traveling at a relativistic speed, which are forced to travel along a curved path by magnetic fields [2]. Synchrotron radiation sources have become one of the backbones of modern scientific research during the past decades. For instance, the wide range of X-ray energy from synchrotrons allows us to investigate a broader

range of atomic structures and interactions, advancing the development of materials, electronic devices [3], and medicine [4].

The demand for improved spatial resolution of X-ray microscopy is increasing due to the substantial interest in nanostructured materials [5-11]. High-resolution X-ray imaging for studies of nanostructures requires X-ray nanofocusing methods, which is challenging due to the weak interaction between X-rays and focusing optics. Despite these difficulties, nanofocused X-ray beams can be achieved thanks to the development of Kirkpatrick-Baez (KB) mirrors and zone plates, which have been used for focusing X-ray beams to less than 5 nm in state-of-the-art experiments [12,13]. There are now many synchrotron beamlines that can routinely deliver nanofocused X-ray beams below 100 nm [13-16].

High-resolution X-ray imaging also creates challenges for X-ray detection. The first type of X-ray detectors – indirect X-ray detectors – uses scintillators to convert X-rays into lower-energy light before converting into an electronic signal. The spatial resolution is theoretically limited to about 0.5 μm [17] due to the Abbe diffraction limit of the lower-energy light. The second type of X-ray detectors – direct X-ray detectors – converts the absorbed X-ray photon directly into an electrical signal. For commercial direct X-ray detectors, the pixel size is limited to about 50 – 200 μm [18-20] due to the electrical components necessary for each pixel.

Since X-rays can penetrate through a lot of material, apart from a minimal pixel area, the ideal high-resolution X-ray detector should also have a sufficient thickness to absorb the X-rays. The two challenging requirements of a small cross-section but a large thickness along the optical axis lead to a nanowire-shaped structure of the pixels.

Semiconductor nanowires (NWs) have a cylindrical shape with a diameter of a few tens to a few hundreds of nm, and a length that is almost unlimited [21]. This geometry of NWs is considered as a one-dimensional nanostructure, which makes optical and electrical properties of NWs different from bulk materials. Various material compositions are available in NWs, which can be synthesized on a reusable substrate reducing the cost of manufacturing [22,23]. These properties make NWs a promising building block of advanced electronic devices, such as quantum devices [24], light emitting diodes (LED) [25,26], transistors [27-29], lasers [30,31], photodetectors [32-34], and solar cells [35-38].

The same mechanism as in direct detectors can also be used to characterise materials in the X-ray microscopy technique called X-ray beam induced current (XBIC) [39,40]. There are only a few studies of NWs using XBIC aside from this work [9,41,42], although XBIC has been used extensively to study materials for solar cells [43-45]. The results of the early XBIC studies on single NW devices show that, despite a small volume of X-ray absorption, NW devices still have a strong electrical response to hard X-ray exposure. The NWs studied in ref. [41] were n^+-i-n^+ doped InP NWs, which were turned into a horizontally single contacted NW device, such

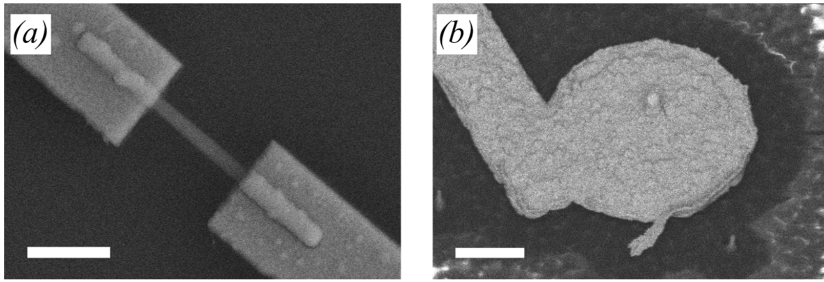

Figure 1-1 SEM images of a single NW device for X-ray detectors: a) Horizontal (in-plane) configuration and b) Vertical configuration. The scale bars are 1 μm.

as the one shown in Figure 1-1(a). With this in-plane configuration, a single NW is oriented parallel with the substrate. The XBIC signal from this NW device showed a long saturation time with the X-ray exposure due to the charge trapping at surface states, which could also lead to photogating and photodoping effects [46]. Nonetheless, that study demonstrated the possibility of the single NW device to image nanofocused X-rays.

The main question of this thesis is how NW devices could be further improved for high-resolution X-ray detection. To answer this question, XBIC measurements have been employed as a primary tool to further enhance the understanding of the electrical interaction between X-rays and NW devices. First, NW devices similar to the one in ref. [41] – horizontal single contact n^{+}-i-n^{+} doped InGaP NW devices – were studied with the spectrally resolved measurement of XBIC and XRF to shed light on the underlying atomic process of the XBIC signal (Paper I).

Then, the NWs were modified to a *p-i-n* doping profile, which is extensively used in nanowire photodetectors [32-34] and solar cells [35-38]. The time-resolved and flux variation XBIC measurements revealed a better electronic response from the *p-i-n* doped NW devices (Paper II). In addition, the measurements with applied bias dependence showed the ability of the XBIC technique to spatially resolve the charge collection efficiency (CCE), which is related to the internal quantum efficiency (IQE), in the study of NW solar cells. Simulations based on the finite element method (FEM) also helped to understand the carrier collection mechanism of XBIC results from these NWs.

Due to the geometry of horizontal NW devices, the resolution of the X-ray detection was still limited by the active region along the length of the NW, and the absorption was limited to the nanowire diameter. Another aim in this thesis was therefore to take advantage of the NW geometry to further improve the spatial resolution. Hence, the vertical configuration (Figure 1-1(b)) was developed, as demonstrated in Paper IV. With the vertical NW device, the spatial resolution of the detector will be limited by the diameter of the NW, and the X-rays can be absorbed along the NW axis. Moreover, the device design with as-grown NWs could scale up into a multi-pixel array detector similar to those conventional X-ray detectors.

To give an overview of the thesis, the general concept of X-ray detectors is described in chapter 2, which includes the interaction between X-rays and materials, the charge generation, and the charge collection processes of the detectors. Then, chapter 3 shows the fabrication processes of the NW devices. In this chapter, the more challenging process to fabricate vertical NW devices with the NW diameter of about 60 nm is discussed. The preliminary characterization of the devices is also included in this chapter. After that, the XBIC measurement method, as well as the multimodal X-ray imaging at different synchrotron beamlines (Paper III), is discussed in chapter 4. This chapter also describes how FEM was used for the XBIC simulation.

Chapter 5 presents the XBIC results from the investigation of both single horizontal and vertical NW devices to get a better understanding of the X-ray interaction with NW devices. The results demonstrating the NW device for X-ray detections are presented and discussed in chapter 6, where both horizontal and vertical NW devices were used to map the nanofocused X-ray beams. In the case of horizontal NW devices, the beam waist from the off-axis multilayer zone plate (MZP) was two-dimensionally mapped. Then, the vertical single NW device three-dimensionally mapped the intensity of the focus from the KB mirrors at the NanoMax beamline, MAX IV synchrotron (Paper IV). Finally, chapter 7 contains the conclusions of this thesis as well as the outlook for future development.

2 X-ray detectors

After the X-ray discovery, a phosphor screen or film was used to collect the X-rays, similarly to how W. Röntgen acquired his first X-ray image. Nowadays, digital X-ray detectors have become standard. A digital X-ray detector allows X-ray images, such as STXM, computed tomography (CT) and ptychography, to be analyzed in real-time.

In this chapter, some background of relevant X-ray interactions and how photodetectors operate are introduced, before discussing X-ray detectors. Digital X-ray detectors can be separated into two categories according to the underlying process: indirect and direct X-ray detectors. Although the main focus of this thesis is direct X-ray detectors, indirect X-ray detectors will be briefly mentioned in this chapter as well. These concepts are crucial to understand electrical performance and X-ray response of the developed NW devices later in this thesis.

2.1 X-rays and refractive index

X-rays are electromagnetic radiation like radio waves, infrared, ultraviolet, and visible light. The wavelength, λ, of X-rays is in the range of 10 nanometers down to 0.1 Ångström (10 nm – 0.1 Å). From a quantum perspective, the energy of electromagnetic radiation is quantized in particles named photons. The wavelength of X-rays corresponds to photon energies of 1 keV to 100 keV, according to the equation $E = hc/\lambda$, where h is Planck's constant (h = 6.262×10^{-34} J·s) and c is the speed of light in vacuum ($c \approx 3\times10^{8}$ m/s).

The speed of electromagnetic waves, the phase velocity, v, in materials deviates from the speed of light, c, by the refractive index, $n = c/v$, of that particular material. In general, electromagnetic waves have a *normal dispersion*, with n higher than 1. In contrary, n is less than unity for X-rays [2]. This makes the phase velocity, v, higher than c. However, the envelope of the electromagnetic wave travels with the *group velocity*, which is still less than c. Thus, the law of relativity is not violated.

The refractive index of matter, n, in the case of X-rays, relates to the scattering and the absorption properties of the medium represented by δ and β, respectively. Therefore, n can be written as:

$$n \equiv 1 - \delta + i\beta \tag{1}$$

Both δ and β are positive and small since X-rays generally interact weakly with matter. Alternatively, the refractive index can be defined in term of the atomic form factor as:

$$n \equiv 1 - \frac{2\pi\rho_{at}r_0}{\mathrm{k}^2}\{f^0(0) + f' + if''\} \tag{2}$$

where ρ_{at} is the atomic density, and r_0 is Thomson scattering length. The atomic form factor determines the scattering amplitude of X-rays by an atom. Here, $f^0(0)$ is the atomic form factor in the case that the scattered wave from an atom with wavevector, $\mathbf{k}'$, has the same direction as the incident wavevector, $\mathbf{k}$, so that the scattering vector is $\mathbf{Q} = \mathbf{k} - \mathbf{k}' = 0$. f' and f'' are the real and imaginary parts of the dispersion corrections to the atomic form factor, where f' is related to the scattering from the bound electron and f'' represents the absorption [2]. Combining the above equations, δ and β can be expressed as

$$\delta = \frac{2\pi\rho_{at}r_0}{\mathrm{k}^2}f^0(0) \tag{3}$$

$$\beta = -\left(\frac{2\pi\rho_{at}r_0}{\mathrm{k}^2}\right)f'' \tag{4}$$

The following section shows how to derive the absorption coefficient, μ, of materials from the absorption part of the refractive index, β (eq. (4)).

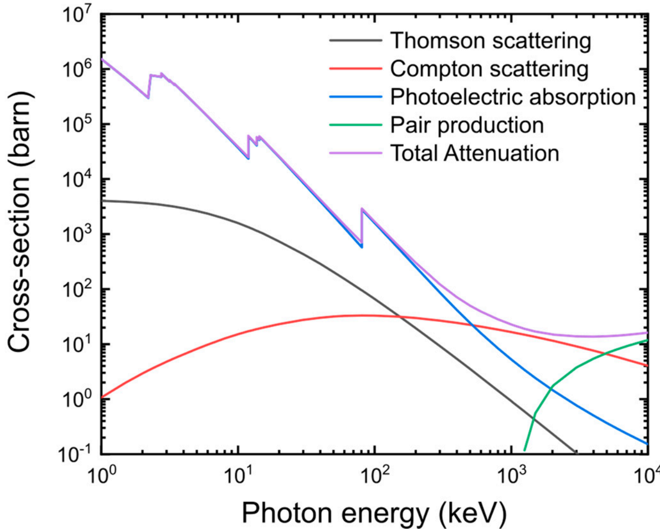

Figure 2-1 Thomson scattering (black), Compton scattering (red), Photoelectric absorption (blue), pair production (green) and the total attenuation (purple) cross-sections of Au in barn (1 barn ≡ 10^{-24} cm^2) from the database website https://physics.nist.gov/PhysRefData/Xcom/html/xcom1.html.

2.2 X-ray absorption

The atomic cross-section, measured in barn (1 barn ≡ 10^{-24} cm^2), of the four main interactions between X-rays and matters – 1) photoelectric absorption, 2) elastic scattering, 3) inelastic scattering, and 4) pair production – is shown in Figure 2-1. Note that the relevant energy range in this thesis is 10 – 20 keV. From these four interactions, this thesis only focuses on photoelectric absorption, which is relevant to the XBIC measurement and the operation of the X-ray detector. Further information on the other processes can be found elsewhere [2].

The absorption cross-section of an element is approximately proportional to $\sigma \sim Z^4/E^3$, where Z is the atomic number and E is the X-ray photon energy. Therefore, materials with a higher atomic number absorb more X-rays, especially at low energy.

In an experiment it is often important to be able to calculate the X-ray transmission through a sample (Paper I – IV). The change in intensity (absorption) of the X-rays at depth z from the surface, $I(z)$, in an infinitesimal sheet of thickness dz can be expressed as

$$dI = -I(z)\mu dz \tag{5}$$

where μ is the absorption coefficient. This equation is solved with the boundary condition $I(z = 0) = I_0$, so the X-ray intensity transmitted through the sample is

$$I(z) = I_0 e^{-\mu z} \tag{6}$$

This equation is known as the Beer-Lambert's law in which the ratio between $I(z)$ and I_0 is the transmission, $T(z) = I(z)/I_0 = e^{-\mu z}$. Hence, the X-ray absorption probability is defined as $p_{abs} = 1 - e^{-\mu z}$, which is extensively used throughout this thesis (Paper I – IV). In case of a very thin sample, $\mu z \ll 1$, eq. (6) can be approximated as $I(z) \approx I_0(1 - \mu z)$ and $p_{abs} \approx \mu z$.

Since $\beta \mathrm{k} = \mu/2$ [2], eq. (4) becomes

$$\mu = -\left(\frac{4\pi\rho_{at}r_0}{\mathrm{k}}\right)f'' \tag{7}$$

For a compound consisting of j atom types, the absorption coefficient, μ, can be calculated as the product of the respective atomic densities, $\rho_{at,j}$, and the atomic absorption cross-sections, σ_j:

$$\mu = \sum_j \rho_{at,j}\, \sigma_j \tag{8}$$

Therefore,

$$\mu = \left(\frac{4\pi r_0}{\mathrm{k}}\right) \sum_j \rho_{at,j}\, f_j'' \quad (9)$$

Eq. (9) is used to calculated μ for different materials of the studied NWs, and then used to attain p_{abs} as discussed above.

2.2.1 X-ray fluorescence (XRF)

Upon the X-ray absorption at the atomic level, an inner shell electron of an atom is excited, emitting a high energy electron and leaving a vacant state called a core hole. This process is known as the photoelectric emission (Figure 2-2). The core hole is then filled by relaxation of a second, higher state, electron. Consequently, there is an emission of excessive energy, which can be in the form of a lower energy secondary X-ray photon, known as X-ray fluorescence (XRF). This XRF emission is more efficient for heavy elements [47]. Alternatively, the excess energy can excite a third electron in the outer shell of the atom, which is known as Auger electron emission (Figure 2-2).

Each transition between different energy states of the XRF process results in a specific energy of the XRF photon, which is also characteristic for the element. The Siegbahn notation is used to define each of these XRF transitions. The XRF energy of various transitions of elements and their relative intensities can be found in the X-ray data booklet [48].

Figure 2-3 shows the XRF spectrum measured from a vertical nanowire device, using an X-ray energy of 10 keV. The spectrum reveals the energy of the electronic

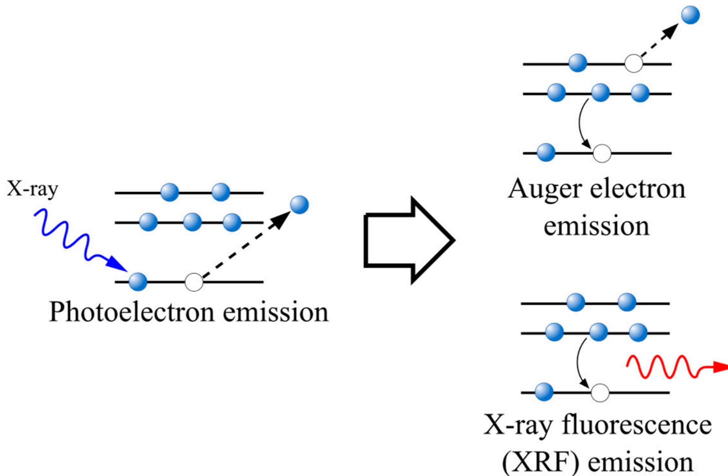

Figure 2-2 Photoelectric absorption. The X-ray absorption excites an inner core electron of an atom which results in a photoelectron emission. Consequently, there is a vacant state, called a core hole. The relaxation of an electron from a higher state fills the core hole. This process releases excess energy, either in the form of a lower energy X-ray photon, X-ray fluorescence (XRF), or excitation and emission of a higher state electron, Auger electron emission.

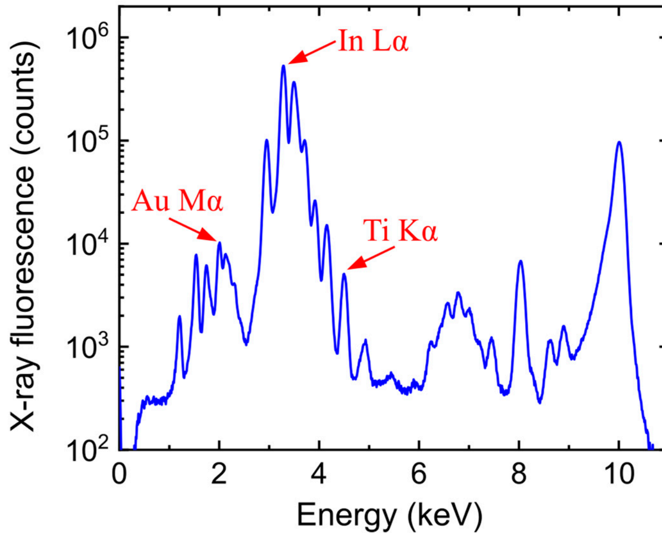

Figure 2-3 X-ray fluorescence (XRF) spectrum from a nanowire device. Multiple peaks in the spectrum correspond to various transitions in elements inside the sample. This spectrum was attained by the use of a 10 keV X-ray beam. Au M_α and Ti K_α are emitted from metal contacts of the nanowire device, and In L_α comes from the InP substrate.

transition from various elements within the sample. For instance, the XRF emission from the In L_α transition, which comes from the NW and the InP substrate, appears as a peak at about 3.28 keV. The emission from Au M_α and Ti K_α transitions at 2.12 keV and 4.51 keV, respectively, can also be observed. These elements are part of the metal contacts in the vertical NW devices (Paper IV). The rightmost peak corresponds to the scattered incident X-ray beam.

The intensities of these peaks on the XRF spectrum (Figure 2-3) can be used to determine the relative or even the absolute concentration of the measured elements. For instance, the intensity of In L_α in Figure 2-3 is relatively higher than Au M_α and Ti K_α, since there is much more absorption in the InP substrate than the 20 nm/200 nm thick Ti/Au layer in the metal contact. The absolute concentration from the XRF spectrum could be attained by considering the XRF yield, air absorption, and the quantum efficiency of the detector. By scanning the sample in a focused beam, the spatial distribution of elements can be imaged. Details of this scanning XRF method will be mentioned later in section 4.2.2.

2.2.2 X-ray absorption spectroscopy (XAS)

The photoelectron emission can occur when the exciting X-ray energy is higher than the binding energy of an electron, and the X-ray energy therefore affects the absorption cross-section. This can be observed as a step in the spectrum in X-ray absorption spectroscopy (XAS), as shown in Figure 2-1. The energy at this step is

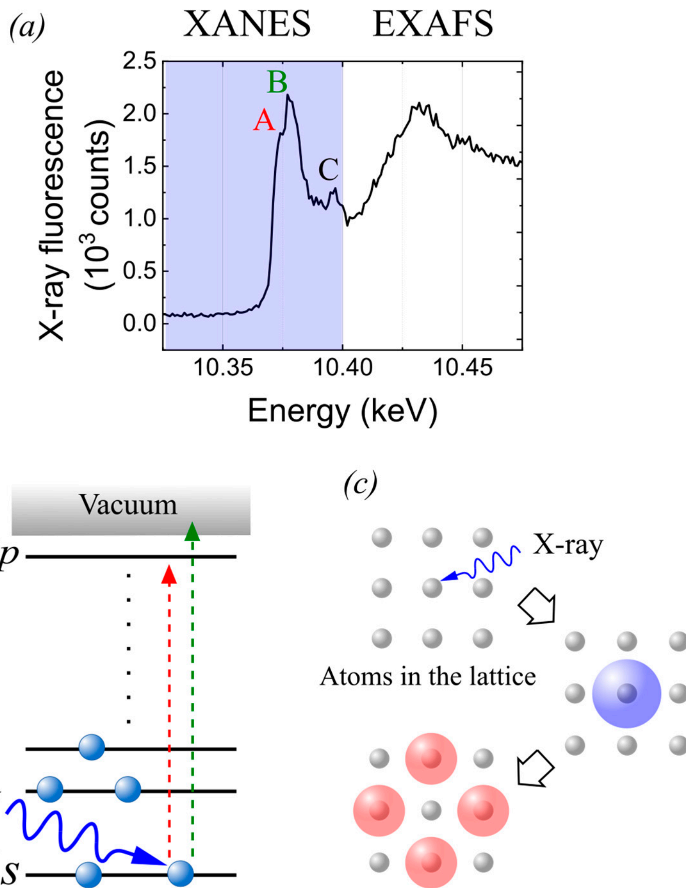

Figure 2-4 X-ray absorption spectroscopy (XAS). a) The blue area corresponds to the X-ray absorption near edge spectroscopy (XANES) which is a range of about 50 eV around the edge energy, in this case the Ga K edge in the nanowire. The extended X-ray absorption fine structure (EXAFS) region of the X-ray absorption spectrum is > 50 eV from the edge energy. Note that the energy range here is limited, so the oscillations are not clearly seen. b) Schematic showing energy levels of a Ga atom with the possible transitions that are indicated as peak A (red) and B (green) in (a). c) The backscattered waves (red spheres) from the neighboring atoms are the result of the photoelectric emission (blue sphere). Interference of these waves affects the absorption cross-section and appears as an oscillation in the EXAFS spectrum. [Panel (a) is adapted from Paper I.]

called the edge energy, which corresponds to the energy of emitted photoelectrons from a specific bound state of the atom.

Since the XRF emission is a consequence of the process above, one can use the spectrally resolved XRF detector to monitor XAS instead of the absorption cross-section (Paper I), which is typically measured by the transmitted X-ray intensity [49]. In contrast to the XRF emission spectrum in Figure 2-3, the XRF spectrum in this case is attained by monitoring a specific XRF transition, as a function of the primary X-ray energy, as showed in Figure 2-4(a). Later in this thesis, the spectrally resolved XBIC is used to investigate XAS as discussed in section 5.2.

The spectrum around the edge energy in the XAS spectrum is separated into two main regions (Figure 2-4), known as the X-ray absorption near edge spectroscopy (XANES) and the extended X-ray absorption fine structure (EXAFS). XANES concerns the pre-edge and edge region, which covers a range of about 50 eV above and below the edge energy. The energy more than 50 eV above the edge energy is the EXAFS region.

In the pre-edge region (Figure 2-4(a)), the X-ray energy is not enough to excite the electron from the atom to the continuum state, i.e. photoelectric emission. However, absorption peaks in this region can occur, corresponding to the transition to available states just below the continuum, e.g. oxidation states (Figure 2-4(b)).

Beyond the edge energy (Figure 2-4(a)), emitted photoelectrons can be considered as propagating waves from the excited atom. This wave generates backscattered waves by scattering with the neighbouring atoms in the lattice, and the backscattered waves interfere with each other (Figure 2-4(c)). Depending on the absorbed X-ray energy, the electron wave has different wavelengths and the interference can be either constructive or destructive, which predetermines the X-ray absorption probability and cross-section. This phenomenon can be observed as an oscillation in the EXAFS region. In order to analyse the EXAFS spectrum, one can Fourier transform the X-ray energy in terms of wavenumber into the real space distance to the surrounding atoms [2].

2.2.3 Photogenerated secondary electrons in semiconductors

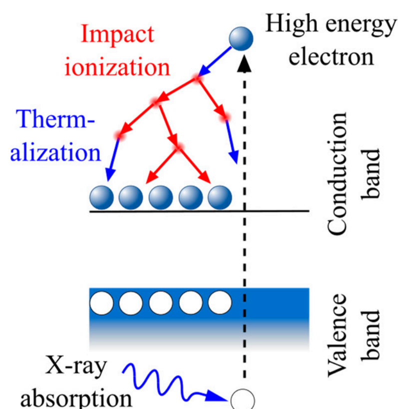

Figure 2-5 Generation of conduction band electrons in X-ray beam induced current (XBIC). The process starts with a high energy Auger electron or photoelectron, which transfers energy to valence band electrons and excite them to the conduction band. The excited electrons can in turn excite other electrons, in a cascade process of impact ionization that can lead to thousands of excited electrons. The excited electrons quickly thermalize to the band edge.

The result of the X-ray absorption through the photoelectric, Auger electron, and XRF emissions are high energy electrons and photons. The high energy photons can contribute to additional photoelectric absorption and Auger electron emissions. Simultaneously, the high energy electrons can start a cascade process of impact ionization, leading to thousands of secondary electrons, as shown in Figure 2-5.

Eventually, the excited electrons lose their excess energy to the lattice via phonons, and are thermalized to the edge of the conduction band, leading to thousands of secondary electrons [50-52].

The final yield of the electron-hole pair generation with this process is $\eta = E/\epsilon$, where E is the X-ray energy, and ϵ is the ionization energy of the semiconductor [53]. The latter can be calculated from the band gap energy E_g using $\epsilon = 2.75E_g + 0.55$ [53]. As an example, for InP with $E_g = 1.34\ eV$, a single X-ray photon with energy of $E = 10\ keV$ yields on average $\eta = 2355$ electron-hole pairs. Combining this term with the X-ray absorption probability in section 2.2, the charge generation rate in $m^{-3}s^{-1}$ as a function of the X-ray photon flux Φ can be estimated as

$$G_{n,p} = \eta p_{abs} \Phi / Ad \tag{10}$$

where A is the area of the incident X-ray beam, and d is the thickness of the material. This generation rate from the X-ray excitation is crucial to be able to compare the XBIC measurements with other excitation sources, e.g. the excitation with sun illumination of solar cells (Paper II).

2.3 Semiconductor photodetectors

Direct X-ray detectors are based on semiconductors. Charge carriers can be generated in semiconductors using the excitation of light, for instance, with photon energy higher than the bandgap energy, E_g. The energy of a photon excites an electron from the valence band to the conduction band, leaving a hole behind in the valence band. For X-rays, the excitation relates to the absorption at the atomic level with subsequent processes, as discussed in the previous section.

The excited or free charge carriers in the lattice of semiconductors can move with two transport mechanisms, *diffusion* and *drift*. Eventually, electrons in the conduction band are de-excited through *recombination* with holes in the valence band. The process is characterized by the charge carrier lifetime, τ.

Generally, diffusion is the movement of the particle from an area with high carrier concentration to a low concentration area. The diffusion is terminated when electrons and holes recombine. The characteristic distance of the diffusing charge carriers can be calculated from

$$L_{n(p),Diff} = \sqrt{D_{n(p)} \tau_{n(p)}} \tag{11}$$

where $D_{n(p)}$ is the electron (hole) diffusion coefficient and $\tau_{n(p)}$ is the lifetime of electrons (holes) [54].

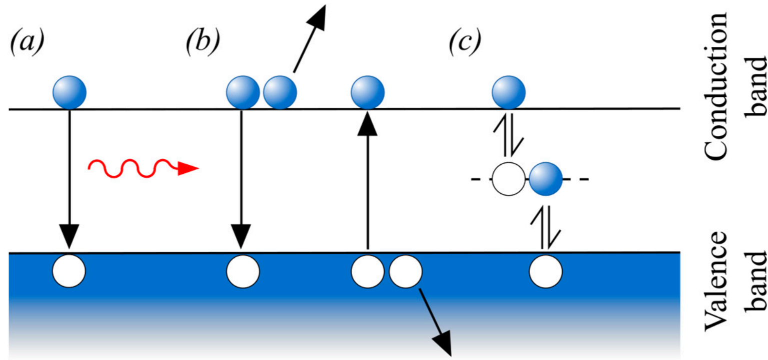

Figure 2-6 Recombination mechanisms in semiconductors: a) Radiative recombination, b) Auger recombination and c) Shockley-Read-Hall (SRH) recombination.

The charged particles, like electrons and holes, can also be mobilized by the force induced by an applied electric field, $\mathcal{E}$. This carrier transport mechanism is known as drift. The characteristic length of the drift is determined by

$$L_{n(p),Drift} = \mu_{n(p)}\tau_{n(p)}\mathcal{E} \qquad (12)$$

where $\mu_{n(p)}$ is the electron (hole) mobility. The mobility describes the carrier movement under an electric field in different materials. The diffusion coefficient can be written as a function of mobility as $D_{n(p)} = \frac{kT}{q}\mu_{n(p)}$.

As mentioned above, the charge transport ends with the recombination process, which is divided into *radiative recombination* and *non-radiative recombination*. The former case emits the excess energy in the form of photons (Figure 2-6(a)). This process is known as *photoluminescence*. In the case that the charge carriers are the result of an X-ray excitation, the process is called X-ray excited optical luminescence (XEOL), which can also be used to investigate semiconductors [55].

In contrast, the excess energy is transferred in different processes for the non-radiative recombination, which can be separated into *Auger recombination* and *Shockley-Read-Hall (SRH) recombination*. In Auger recombination, the excess energy is transferred to another charge carrier, which is then excited from the band edge (Figure 2-6(b)). In SRH recombination, the carriers recombine via energy states within the bandgap, as shown in Figure 2-6(c). These trap states are created from defects, impurities, and dangling bonds at the surface of semiconductors.

In the case of nanostructured semiconductors, the recombination is usually dominated by SRH recombination at surface states due to the high surface-to-volume ratio [56-58]. The surface states can also trap charges in long-lived states. These trapped charges can generate an electric field that could either attract or repel electrons from the surface, resulting in photodoping and photogating effects [46,59]. One method that is generally used to reduce the SRH recombination through surface states is surface passivation.

2.3.1 Photoconductors

A semiconductor can be used to detect light by just connecting it with electrodes, which is known as a photoconductor. Photogenerated electron-hole pairs from the absorbed photons drift from the applied electric field between the electrodes. This, in turn, creates an electrical current that can be measured in the circuit and alters the conductivity of the device. The semiconductor should then be low doped so that the conductivity without light is low.

The induced conductance of photoconductors is given by:

$$G = \frac{q\mu}{L^2} N \tag{13}$$

where q is the electronic charge constant ($1.6 \times 10^{-19}\ C$), L is the length of the semiconductor, and N is number of excited charge carrier. With the X-ray excitation, N could be calculated from the X-ray photon flux, as $N = \eta p_{abs} \Phi \tau$ [41]. Due to the linear current-voltage relation of photoconductors [60], the conductance is $G = I_{XBIC}/V$ where I_{XBIC} is the X-ray induced current, and V is the applied bias on the photoconductor. Therefore, eq. (13) becomes

$$I_{XBIC} = q\eta p_{abs} \Phi \frac{\mu\tau V}{L^2} \tag{14}$$

In the XBIC experiment with a nanowire as a photoconductor, the induced current I_{XBIC} is first measured under an applied bias V and then converted into the conductance G for the subsequent analysis (Paper I).

2.3.2 Photodiodes and *p-n* junctions

Another way to use semiconductor materials in a photodetector is a *p-n* junction, known as a photodiode. The mechanism of the charge collection in a photodiode is also the basis of solar cells (Paper II), commercial X-ray detectors and the nanowire devices as X-ray detectors (Paper IV).

At the *p-n* junction, the doping atoms in both regions induce a built-in electric field within the *depletion region*. This electric field creates a potential barrier denoted by ϕ_{bi}, which maintains equilibrium between the majority and minority carriers in the *p* and *n* regions. ϕ_{bi} can be calculated by [54]:

$$\phi_{bi} = \frac{kT}{q} \ln\left(\frac{N_A N_D}{n_i^2}\right) = V_t \ln\left(\frac{N_A N_D}{n_i^2}\right) \tag{15}$$

where $V_t = kT/q$ is defined as the thermal voltage, k is the Boltzmann constant (8.62×10^{-5} eV · K^{-1}), T is the temperature, n_i is the intrinsic charge

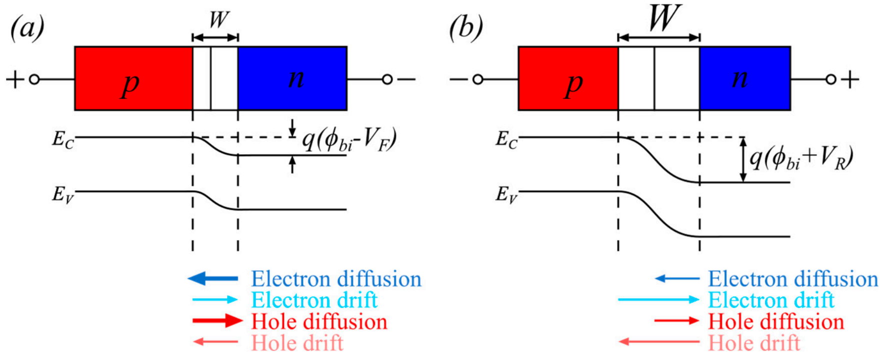

Figure 2-7 *p-n* junction under a) forward and b) reverse bias. The corresponding band structures show the change of the electric potential within the depletion region regarding the applied bias. The arrows below illustrate the direction of the charge carriers traveling across the junction with different mechanisms (diffusion and drift).

concentration and N_D (N_A) is the donor (acceptor) concentrations in n-type (p-type) semiconductors.

The electric field of the depletion region can be calculated from the fixed charge using a one-dimensional Poisson's equation,

$$\frac{d^2\phi(x)}{dx^2} = -\frac{d\mathcal{E}(x)}{dx} = -\frac{\rho(x)}{\epsilon_s} \tag{16}$$

where $\phi(x)$ is the electric potential, $\mathcal{E}(x)$ is the electric field, $\rho(x)$ is the charge density and ϵ_s is the permittivity of the semiconductor.

The *p-n* junction is no longer in equilibrium condition when a potential bias, V, is applied between the p and n regions. Thus, the total potential barrier, indicated by V_{tot}, becomes $V_{tot} = \phi_{bi} - V$. V is positive ($V > 0$) when a positive bias is applied to the p region with respect to the n region. In this case, the *p-n* junction is in the *forward bias* regime, so $V = V_F$ in Figure 2-7(a). In contrast, it is in the *reverse bias* regime when a negative bias ($V < 0$) is applied to the p region with respect to the n region, so $V = -V_R$ in Figure 2-7(b). These bias regimes change the depletion region and thereby the charge transport, as shown in Figure 2-7.

The total current through the *p-n* junction as function of the applied bias can be derived from the total current density of the carriers in each region of the junction (Figure 2-7). The detailed discussion of this calculation can be found elsewhere [54]. In general, the current-voltage relationship of the *p-n* junction can be written as:

$$I = I_s\left[\exp\left(\frac{qV}{nkT}\right) - 1\right] \tag{17}$$

where I_s is the reverse saturation current, and n is known as the *ideality factor*.

The ideality factor n is a figure of merit used to characterize the *p-n* junction, and it is expected to be in the range of $1 < n < 2$. An ideality factor of $n = 1$ implies that

diffusion dominates the current, while $n = 2$ indicates that the current is dominated by recombination in the depletion region [61]. The ideality factor was used to assess the NW device before testing with X-rays (section 3.5.3).

The process of charge generation within the photodiode is illustrated in Figure 2-8. Upon absorption within the depletion region, the photogenerated electron-hole pairs will be separated by the built-in electric field. For instance, electrons (holes) are attracted toward the positive (negative) polarity of the electric field within the *n*-type (*p*-type) material. The drift then dominates the transport mechanism within the depletion region. These electrons then become excess majority carriers on that side of the junction. For electron-hole pairs generated within either *n*- or *p*-type material, the charge carriers with the same polarity as the majority carrier become excess majority carriers. The minority carriers recombine or diffuse into the depletion region before drifting to the other side to become excess majority carriers there. However, the lifetime and diffusion lengths of the minority carriers is very low in the highly doped *p*- and *n*-segments, so the net current generated by excitation in these regions will be small.

By connecting this photodiode to the external circuit, as shown in Figure 2-8, the charge carriers can travel as a current to recombine on the other side of the device. The transport of these charges can generate power to the load in the external circuit, which is the principle of solar cells. The same principle is applied to XBIC. After the charge carrier have been excited through the process discussed in section 2.2.3, they thermalize to the band edge of the semiconductor, and are collected with the process discussed in the previous paragraph.

The ratio between the photocurrent and the incident photon flux of a photodiode represents the performance of the device in terms of the *external quantum efficiency*

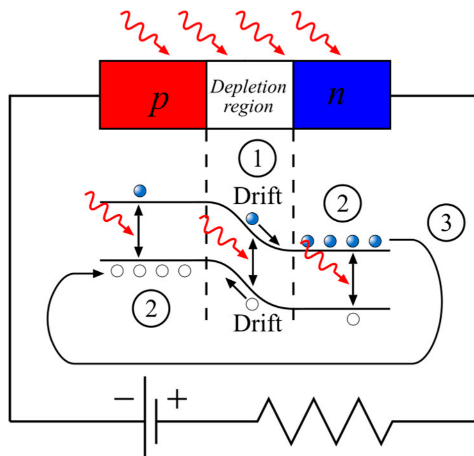

Figure 2-8 Photodiodes. The photogenerated electron-hole pairs in the depletion region (1) are separated by the electric field and the carriers drift toward the corresponding side of the *p*-*n* junction. For the electron-hole pairs generated within the doped regions (2), only the photogenerated minority carriers that randomly diffuse to the depletion region before recombination will generate a net current. With the connected circuit, the excess majority carrier can travel through the circuit (3) to recombine with the majority carrier on the other side of the junction.

(EQE). The efficiency of the photodiode to collect photogenerated charge carriers is known as the *internal quantum efficiency* (IQE). In this thesis (Paper II), the term *charge collection efficiency* (CCE), which is closely related to the IQE, is used instead to quantify how well the device collects the generated charges from the absorbed X-ray photons [62]. The CCE is spatially dependent, denoted by $S(x, y, z)$, due to the local variation of material, doping and geometry. For our X-ray detectors, EQE can be expressed as a function of CCE as

$$EQE = \frac{I_{ph}}{q\Phi} = \eta p_{abs} S(x, y, z) \tag{18}$$

where I_{ph} is the generated photocurrent. In the case of XBIC, the generated photocurrent as a function of CCE is

$$I_{ph} = q\Phi\eta p_{abs} S(x, y, z) \tag{19}$$

Note that in the case of solar cells, the reflectivity, and therefore the wavelength of the light, needs to be considered to determine the IQE of solar cells [60]. In contrast, the reflectivity of the X-ray detector in the studied energy range can be ignored. Therefore, the CCE was introduced for X-ray detectors, not to confuse it with IQE as it is used in the study of solar cells.

The charge collection in photodiodes is expected to be high within the depletion region. In order to improve the charge collection, one can increase the built-in electric field or extend the depletion region [54]. By having an intrinsic semiconductor known as i-region in between the *p-n* junction, the depletion region width can be extended. This kind of photodiode is called a *p-i-n* diode (Paper II).

2.4 Indirect and direct X-ray detectors

At this point, some background of relevant X-ray interactions and how photodetectors operate have already been introduced. How these principles are combined for X-ray detectors will be briefly discussed below.

For *indirect* or *scintillator X-ray detectors*, X-ray photons are converted to lower energy photons, i.e. UV or visible light, by a scintillator [63]. The X-ray absorption in the scintillator generates secondary electrons, which recombine via the radiative recombination process [51]. This visible light is detected using conventional detectors, e.g. photodiodes, photomultiplier tubes, or charge coupled device (CCD) cameras. The scintillation spreads photons isotropically from the initial point of the X-ray interaction, which leads to a loss of spatial resolution. An optical system can be included in the indirect X-ray detectors to optimize the spatial resolution of the detector. The spatial resolution of indirect detectors is theoretically limited to about 0.5 µm as mentioned in chapter 1.

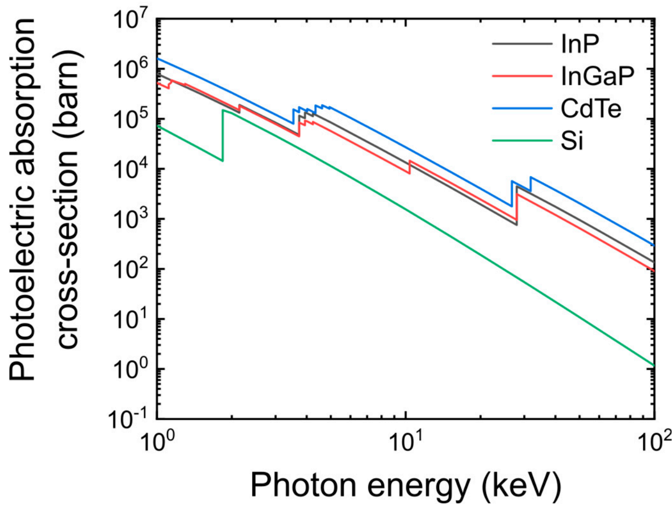

Figure 2-9 Photoelectric absorption cross section in barn of InP (black), InGaP (red), CdTe (blue) and Si (green). The data in the plot was attained from https://physics.nist.gov/PhysRefData/Xcom/html/xcom1.html.

In contrast, photogenerated electron-hole pairs, as discussed in section 2.2.3, directly contribute to the detected signal in the case of *direct X-ray detectors*. Unlike in scintillators, these charges should be collected prior to recombination. Since the signal is generated and collected within the detector, there is less noise in the process compared with the indirect detector. Furthermore, the direct detector has an advantage in terms of the linearity and the dynamic range [64]. However, as mentioned in chapter 1, the finest spatial resolution of direct X-ray detectors is a few tens of μm. The relatively complex readout electronics with hundreds of transistors per pixels means that it is difficult to make the pixels very small, and also makes direct detectors much more expensive than indirect detectors.

The direct detectors require high-quality semiconductor material with very few trap states, so that the carriers can be collected before recombining through the SRH process. Generally, materials such as Si and CdTe are used for the direct X-ray detector. The well-developed crystal growth of Si yields high quality single crystals with sufficient thickness for high efficient X-ray detectors at moderate X-ray energies [65]. Si has a much lower absorption cross-section than CdTe, but superior crystal quality, so its use is limited to modest energies up to about 20 keV (Figure 2-9). In this thesis, InP and InGaP nanowires, which can also be synthesised with high crystal quality [66], were used to develop X-ray detectors. The absorption cross-sections of InP and InGaP are almost as high as CdTe, so there should be no significant difference in terms of the quantum efficiency of these materials, as shown in Figure 2-9.

3 Nanowire device fabrication and preliminary evaluation

The methods used for device fabrication and their preliminary evaluation are described in this chapter. The first section gives a brief explanation of the NW synthesis, although this is not the focus of this thesis. The following sections describe the nanofabrication techniques that were employed to create both horizontal and vertical nanowire devices. Finally, some aspects of the electrical characterization are presented.

3.1 Nanowire synthesis

There are four different kinds of NWs studied in this thesis. These NWs were synthesized by the vapor-liquid-solid (VLS) growth mechanism with the technique known as metalorganic chemical vapor phase deposition (MOCVD), which was done by M.T. Borgström's group at *NanoLund, Lund University, Sweden*. More detail of MOCVD can be found elsewhere [67-72].

The NW synthesis starts with the deposition of the Au seed particle on the growth substrate, which is an InP (111)B wafer. The deposition is typically done with nano-imprint lithography (NIL) to create a structure for a dense array of Au particles [73-75]. Alternatively, a patterning technique using electron beam lithography (EBL) can be used, as discussed later in this chapter (section 3.3.1).

The growth substrate with Au seed particles is then placed in the reaction chamber, where the temperature is raised. Then, precursor gases, such as trimethylindium (TMIn), trimethylgallium (TMGa), and phosphine (PH_3), are fed into the chamber. The concentration of these gases depends on the required composition of the NW; for instance, TMGa was omitted for the InP NW growth. The precursor vapor is absorbed on the heated surface where it decomposes, so that atoms of the interesting elements In, Ga and P are released. The atoms collect within the liquid phase Au particle, and then incorporate in the crystal growth of the NW. Diethyl zinc (DEZn) or tetraethyl tin (TESn) are also introduced into the chamber to create the *p*- or *n*-doped segments, respectively. Figure 3-1(a) schematically shows the synthesis of the *n-i-n* doped InGaP nanowire. In addition, hydrogen chloride (HCl) is added

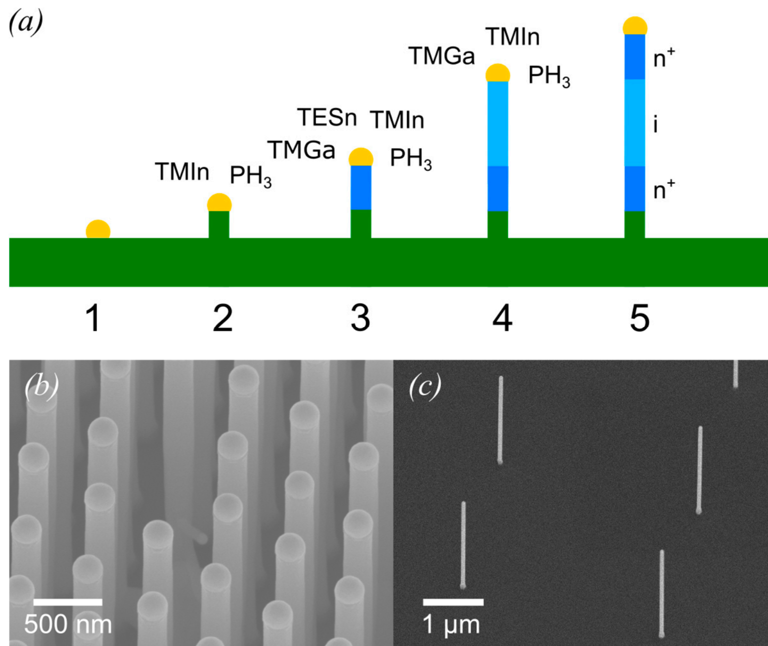

Figure 3-1 Nanowire synthesis a) Schematic showing the NW growth process, with a *n-i-n* doped InGaP NW as example. 1) Au seed particle deposition on InP substrate 2) InP stub growth in case of the InGaP NW on the InP substrate. 3) *n*-doped InGaP segment grown with TESn 4) Intrinsic segment growth of the InGaP. 5) Completed *n-i-n* doped NW. b) SEM image of a NW array at the end of the growth process. c) A larger pitch NW array, where the Au particles were prepared by the electron beam lithography (EBL) process, for the vertical nanowire devices.

during the synthesis to prevent radial growth [76,77]. The length of each segment in the NW could be monitored *in situ* by optical reflectometry [70,78].

SEM images of NW arrays from this growth process are shown in Figure 3-1(b) and (c). Figure 3-1(c) is a large pitch NW array for the vertical NW device. These NWs are *p-i-n* doped InP with a diameter of about 60 nm and a total length of about 2.2 µm. The large pitch allows the metal contact to be connected to a particular NW in the array, as discussed later in section 3.3.

3.2 Horizontal single contacted nanowire devices

Figure 3-2 shows the fabrication process for horizontal single contacted NW devices. Although most of this process was developed in Lund years ago [79], there was still a challenge in this project to create such a device on a fragile silicon nitride (Si_3N_4) membrane. The use of such an X-ray transparent substrate was necessary for XRD experiments, and special treatment of this fragile membrane during the fabrication was required.

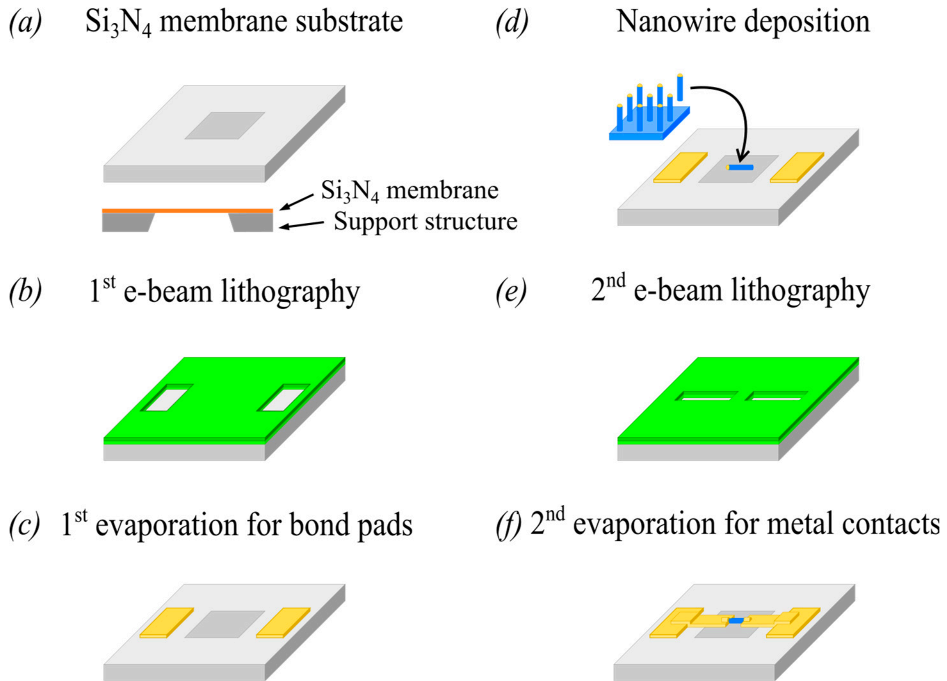

Figure 3-2 Fabrication process for horizontal single contacted nanowire devices. a) The Si_3N_4 membrane substrate and its cross-section. b) First spin coating and EBL process, to create a mask for the bond pads. c) First metal evaporation for the bond pad. d) NWs are deposited randomly on the Si_3N_4 membrane window. e) Second spin-coating and EBL for the metal contacts the ends of a single NW. f) The second evaporation for the metal contacts.

3.2.1 Predefined Si_3N_4 membrane substrate

The substrate for the horizontal single contacted NW devices was a suspended Si_3N_4 membrane, which was purchased from *Silson Ltd., Warwickshire, England*. The Si_3N_4 membrane is supported by a 3×5 mm^2 Si wafer frame, as schematically shown in Figure 3-2(a). The size of the membrane window is 250×250 μm^2, and is positioned in the center of the supporting frame. The thicknesses of the membrane and the supporting frame are 1 μm and 381 μm, respectively. This membrane is transparent for X-rays, so it is typically used as a sample holder in transmission experiments (Paper III), such as STXM, XRD, etc.

The structure of bond pads and alignment marks was created around the membrane window using *electron beam lithography* (EBL) followed by metal evaporation. Depending on the requirement of the experiment, the structure of bond pads (Figure 3-3(a)) could be changed accordingly using the EBL software to draw different patterns. For instance, two different patterns of the bond pads were used for the devices tested at beamlines using different X-ray focusing lenses (section 4.3.3).

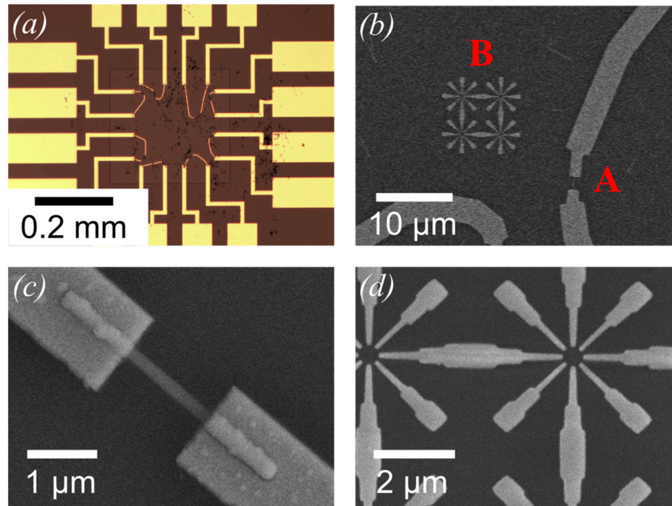

Figure 3-3 Horizontal single contacted NW devices. a) Microscope image of the Si_3N_4 window with the surrounding bond pads. b) SEM image showing a horizontal NW device (A) with Siemens stars (B) next to it on the Si_3N_4 membrane. c) High-resolution SEM image of a horizontal (in-plane) single contacted NW. d) Siemens stars that can be used for ptychographic reconstruction evaluating the beam during the experiment. The smallest features of the Siemens stars are about 100 nm.

At the beginning of the fabrication, the photoresist was spin-coated on the Si_3N_4 membrane. A fragile Si_3N_4 membrane is not suitable for the available spin-coating system at *Lund Nano Lab,* which fastens the sample with vacuum. Therefore, a dedicated process, which uses a 2" Si wafer as a carrier for the Si_3N_4 membrane, has been developed to spin-coat on this Si_3N_4 membrane [80]. This carrier wafer was first spin-coated by 950K polymethyl methacrylate (PMMA) A6 at 1000 rpm. With this photoresist as an adhesive layer, the Si_3N_4 membrane substrate could adhere to the top of the carrier wafer. Then, the carrier wafer, together with the Si_3N_4 membrane substrate, was baked at 180 °C for 5 min to harden the photoresist. At this point, the Si_3N_4 membrane substrate could stay on the rotating chuck while spin-coating. After applying the designated photoresist on the top of the Si_3N_4 membrane, it could be separated using a tweezer with a slightly push on the side of the Si_3N_4 membrane frame.

For the EBL process, a double-layer photoresist was used with 200K PMMA A5 and 950K PMMA A6 as bottom and top layers, respectively. The number in front of the photoresist name indicates the molecular weight (MW) of the photoresist, where the lower number is the more electron beam sensitive. In this double layer, the higher photosensitivity resist is used as a bottom layer. Since the bottom layer reacts more with the light or the electron beam, the exposure results in an undercut profile creating a discontinuity of the deposited material between the photoresist and the substrate. Hence, the deposited material on the substrate will not be lifted-off together with those excess materials, ensuring a successful lift-off process.

The subsequent processes used to define the bond pad structure are listed below:

1. The two layers of PMMA, as mentioned above, were spin-coated at 3500 rpm. After spin-coating each layer, the sample was baked at 180 °C for 5 min.
2. EBL was used to create the structure of the bond pads, using a 20 kV accelerating voltage and a 30 µm aperture. The dose was at 280 $\mu C/cm^2$.
3. The sample was dipped in the developer, methyl isobutyl ketone (MIBK) mixed 1:3 with isopropyl alcohol (IPA), for 75 s and IPA for 30 s.
4. A Ti/Au (10/190 nm) layer was deposited using thermal evaporation.
5. The lift-off process was done by soaking the sample in warm acetone (48 °C) for 30 min following by the rinsing with IPA for 30 s.

A final predefined Si_3N_4 substrate with a structure of bond pads and alignment marks is shown in Figure 3-3.

3.2.2 Metal contacts for a single horizontal nanowire

The NWs were then transferred from the growth substrate to the predefined Si_3N_4 membrane (Figure 3-2(d)). A small piece of cleanroom wipe paper was used to pick up some NWs from the growth substrate and transfer them to the predefined Si_3N_4 membrane.

Since the positions of the NWs are random, the alignment marks from the previous EBL and thermal evaporation processes were used as a reference position for NWs. To acquire the positions of the NWs, a LabVIEW program developed by C. Thelander at NanoLund, Lund University, was used. It creates a coordinate system from the alignment marks, giving the relative positions of the NWs on the substrate. With the known position of the NW, the resist pattern for the metal contact can be created using the process steps 1 to 3 listed in the previous section.

After the development process and right before the metal deposition, the sample was dipped into buffered oxide etch (BOE) mixed 1:10 with deionized (DI) water for 10 s, followed by rinsing in DI water for 30 s. The BOE step is used to remove any native oxide covering the exposed surface of the NW, which could affect the interface between the semiconductor NW and the metal and increase the contact resistance.

Next, thermal evaporation was used to deposit metals, which could be Ti/Au (10/230 nm) for *n*-doped NWs or Pd/Zn/Pd/Au (~10/10/10/170 nm) for *p*-doped NWs [81]. However, in the case of the *p-i-n* doped NWs, which have *p*-doping on one end and *n*-doping on the other end, the Pd/Zn/Pd/Au layer was applied on both ends to simplify the fabrication process. The performance of the NW devices seems to be unaffected by using this metal combination, as shown later in section 3.5.3.

The structure of so-called Siemens stars could also be included next to the NW devices during this fabrication process, as shown in Figure 3-3(b). A Siemens star is a structure with many angles and varying dimensions, which is generally used as the standard object to evaluate X-ray beams with ptychography [82]. The smallest structure of these Siemens stars was about 100 nm (Figure 3-3(d)). These structures helped to maintain the NW device in the focal plane during the X-ray imaging experiment, since the ptychography could be done without swapping the NW device to dedicated samples with Siemens stars.

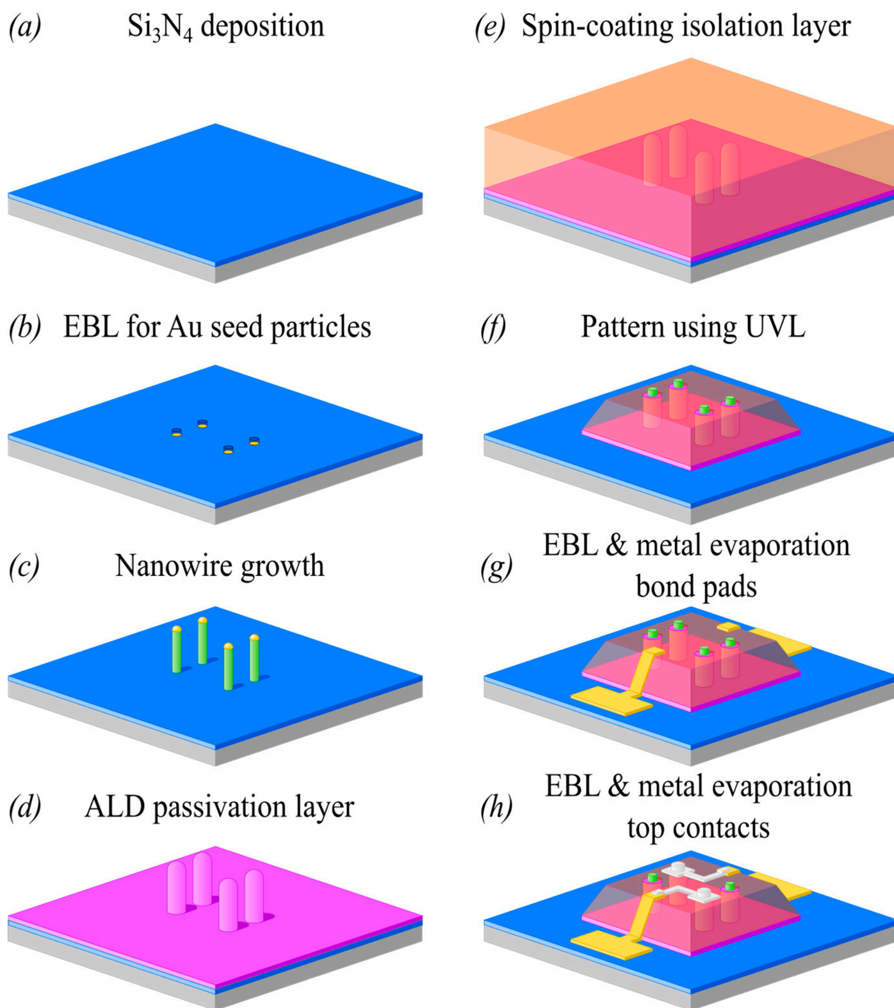

Figure 3-4 Fabrication process of vertical single nanowire devices. a) A *p*-doped InP:Zn (111) B substrate is covered by a ~70 nm Si_3N_4 layer. b) An array of Au seed particles, which was created by EBL, was deposited using metal evaporation. See next figure for details. c) The NWs were synthesized using MOCVD. d) To passivate the NWs, a layer of SiO_2 was deposited by ALD. e) The isolation layer (photoresist S1828) was spin-coated. f) Some areas of the isolation layer were removed using UVL following by RIE. The SiO_2 layer and the Au seed particles on the top of the exposed NW tip were wet etched away by BOE and Au etchant. g) EBL and metal evaporation created bond pads. h) The top contacts were created with a third round of EBL and metal evaporation.

3.3 Vertical single contacted nanowire devices

This section introduces a novel fabrication process for vertical single NW devices. With this device configuration, the requirements of the high-resolution X-ray detectors could be achieved, i.e. the minimal active area with the NW cross-section and sufficient thickness for X-ray absorption with the NW length (Chapter 1). The fabrication process flow for this NW device is displayed in Figure 3-4. Compared to the previously described fabrication process for the horizontal NW devices, this process was significantly more challenging and complicated. Also, more fabrication techniques such as *UV lithography* (UVL), *atomic layer deposition* (ALD), and *reactive ion etching* (RIE) were required.

3.3.1 Large pitch array for NW growth using EBL

The large pitch array NW was required for the vertical NW device, where a 1.5 µm metal line can reach a single NW in the array as a top contact. Therefore, a 2.5 µm × 3.5 µm pitch was designed for the NW array (Figure 3-1(c)). EBL was used to create the pattern of Au seed particles, due to its flexibility.

The Au seed particles on the substrate could move during the growth process [74]. Therefore, a ~70 nm thick Si_3N_4 layer was deposited on the InP substrate and turned into a mask, which helps to maintain the pitch size of the NW array (Figure 3-1(c)). Another purpose of this Si_3N_4 layer was to prevent a short circuit between bond pads and the substrate. By using EBL and RIE processes, holes could be created to deposit Au particles in direct contact with the substrate (Figure 3-5).

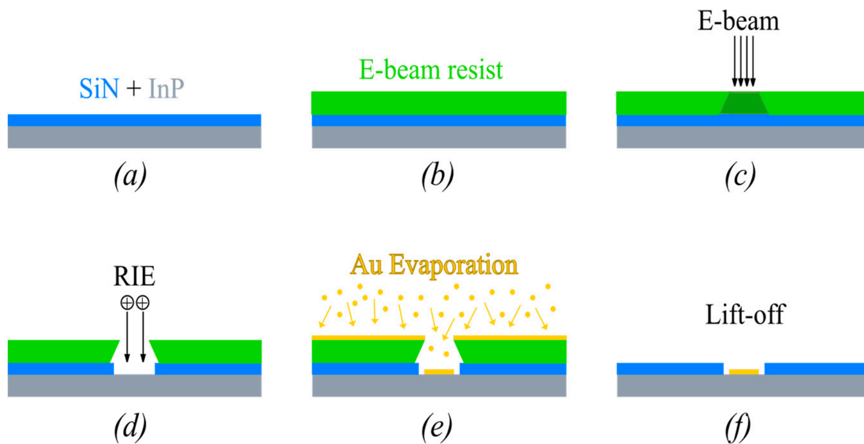

Figure 3-5 Schematic of the deposited Au in the SiN hole. a) InP substrate with SiN layer on top. b) The e-beam resist (AR-P 6200.09) is spin-coated on the SiN layer. c) EBL is used to make openings in the resist. d) RIE removes the SiN layer in the openings. e) Au was deposited with metal evaporation. f) The lift-off process removes the e-beam resist together with the excess Au material on top of the resist.

A thin single layer photoresist for the high-resolution structure was chosen instead of a conventional double-layer PMMA used previously. This sophisticated photoresist is *AR-P 6200.09*, which is also a positive e-beam resist, from *ALLRESIST GmbH, Strasburg, Germany*. This e-beam resist can achieve high-resolution structures down to 6 nm with an undercut profile.

The processes to prepare the substrate for the NW synthesis in a large pitch was:

1. Spin-coating of AR-P 6200.09, using a spin speed of 3000 rpm for 1 min, giving a thickness of about 250 nm (Figure 3-5(b)).
2. For the EBL process (Figure 3-5(c)), the parameters of the electron beam, including aperture size, accelerating voltage, and current, were set at 20 µm, 20 kV, and ~0.117 pA, respectively. The exposed AR-P 6200.09 was dissolved by dipping in the developer, Amyl acetate, for 75 s followed by DI water for 10 s.
3. The Si_3N_4 layer underneath was etched away by using RIE (Figure 3-5(d)). The gases used as etchant were CF_4 and CHF_3, with an etch rate of about 3.3 nm/s.
4. Before the Au deposition, the substrate was dipped into the 1:10 BOE for 10 s followed by DI water for another 30 s. This step was used to clean the exposed surface of the InP substrate from any residuals and oxide, for a good interface to the deposited Au.
5. Au particles were deposited into the Si_3N_4 holes using thermal evaporation (Figure 3-5(e)). The deposited Au needed to be about 20 nm thick for 50 nm diameter NWs.
6. The excess Au layer, together with the remaining resist, was removed using *remover 1165* (1-Methyl-2-Pyrrolidinone) for about 15 min. In order to wash away this remover from the substrate, it was dipped into DI water.

After this process, the NWs were grown with MOCVD as described in section 3.1.

In order to turn the NWs into a device, a metal contact was needed to connect an individual NW in the array. However, additional processes to deposit passivation and isolation layers were required before the fabrication of the metal contact on the top of the NW.

3.3.2 Nanowire passivation and isolation layer

The NWs need to be passivated to prevent a short circuit between the *p*-segment and the top contact. Ideally, this layer should also reduce the surface SRH recombination. Figure 3-6(a) shows a single NW in the array prepared with the process in the previous section. In order to passivate the NWs, a 40 nm thin layer of SiO_2 was deposited on the surface by ALD (Figure 3-6(b)). The reactions used the

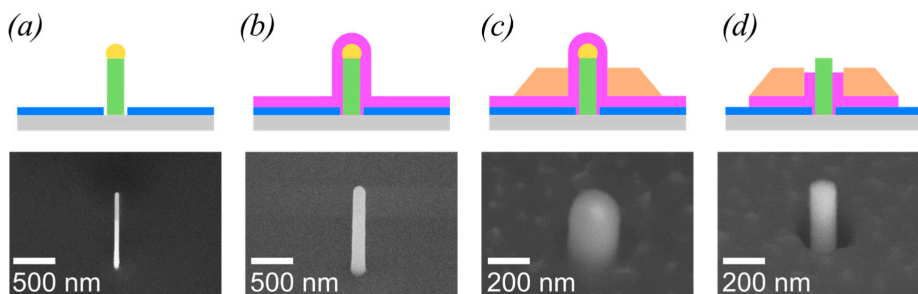

Figure 3-6 Process to fabricate passivation and isolation layers. The bottom row show corresponding SEM images of each process in the top row. a) NW grown from Au seed particle inside Si_3N_4 hole. b) NW with SiO_2 passivation layer from ALD (purple). c) The NW tip appears on the top of the isolation layer (orange) after UVL and RIE. d) Back wet etch, using BOE and Au etchant, removed part of the passivation layer and the Au seed particle at the tip of the NW. The SEM images were taken while tilting the sample at 30°. Note that the scale bar is 500 nm for the first two images and 200 nm for the last two images.

precursor tris(tert-butoxy)silanol (TTBS) together with the catalyst trimethylaluminum (TMAl). More details can be found elsewhere [83-85].

The UV photoresist called S1828 (*Microposit™*) was then spin-coated on the sample as an isolation layer, which would separate the top metal contact from the substrate. This spin-coating was done at 4000 rpm for 1 min resulting in an about 3 µm thick isolation layer, followed by baking at 120 °C for 90 s. Although the top contact was on the isolation layer, bond pads were directly deposited on the substrate. The reason for this will become clear in the next section (section 3.3.3). Therefore, parts of the isolation needed to be removed.

UVL was then used to remove parts of the isolation layer for the deposition of the bond pads, as schematically illustrated in Figure 3-6(c). The UVL process was operated with a soft-contact mode to get chamfers at the edge of the remaining photoresist, which was required in the later metal evaporation process. After exposure, the sample was developed in MF-319 (*Microposit™*) for about 5 min, followed by rinsing in DI water for 30 s. Then, the substrate was hard-baked using rapid thermal processing (RTP) for an hour at 250 °C.

Since the S1828 layer was thicker than the NW length, RIE was then used to slowly etch away parts of the isolation layer. The exposed tips of the NWs over the isolation layer could be observed by using SEM. The sequential steps of RIE and SEM were repeated until a specific tip length of NWs over the isolation layer was achieved, as shown in Figure 3-6(c).

In order to get an electrical contact on the tip of NWs, metals need to be deposited directly on the NW. Hence, the passivation layer on the exposed NW tip was removed by dipping the sample in 1:10 BOE for 30 s followed by rinsing in DI water for 1 min. The Au particle at the NW tip was also etched away in KI/I_2 for 20 s followed by rinsing in DI water for 1 min. Consequently, the bare NW tip, as

shown in Figure 3-4(f) and Figure 3-6(d), remained above the isolation layer, ready for the deposition of the top contact mentioned in the following section.

3.3.3 Bond pads and top contacts

The pattern from EBL in the previous step (section 3.3.1) also included alignment marks, which were used in the latter two EBL steps for structures of bond pads and top contacts. The double-layer photoresist of PMMA previously used for horizontal single NW devices (section 3.2.1) was employed again for these two patterns, which required lower resolution than the NW diameter.

Figure 3-7(a) shows the layout of the vertical NW device. The structure of the bond pads has two parts, which are large rectangular pads and stripes leading to the NW array. To my knowledge, the conventional bond pads of vertical NW devices, e.g. solar cells and transistors, are located on the isolation layer (floating pads). Although this is convenient for the fabrication process, floating pads are unacceptable for wire bonding, as discussed later in section 3.4. Our preliminary experiments to wire bond to floating pads on ~3 µm isolation layer of polymers, using either wedge or ball bonding (section 3.4), were not successful. The polymer of the isolation layer beneath the pads was too soft to withstand the force pushed by the wire bonding machine, and parts of the pads that were touched by the wire were stripped off. Therefore, the bond pads were instead deposited directly on the Si_3N_4

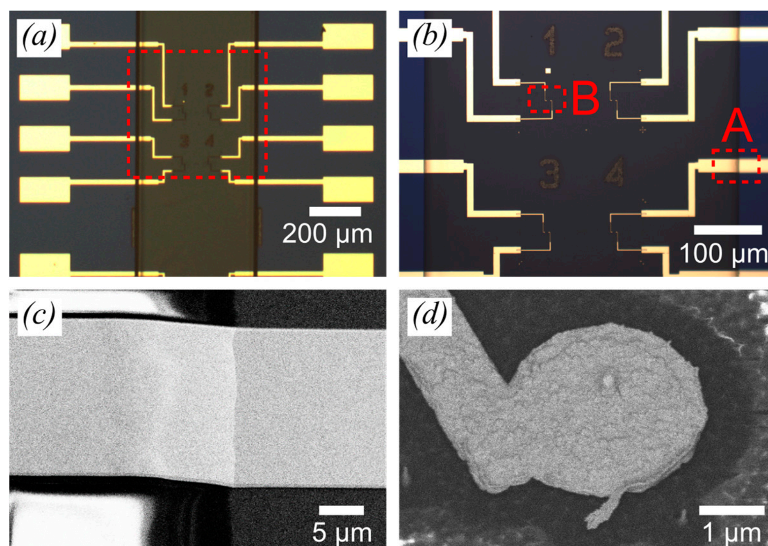

Figure 3-7 Completed vertical single NW devices. a) An image of the vertical single contacted NW devices shows bond pads as well as metal stripes leading to a single NW. b) A zoom-in image of the red square area in (a). c) SEM image of the metal stripe lies across the chamfered edge of the isolation layer, which is the area in the red square A of (b). d) The top contact made the connection to a single vertical NW. The SEM images were taken with a tilt of 30º.

layer over the substrate, which is more complicated but provided better support for the wire bonding.

Since the bond pads were resting on the substrate, it was necessary to create metal lines that lie across the substrate from each bond pad onto the top of the isolation layer (Figure 3-7(b) and (c)). In order to ensure the continuity of these lines, the edge of the isolation layer needs to have a chamfered edge, created with the soft-contact UVL process, as mentioned in the previous section. Furthermore, the substrate was tilted during the metal evaporation for better coverage of the deposited metal over the chamfered edge of the isolation layer. The bond pads of the vertical NW devices have a layer of Ti/Au with a thickness of ~20/200 nm.

The last EBL step for the top contacts was roughly aligned using the same alignment marks on the substrate created in the first EBL step for the NW arrays (section 3.3.1). Then, it used the alignment marks created together with bond pads in the second EBL step for the fine alignment. Although the second EBL step (section 3.3.2) was aligned to the first EBL step, the actual position could be off by a few µm, which is critical to align the 60 nm NW to the center of 3 µm pad, as shown in Figure 3-7(d). This problem was possibly caused by the write-field alignment process in the first two EBL steps.

Due to the fact that the moving step of the sample stage is coarser than the resolution of EBL, the fine resolution patterns can only be achieved by the deflected beam exposing within a specific area called *a write field* before the motor stage move to the new position. The typical write field has a size of 100 × 100 µm^2. Hence, the process called *write field alignment* needs to be done before the exposure to ensure the continuity of the patterns between write fields.

To reduce the error from the write field alignment in first two EBL steps, two structures created in the first and the second EBL steps were used to attain the offset

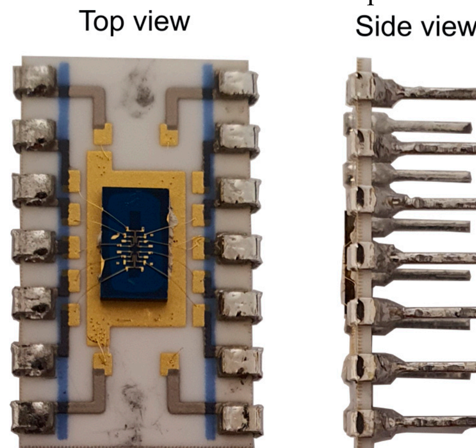

Figure 3-8 Top and side view of the dual in-line pin (DIP) chip carrier. In the top view, the mounted and wire bonded substrate can be seen. The 10 × 18 mm^2 chip carrier has 14 pins.

between each EBL step. With this offset, the top contact pattern was compensated and aligned well on top of the NW in the last EBL step. This novel alignment procedure allowed us to precisely locate the NW at the center of the top contact.

Unlike the horizontal single contact NW devices that were produced from randomly deposited NWs, the vertical NWs in the array were located at a specific position. The pattern of the top contact to a certain NW was only contained in a single write field of the EBL. Hence, the write field alignment did not affect the continuity of the pattern of the top contact. The width of the metal lines in the top contact was 1.5 µm, and the pads on the NWs were about 3 µm in diameter (Figure 3-7(d)). Similar to the previous deposition process, BOE was used to clean any residual and oxide layer prior to the metal deposition. The metal layer of Ti and Au with a thickness of 20 and 200 nm was deposited for the top contact, followed by the lift-off process.

3.4 Chip mounting and wire bonding

The final step for both kinds of devices was to mount the device chip on a 10 mm × 18 mm dual in-line pin (DIP) chip carrier (Figure 3-8). This DIP chip carrier has 14 pins. The substrate was attached to the top of the chip carrier using conductive silver glue, as shown in Figure 3-8. Then, wire bonding was used to provide an electronic connection between the NW device on the substrate to the chip carrier (Figure 3-8(b)). With this mounting and wire bonding on the chip carrier, it was easy to switch the sample in the XBIC measurement system (section 4.1).

In the case of horizontal single contacted NW devices, the chip carrier was modified by laser drilling to create a hole at the center (not shown). This hole was aligned with the Si_3N_4 membrane window, allowing X-ray transmission through the chip carrier, which is necessary for STXM and XRD experiments.

Two methods of wire bonding, *wedge bonding* and *ball bonding*, were used. The wedge wire bonding method uses a metal wedge to press the wire on the bond pad, while simultaneously applying ultrasonic energy to the wire. With the pressure and the ultrasonic energy, the wire and the pad are bonded together.

The force from the pressure and the ultrasonic energy exerted on the pad was too intense for the thin layer of Si_3N_4 beneath the bond pad in the case of vertical NW devices. Our preliminary tests showed that every vertical device had a significant leakage current after the wedge bonding. However, there was no leakage current in the horizontal NW devices, since in that case there was a much thicker (1 µm) layer of Si_3N_4 insulating the pads from the Si frame. Therefore, an alternative bonding method was needed for the vertical NW devices.

Instead of the wedge tip to push the wire on the pad, the ball bonding method uses a capillary tip with a ~25 µm diameter of Au wire. Before the bonding, the end of

the wire is melted by the heat from an applied electrical bias, forming the free air ball. Then, the capillary pushes the free air ball against the bond pad in which the pressure and the ultrasonic energy could be applied at the same time. The force can be lower in this case.

3.5 Preliminary device characterization

The fabricated devices were verified before and after mounting on the chip carrier with the methods explained in this section. These methods also provide complementary characteristics of the as-grown NWs and the NW devices. Since there are more devices on the substrate than pin connectors on the chip carrier, it is necessary to wire bond only the interesting devices for the experiment at the synchrotron facilities.

3.5.1 Electron beam induced current (EBIC) measurement

EBIC is a technique similar to XBIC, as will be discussed later in section 4.1. The available EBIC measurement system at Lund Nano Lab, Sweden, is a tungsten nanoprobe (*Kleindiek Nanotechnike*) integrated with the SEM Hitachi SU8010 [86]. In this integrated EBIC system, the probe can be moved freely with the piezo-motor stage separated from the sample holder. This system also allows EBIC and dark current-voltage (I-V) measurements through the *Point Electronic* and *Keithley 2635B* systems [86].

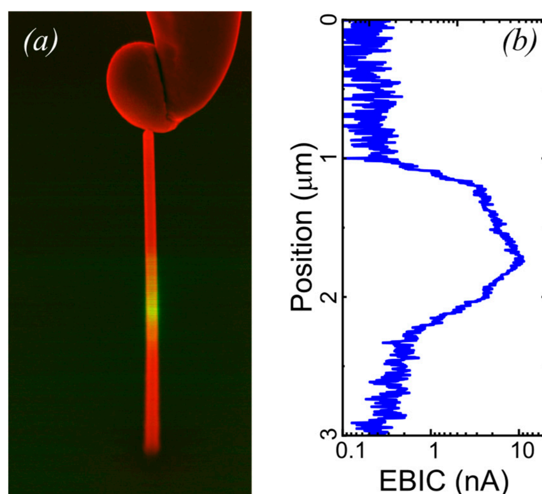

Figure 3-9 Preliminary EBIC measurement. a) EBIC map (green) from an as-grown NW for a vertical NW device, overlayed with the secondary electron signal (red). The green area indicates the depletion region of the NW at the middle of the NW. b) EBIC profile along the axial direction of the NW, starting from zero at Au particle, showing a 1 μm long active region of the nanowire.

The *p-i-n* doped NWs for the horizontal NW device were thoroughly characterized by EBIC in a separate work [75]. This technique can be used to preliminary observe the depletion region of as-grown NWs for the vertical NW devices (Paper IV). During the measurement, the probe needs to exert force by pushing against the tip of the NW, making electrical contact [87]. The current is collected at each point, as the electron beam is scanned over the sample. This measurement results in a superpositioned map of the SEM and the EBIC signals, as shown in Figure 3-9(a). Figure 3-9(b) shows the EBIC profile along the axial direction of the nanowire, indicating the ~1 µm long active region. With this setup, the I-V characteristics in dark and while exposed to the electron beam can also be measured. However, the measurement is difficult due to the instability of the probe exerted on the NW tip, since the small diameter NWs are very flexible.

Note that the available EBIC system does not have a measurement unit for the exciting electron beam current. This parameter is essential to calculate the charge generation rate in the NW with an electron beam, as eq. (10) is used in the case of XBIC. Without knowledge of the injected charge concentration, care must be taken to compare the results between XBIC and EBIC measurement. Furthermore, the XBIC measurements in this project were performed on a contacted NW device, which can be affected by the SiO_2 layer and series resistances introduced by the metal contact.

3.5.2 Electrical characterization with a probe station

The I-V characteristics of the fabricated NW devices were obtained by using *probe station Cascade 11000B* with *Keithley 4200A-SCS parameter analyser*. The probe has gold plated tungsten tips. In the case of the horizontal NW device, two probes were put on the bond pads of the NW device, as cathode and anode. Alternatively, a single probe is required to make electrical contact to a single vertical NW, while the second contact is made to the substrate.

For the photoconductive device, the conductance of the device was calculated from the slope of the I-V plot (Paper I). Graph fitting with eq. (17) yields the ideality factor of the photodiode device (Paper II and IV).

3.5.3 Simplified photocurrent measurement

The I-V characteristics of the device were measured again after wire-bonding on the chip carrier. The device is not accessible by the probe tip at this point. Hence, the equipment that was developed for the XBIC setup at the NanoMAX beamline and the P10 beamline (Paper III) was used. The equipment consists of a measurement unit, *Keysight B2985A*, and the printed circuit board (PCB) sample holder to mount

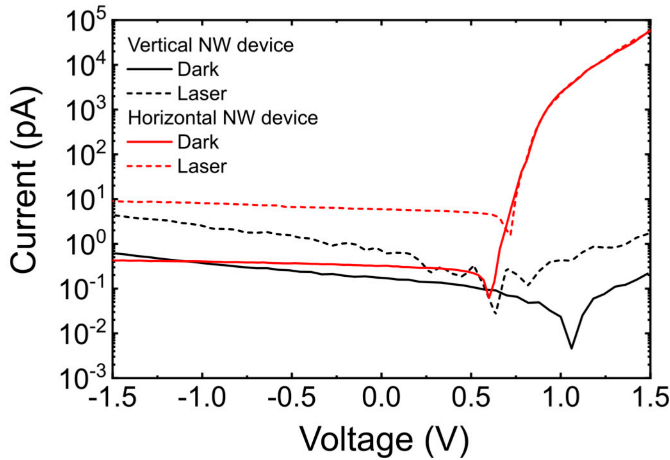

Figure 3-10 Current-voltage (I-V) characteristic of the NW devices. Horizontal *p-i-n* doped InP NW device (red lines), and vertical *p-i-n* doped InP NW device (black lines). Dashed lines are I-V characteristics under laser illumination.

the chip carrier. More details of this equipment and the integration method to the control system at the beamline are mentioned in the next chapter.

The light response of the device was preliminarily verified before testing at the beamline by comparing the dark I-V characteristic with the photocurrent measurement. To perform the simplified photocurrent measurement, the NW device was illuminated by a green laser pointer ($\lambda = 532\ nm$).

The I-V characteristics of a horizontal p-i-n doped InP NW device (Paper II) is shown in Figure 3-10, which revealed the ideality factor to be about $n = 1.4$. This ideality factor is in the range where both diffusion and recombination are comparable (section 2.3.2), indicating a high-quality device. In contrast, the dark I-V characteristic of the vertical p-i-n doped InP devices (Paper IV) exhibits an ideality factor of $n \approx 14$ (Figure 3-10), which is much higher than typical semiconductor photodiodes. Such a high ideality factor indicates additional factors that affect the current through this device, such as serial resistance or poor contacts.

Compared with the horizontal NW device, the leakage current of the vertical NW device at reverse bias is considerably higher. At forward bias, the turn-on voltage of the vertical NW devices is also higher, and the forward current is significantly lower than the horizontal NW devices. Thus, the vertical NW devices show a low-quality photodiode, which could be affected by the doping concentration from the NW synthesis [88,89], as well as the series and shunt resistances from the device processing. The I-V characteristics with light do show a photocurrent at reverse bias, as expected from photodiodes (Figure 3-10). It should be noted that the p-i-n junctions in the thicker NWs, e.g. the NWs for horizontal NW devices, have been optimized for solar cell applications for over a decade, so it’s not surprising that they show better performance.

4 X-ray characterization methods

This chapter describes the various X-ray based characterization methods that were used. The primary X-ray technique was X-ray beam induced current (XBIC). Both the principle and the use of the XBIC measurements are crucial for the investigation of the NW devices, as well as the operation of our NW X-ray detectors. Other X-ray imaging techniques were also employed, such as scanning transmission X-ray microscopy (STXM), scanning X-ray diffraction (XRD), and X-ray fluorescence, and these are also discussed in this chapter.

The XBIC results reported in this thesis were obtained from various experiments at nanofocus beamlines of three different synchrotron facilities. Even though the XBIC measurement systems were similar in all these beamlines, the availability of other techniques such as STXM, XRF, and XRD varied from beamline to beamline. Hence, the overview of our XBIC measurement system is first described, followed by the implementation at the beamlines.

4.1 X-ray beam induced current (XBIC)

XBIC was used in this thesis to understand the X-ray response of the developed nanowire devices. By using a nanofocused X-ray beam as an excitation source, the charge carriers can be generated locally within nanowire devices with the processes discussed in section 2.2.3. The photogenerated charges at the band edge will drift in the electric field from either the applied electrical bias, in photoconductors, or the built-in electric field in depletion region of a photodiode (section 2.3). During the charge collection at the band edge, the charge carriers are affected by charge transport and recombination, which could be spatially resolved by the XBIC measurement. In turn, the nanowire device can three-dimensionally map the focused X-ray beam along the optical axis using the same concept, which is how our nanowire X-ray detectors operate.

The principle of XBIC is similar to scanning photocurrent microscopy (SPCM) [90-92] and electron beam induced current (EBIC) [39,93,94] using laser and electron beams, respectively. In some literature, SPCM is referred to as laser beam induced current (LBIC). Compared with lasers, X-rays can reach a higher spatial resolution

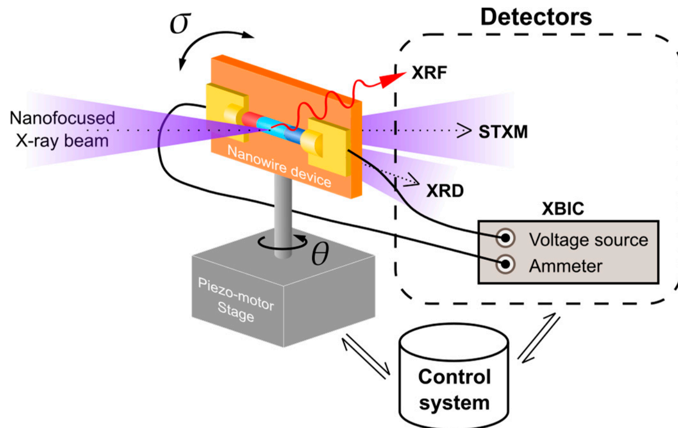

Figure 4-1 Schematic of combining X-ray microscopy with electrical measurement. The nanowire device is mounted on a sample holder and connected on one end to the external voltage source and with the other end to the amperemeter for XBIC. The sample holder is mounted on the piezo-motor stage, which can be moved in three dimensions during the measurement. The other modes of X-ray microscopy, e.g. STXM, XRF, and XRD, can be measured simultaneously with this system. [From Paper III]

with a smaller focal spot due to the lower diffraction limit. Moreover, X-ray beams have much higher penetration depth than electron beams [95], which makes them suitable for complete devices and operando investigations.

The idea of XBIC was first introduced and demonstrated by investigating grain boundaries and metal precipitations in multi-crystalline silicon solar cells, at microscale resolution, together with the XRF technique [39,40]. Later, XBIC was used together with XRF to develop silicon-based solar cells [43-45]. Recently, other potential materials for high efficiency solar cells, such as $Cu(In_{(1-x)}Ga_x)Se_2$ (CIGS) and perovskites, have also been studied using XBIC [96,97]. However, there have only been a few reports of XBIC to study semiconductor NWs [9,41,42].

The XBIC measurements of the NW devices were performed by connecting one end of the NW to the external voltage source and another end to the ampere meter, as shown in Figure 4-1. In the case of the vertical NW device, the voltage source was connected to the top contact of the NW and the ampere meter was connected to the back contact on the substrate. The tested NW device was mounted on a special sample holder, which is mentioned below. With this experimental setup, the XBIC measurement could be combined with other X-ray imaging techniques, such that STXM, scanning XRD, and XRF could be performed simultaneously (Paper III).

4.1.1 XBIC measurement system

Our XBIC measurement system was designed to test samples or devices mounted on the DIP chip carrier, as mentioned in section 3.4. An electrical circuit for the

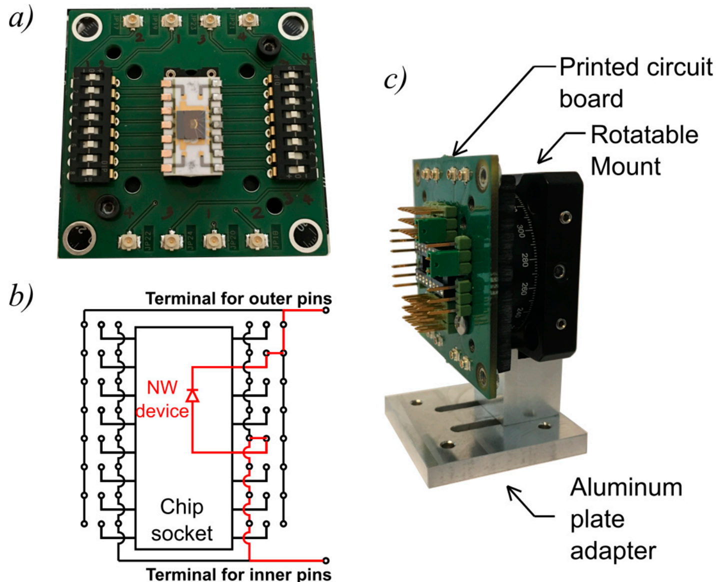

Figure 4-2 Sample holder for XBIC. a) Printed circuit board (PCB) as a sample holder for XBIC measurements, which can connect the nanowire device to the external electronic equipment. b) Circuit diagram of the PCB sample holder in a). The diode symbol represents the NW on the sample, which is connected to the different pin connectors shown as empty dots. By switching these connectors, a particular device is connected to the different connector terminals. c) All the components, consisting of a printed circuit board (PCB), a rotatable mount, and an aluminum plate adapter. Different versions of the PCB can be attached on this rotatable mount. The aluminum plate adapter, which is screwed onto the piezo motor of the sample stage, is modified to fit various beamlines. [Adapted from Paper III]

sample holder was used, allowing the sample to be changed and a particular device on the sample to be easily selected. The sample holder must be easy to access by the cables from the voltage source and the ampere meter, within the limited working area at the experimental hutch. With these requirements, the printed circuit board (PCB), as shown in Figure 4-2(a), was developed after a few iterations.

In the center of the PCB, the DIP chip carrier with the NW device is secured by the chip socket (Figure 4-2(a)). Each slot of the chip socket is connected to a tristate DIP switch (both sides on the PCB), which makes it possible to change the connection from a NW device on the chip to different connector terminals of the PCB, as schematically represented in Figure 4-2(b).

There were two different connector terminals used on the PCB sample holders. For the first version, 2-pin connectors were used. An image of the PCB with pin terminals can be found in the supporting information of Paper III. In order to provide a more reliable connection between the cable and the PCB, these were later replaced by mini-U.FL coaxial terminals, as shown in Figure 4-2(a). This allows a coaxial connection all the way from the PCB to the electronics. With the new connectors, the noise level of the XBIC measurement was also reduced significantly (Paper III).

The internal noise study of the XBIC measurement system is discussed below (section 4.1.2).

As mentioned in section 3.2, the horizontal single NW devices were randomly oriented. To make it possible to perform XBIC measurement in a one-dimensional scan along the NW axis, the sample holder is rotatable around the optical axis, to align the NW parallel to one motor direction of the stage. The rotation in this direction also allows us to perform simultaneous XRD experiments with the scattering plane manually aligned in a favorable direction, without an extra goniometer rotation axis (Paper III). For these reasons, the PCB sample holder was attached on the rotation mount *Thorlabs CRM1/M,* as shown in Figure 4-2(c). Finally, the whole sample holder can be installed on the sample stage at any beamline using an aluminum plate adapter (Figure 4-2(c)).

The electrical equipment that was connected to the sample holder varied between different beamlines. For instance, electronics were already available at the ID16B beamline, ESRF. In contrast, our Keysight system for the XBIC experiment was needed at the NanoMAX beamline, MAX IV, and the P10 beamline, PETRA III.

4.1.2 Internal electronic noise in the XBIC measurement system

To shed light on the underlying noise level of the XBIC measurement system, the background current of the NW devices has been measured (Paper III). The noise measurement was performed in various environmental and experimental conditions, including the current range of the ampere meter, the operation of the motor stage, and the ambient light, within the experimental hutch at the NanoMAX beamline. The experiment also compared the difference between pin connectors and mini coaxial connectors of the PCB sample holder.

The background current of a horizontal NW device was measured as function of time at different current ranges of the ampere meter, which were 2 pA, 20 pA, and

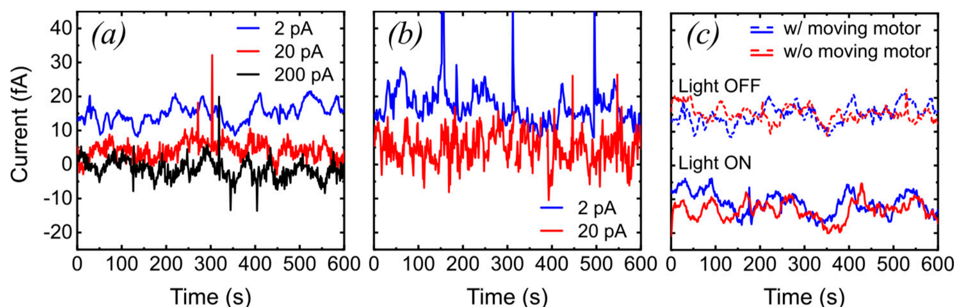

Figure 4-3 Internal electronic noise measured from the dark current of the NW device. a) Dark current measured using the sample holder with micro coaxial connector at the measurement range of 2 pA (blue), 20 pA (red), and 200 pA (black). b) The same measurement as shown in (a), but with the pin connectors. c) The dark current at different conditions: With and without operation of the piezo-motor stage, and with and without ambient light in the experimental hutch. [Adapted from Paper III]

200 pA. Figure 4-3(a) and (b) show measured results from the sample holder with 2-pin connectors and mini coaxial connectors. The dark noise level in the measurement system is less than 10 fA, and it only changed marginally. There are offsets between each range in the ampere meter. The first observation from these results is the non-repeatable spike data points that frequently appear in the measurements using the sample holder with pin connectors (Figure 4-3(b)). The results measured in Figure 4-3(c) also indicate a substantial photocurrent, around 25 fA, just from the ambient room light inside the hutch.

The noise level difference between each measured current range was only ~2%. The increased noise level while the stage motor was operating was considered statistically non-significant. However, the pin connectors showed about 35% higher noise than the mini coaxial connectors (Paper III). Note that we did not use an X-ray chopper or any electrical shielding of the PCB, which has been reported to suppress noise [95,98].

4.2 Complementary X-ray methods

A number of different X-ray methods can be used simultaneously with XBIC to investigate nanostructured devices, in a multimodal fashion, as shown in Figure 4-1. This system for combined measurements with nanofocused X-ray methods was demonstrated at the NanoMAX beamline, MAX IV (Paper III). However, it can also be used at other synchrotrons.

4.2.1 Scanning transmission X-ray microscopy (STXM)

STXM attains a contrast for an image from the transmission using X-ray beams to scan the object. Several STXM contrast modes can provide different information about the object. First, the direct transmitted beam gives the image in the *bright*

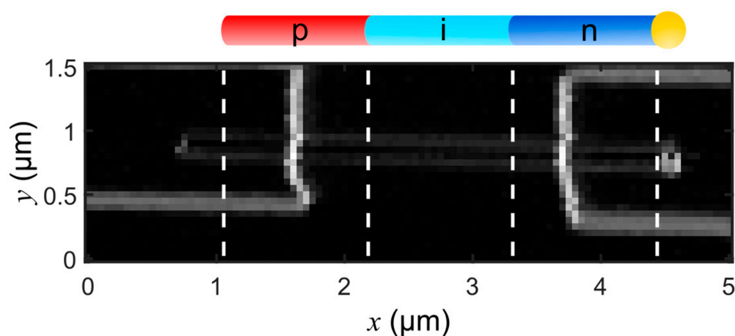

Figure 4-4 Scanning transmission X-ray microscopy (STXM). STXM image of the NW device in a differential phase contrast (DPC) mode. [Adapted from Paper III]

field. Then, parts of the beam are deflected by the thickness variation or the transversal gradient of the object. With this scattered beam, the image can be extracted in the *dark field*, which is the total intensity on the detector outside of the direct beam. Gradients in the samples also deflect the beam, and by measuring this deflection, the *differential phase contrast* (DPC) can be calculated [99].

Figure 4-4 shows a differential phase contrast (DPC) image, calculated from the magnitude of the vertical and horizontal DPC. The image shows the outlines of the NW with the metal contacts on both ends, since the DPC signal is strongest at steep gradients such as edges. The spatial resolution of the STXM is limited to the size of the focused X-ray beam. To overcome this limitation, one can use phase retrieval techniques such as ptychography [82].

4.2.2 Scanning X-ray fluorescence (XRF)

Scanning XRF is performed by collecting the XRF spectrum of the sample as it is mapped by the focused X-ray beam. At each scanned position, a spectrum of XRF signals is detected, as mentioned earlier in section 2.2.1. Each peak on the spectrum corresponds to a specific XRF emission from an electronic transition of an individual element.

The simplest method to extract material compositions from the spectrum is the integrated intensity over a particular range about the transition energy. However, the peaks in the collected spectrum are affected by the quantum efficiency of the detector, air absorption at low energy, secondary absorption and neighbouring peaks. Therefore, a more sophisticated method is to use peak fitting with software like *Pymca* [100]. With this software, scanning XRF can quantitatively determine the absolute doping concentration with high sensitivity and spatial resolution [101].

The XRF map in Figure 4-5(a) from paper III reveals material compositions within the NW devices. In this figure, the XRF signal from In atoms within the NW and Au atoms within the metal contacts are displayed in green and blue areas, respectively. More correlation between XRF and XBIC results are shown and discussed later in chapter 5.

4.2.3 Scanning X-ray diffraction (XRD)

Another X-ray imaging mode that can be extracted from the sample using this multimodal X-ray imaging is the scanning XRD, which is a technique to study the crystal structure of materials [102]. Scanning X-ray diffraction uses the focused X-ray beam to locally probe the crystal structure of the sample. At each position of the sample, the scanning beam generates scattering if the crystal is locally at the Bragg

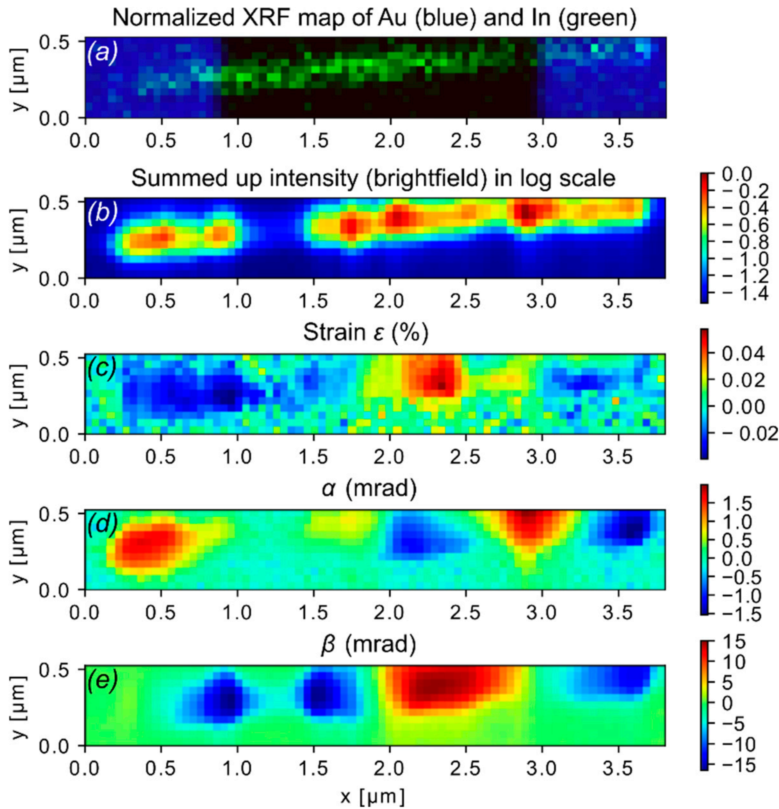

Figure 4-5 Scanning XRF and XRD results. a) Scanning XRF map of a NW device, with In (green) and Au (blue). b) Map of the total XRD intensity. c) Strain (%). d) and e) Lattice tilt around the optical axis, α, and around the vertical axis, β, respectively. [Adapted from Paper III]

angle. The scattering angle is sensitive to the variation in the lattice constant caused by, for instance, strain, piezoelectric fields, thermal expansion, surface stress, etc. This technique is widely used to investigate nanostructured semiconductor devices with nanofocused X-rays [103-108].

The XRD maps were collected for different rotation angles, θ, as schematically shown in Figure 4-1. The XRF map in Figure 4-5(a) was the reference for each θ angle, before mapping the diffraction in the reciprocal space. The total intensity of the Bragg diffraction is shown in Figure 4-5(b). The low intensity around 1.2 µm is due to the extensive bending of the NW, putting the Bragg diffraction out of the angular range.

In scanning XRD, the shifted Bragg peak relates to an associated strain and the tilt of the crystal lattice within the NW. A strain map and two tilts maps, as shown in Figure 4-5(c), (d), and (e), can then be generated from the measured XRD. The tilts are defined around the optical axis and around the vertical axis, represented by α and β, respectively. The strain and tilts in the NW are presumably due to the metal

contacts that apply stress to the NW and strongly bend it, as shown in the tilt maps [8,103]. With this information, the shape of the NW can be reconstructed using a line integral [10].

At this point, the use of the multi-modal X-ray imaging technique have been demonstrated at the NanoMAX beamline, MAX IV. However, further analysis, especially on the diffraction results, is beyond the scope of this thesis. For those who are interested in this versatile technique, a thorough analysis and discussion can be found elsewhere [109].

4.3 Synchrotron radiation sources and beamlines

This section gives a brief overview of the beamlines that were used in this thesis.

4.3.1 ID16B beamline, ESRF, Grenoble, France

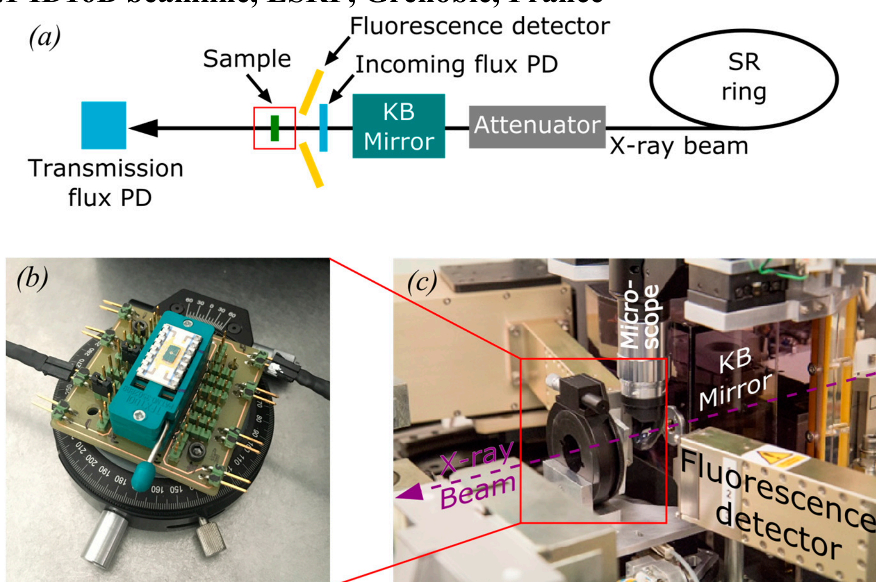

Figure 4-6 Experimental setup at the ID16B beamline. a) Schematic of the experimental setup. b) PCB sample holder on the rotatable mount with the attached cables. c) The installed sample holder in the experimental setup. Also shown are the X-ray fluorescence detector, the optical microscope and the KB mirrors.

The beamline ID16B, European synchrotron radiation facility (ESRF) [110], Grenoble, France, was specifically built as a hard X-ray nanoprobe offering a multimodal X-ray characterization at nanoscale resolution [14]. The experiments at this beamline simultaneously combined XRF and XBIC. The beam parameters for the two experiments at this beamline are listed in Table 4-1.

Table 4-1 Beam parameters of the different experiments at the ID16B beamline, ESRF

Experiment	*Sample*	*Beam mode*	*Energy (keV)*	$\Delta E/E$	*Maximum flux (s⁻¹)*
1 (Paper I)	n^+-i-n^+ InGaP NWs	Monochromatic	10.7	$\approx 10^{-4}$	$\sim 10^{11}$
2 (Paper II)	p-i-n InP and InGaP NWs	Pink beam	17.5	$\approx 10^{-2}$	$\sim 10^{12}$

An overview of ID16B is shown in Figure 4-6(a), and the actual setup is shown in Figure 4-6(b) and (c). First, the beam goes through the attenuator, which consists of metal filters. The X-ray flux at this beamline was reduced to a range of about $\sim 10^6$ s^{-1} to $\sim 10^9$ s^{-1} for the XBIC measurements (Paper I and II). Then, the beam was focused down to 50-60 nm using the KB mirrors on to the sample. The incoming and the transmitted fluxes of the X-ray beam were monitored by two photodiodes (PDs). The XRF detector and the optical microscope are located in front of the sample (Figure 4-6(a) and (c)). The sample holder with the tested sample was installed on a piezo-motor stage (Figure 4-6(c)). The electronic equipment for the XBIC measurement used in this experiment has already been discussed in Paper II.

4.3.2 NanoMAX beamline, MAX IV, Lund, Sweden

The NanoMAX beamline at MAX IV, Lund, Sweden [111] is also equipped with an X-ray nanoprobe [15,16]. The first experiment at this beamline was to demonstrate the combined X-ray imaging techniques to simultaneously investigate nanostructure samples, which in this case is the same NW solar cells studied at the ID16B beamline (Paper II). The measurement system for multimodal X-ray microscopy and the experimental setup at this beamline were discussed thoroughly in Paper III. The X-ray beam was focused to about 50 nm by the KB mirrors and the energy of the beam was 15 keV, in the experiment with the horizontal NW devices. The vertical NW device was also tested at this beamline in another experiment (Paper IV), where the X-ray energy was 10 keV and the focus size was about 90 nm.

4.3.3 P10 beamline, PETRA III – DESY, Hamburg, Germany

Instead of the KB mirrors, the experiment at this beamline used a multilayer zone-plate (MZP) to focus the X-ray beam. This kind of focusing optic that has previously been used to demonstrate a sub-5 nm focus [13], which could drastically improve the spatial resolution of the XBIC measurements. In addition, the implementation of off-axis MZPs together with the order sorting apertures (OSAs) in this experiment was expected to stop the unwanted diffraction orders, to give a low

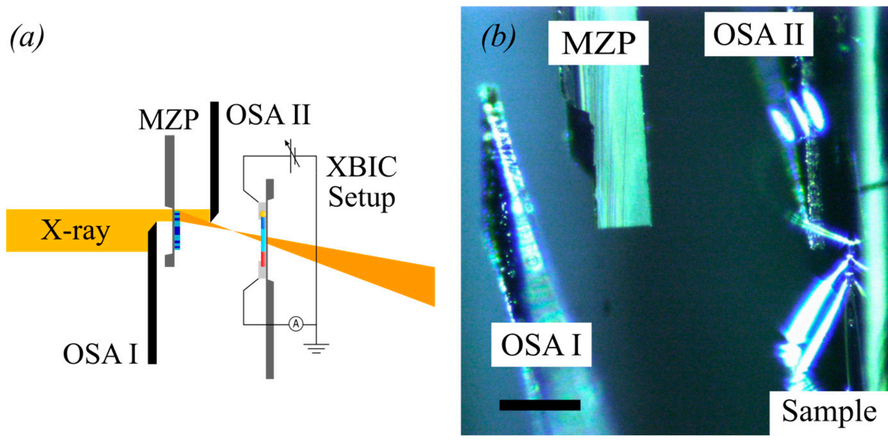

Figure 4-7 Experimental setup using MZP and OSA at the P10 beamline, PETRA III. a) Schematic of the setup. The final focal spot is achieved by the off-axis MZP configuration with OSA I and OSA II. b) Photo of the aligned optics. The distance between OSA II and the sample was about 100 μm during the measurement. The scale bar is 500 μm.

background measurement. Note that the manuscript with the results from this experiment is still in preparation.

The MZP was attached to a Si_3N_4 membrane, which was similar to the one we used for the horizontal NW device but with a smaller window, and mounted on the piezo-motor stage (Figure 4-7). The OSA is a pin-hole made into a 0.75 mm × 5.00 mm metal foil (Figure 4-7(b)), which can be used to block part of the X-rays. There were three OSAs used during the experiment. Note that all these optics were prepared by T. Salditt's group at the Institute for X-ray physics, University of Göttingen, Germany. Further information on this nanofocused X-ray beam using MZP can be found elsewhere [13,112].

The X-ray beam was first prefocused using a compound refractive lens (CRL), resulting in a microscale focal size. An aperture was used to clean up this microfocused beam, which illuminated the MZP. Then, the OSA I was put upstream from MZP to get an off-axis illumination, as shown in Figure 4-7(a). OSA II was located downstream, in between the MZP and the sample, to block the zeroth-order beam and higher-order diffraction from the MZP (Figure 4-7(a)). At this point, the focal size of the X-ray beam was already at the nanoscale resolution. By using separated piezo-motor stages, all these components were aligned to achieve the minimum focal size.

Due to the short focal length of the MZP (~1.1 mm) and the installation of the OSA II, the working distance was reduced to only a few hundred µm from the sample. Thus, the sample holder for the XBIC system was moved to about 100 µm from the OSA II during the measurement, as shown in Figure 4-7(b). All these parts had to be carefully aligned while avoiding contact.

With this complicated focusing optics, the routine ptychography used to characterize the beam propagation could not reveal the focal size during the experiment, but after. Therefore, the focal plane was located by multiple line scanning at the sharp edge of the metal contact, while the sample was moved along the beam path. This method to locate the focal plane is known as a knife-edge scanning. Then, the measurement was repeated in the smaller range with the XBIC scan over the nanowire device resulting in the 2D map of the beam waist. Finally, two-dimensional XBIC scans were performed on the plane that yielded the sharpest XBIC peak in the radial direction of the NW (section 5.4). However, the thorough analysis using ptychographic reconstructions after the beamtime suggest that the beam profiles from these optics on both sample and focal planes are more complicated. The result of this experiment is discussed in chapter 6.

4.4 Finite element method (FEM) with Comsol

To get a deeper understanding of the device properties, it is desirable to make a model of the XBIC process and compare it with the measurements. This requires solutions to the electrostatic problem, which is governed by the Poisson's equation, the charge generation and recombination, as well as the charge transport, as discussed in section 2.3 (Paper II). These kinds of problems, consisting of governing equations (differential equations) and boundary conditions, are not possible to solve analytically except for very simple geometries. However, a numerical solution of a differential equation can be calculated using the *finite element method* (FEM). Since differential equations with complicated geometries appear in many problems in physics and engineering, this is used in wide variety of fields such as mechanics, heat transfer, fluid dynamics, and electrostatics.

FEM solves the problem by dividing the system into small discrete pieces of *elements*. These elements are connected and share the degree-of-freedom by nodes where *nodal unknowns* are dependent variables of the system. In order to calculate these nodal unknowns, the differential equations are approximated by a polynomial function on each element. All the element equations are combined into a system of simultaneous equations, which are solved to satisfy the differential equations and boundary conditions of the system. The calculation of this solution is iterated with an error metric until it reaches the assigned threshold, to achieve the final solution of the system. More detail of FEM can be found elsewhere [113,114].

The FEM simulation here used the software named *COMSOL Multiphysics* (COMSOL AB, Stockholm, Sweden). With the "Semiconductor module" of this software, the designated output, e.g. photogenerated current from XBIC, could be attained from input parameters of semiconductors. The software has already been employed to investigate charge generation and transport processes in the EBIC

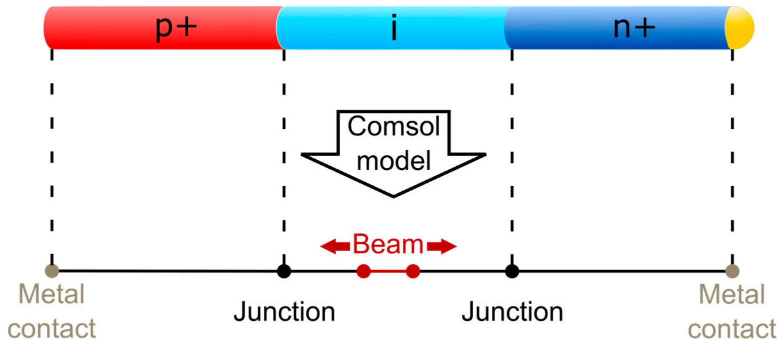

Figure 4-8 Finite element method (FEM) using COMSOL. The NW device is modeled in one dimension as a single line. The line is separated and assigned into three segments: *p*-, *i*-, and *n*-segment, each with many elements. The two red spots and the red segment in the middle of the *i*-segment corresponds to the exposed area, which can be moved along the NW to simulate the 1D XBIC scan along the NW axis.

technique performed on a similar NW device [37], as well as heating from a nanofocused X-ray beam [115]. Hence, a similar method was applied here to shed light on the underlying mechanisms of the XBIC results from NW solar cells.

In order to simplify the FEM of the NW device, a one-dimensional model was used. This is justified since the beam is smaller than the NW cross-section and the NW has radial symmetry. A line representing the NW device was separated by spots into three segments (*p*-, *i*-, and *n*-segment) as shown in Figure 4-8. Each segment was 1.1 µm long, the same as the actual NW. Material parameters, including doping concentration, charge mobility, and carrier lifetime, can be found in the supporting information of Paper II.

The local photoexcitation, corresponding to the probe beam, was introduced between two points, as shown at the center of the *i*-segment in Figure 4-8. The spots were 60 nm away from each other, which is about the same size as the focusing beam at the ID16B beamline. A constant charge generation rate was assigned to this beam, disregarding the complicated absorption process discussed in section 2.2.3. The charge generation rate was calculated using eq. (10) in section 2.2.3. The NW ends were assigned as metal contacts, where a bias could be applied. Finally, in order to simulate the scanning beam, the points limiting the beam were moved from one end to the other. At each position, the photocurrent in the NW was numerically calculated. The photocurrent results plotted against the beam position were then compared with the measurement results, as discussed later in section 5.5. The bias dependent XBIC could also be simulated by changing the applied voltage on the points of the metal contacts.

5 X-ray characterization results

The results from the various types of XBIC measurements, e.g. spectrally resolved, X-ray flux variation, and bias dependence, are presented and discussed in this chapter. The correlation of XBIC with the XRF measurements and FEM simulations is also shown here.

5.1 Simultaneous XBIC and XRF imaging

Simultaneous XBIC and XRF images were acquired to provide the finer detail of the tested NW devices. With this information, the region of interest, such as the active region of the NW device, could be explored.

5.1.1 Horizontal single contacted nanowire devices

Figure 5-1 shows the results from n^{+}-i-n^{+} doped InGaP NW devices. The I-V characteristics of these devices, measured at the beamline under both dark and X-ray conditions, are shown in Figure 5-1(a). The plot is not perfectly linear as being expected for the photoconductors, especially at the low voltage. Due to the doping of the NW, the band offset between the highly doped n-segment and the intrinsic segment could affect the charge collection, as schematically displayed in the inset of Figure 5-1(a). The slope of the I-V characteristic plot under the dark condition yields the conductance at $G = 2.24 \times 10^{-14}\ \Omega^{-1}$. The conductance increased to $G = 6.55 \times 10^{-12}\ \Omega^{-1}$ with X-ray excitation in the center of the NW. Although the I-V curve of the device is not fully linear, the detected photocurrent from the XBIC measurement was converted to the conductance G for the subsequence analysis, as discussed in section 2.3.1.

Figure 5-1(b) shows the superpositioned maps of the XBIC and the XRF signals from a two-dimensional scan over the device, measured with an applied bias of 0.05 V. The different XRF spectra, attained at point A and B in Figure 5-1(b), can be found in the supporting information of Paper I. The XBIC signal is the green area in Figure 5-1(b). The XBIC and XRF profiles along the axial direction of the NW device are plotted in Figure 5-1(c). The dashed lines in these figures (Figure 5-1(b) and (c)) indicate the nominal junctions in the composition and doping profile of the

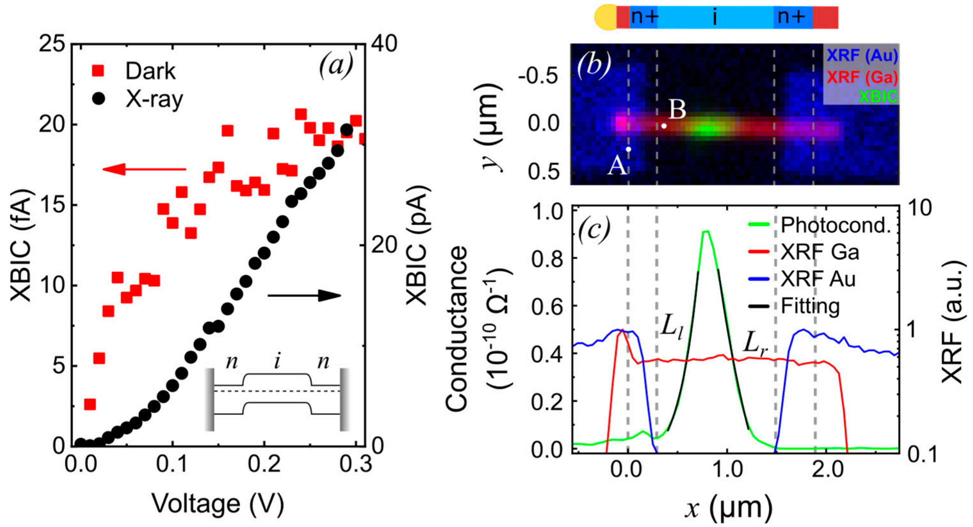

Figure 5-1 X-ray response of n^+-*i*-n^+ NW devices. a) Current-voltage (I-V) characteristics of the device measured in dark (red) and under X-ray illumination (black). The inset is a schematic of the NW's band structure, showing the band offset between the intrinsic segment and the adjacent *n*-segments. The band offset becomes a barrier, obstructing the charge transport. b) XBIC map of the n^+-*i*-n^+ NW device, where the red purple segments at both ends are the GaP cap at the top and the InP stub at the bottom. The green area in this map corresponds to the XBIC signal, whereas the red and the blue areas are the XRF signal from Ga and Au atoms, respectively. c) XBIC and XRF profiles along the axial direction of the NW, as shown in (b). [Adapted from Paper I]

NW. The XBIC signal was strongest near the center of the NW, although slightly shifted to the left (Figure 5-1(b) and (c)).

Figure 5-2 (a) displays the superpositioned maps of the XBIC and XRF signals from a *p*-*i*-*n* doped InP NW device. A similar result from *p*-*i*-*n* doped InGaP NW devices can be found in Paper II. The green area in this map is the XBIC signal, whereas the blue and red areas are the XRF signal from In and Au atoms, respectively. Then, a line scan yielded the XBIC and XRF profiles along the NW axis, as shown in Figure 5-2(b). With the nominal doping profile in Figure 5-2(b), the XBIC signal appears to be mostly generated from the intrinsic segment of the NW, where the photogenerated charges are affected by the built-in electric field (section 2.3.2).

The plot of the XBIC profile in both Figure 5-1(c) and Figure 5-2(b) shows that the XBIC signal decays on both sides. An exponential fit can quantify these decays with a characteristic decay length, $L_{l(r)}$, for the left (right) decay [116,117]. The characteristic decay lengths from these profiles are more than a few hundred nm (Paper I and II), which is larger than the size of the X-ray beam. It will be shown later, in section 5.6, that the characteristic decay lengths can be affected by the measurement conditions.

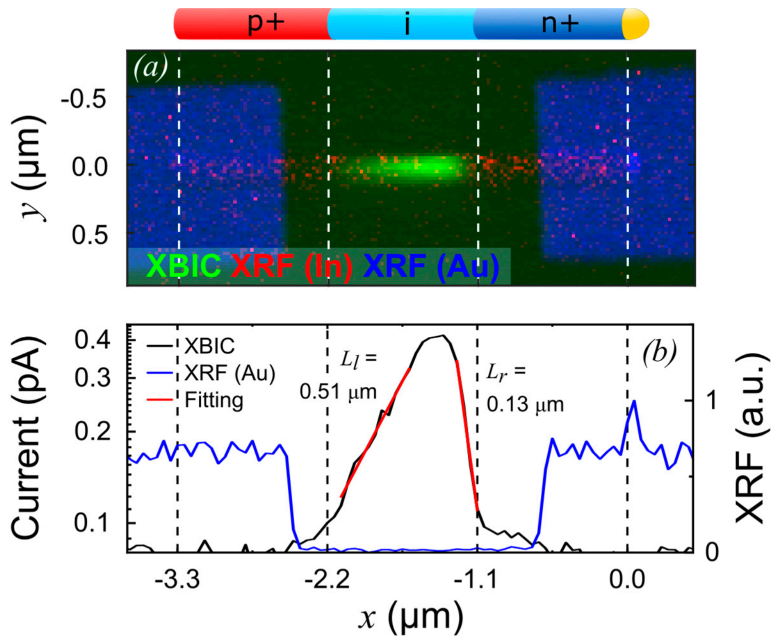

Figure 5-2 XBIC map of *p-i-n* doped NW devices. a) Superpositioned XBIC and XRF maps, where green is the XBIC signal, red is the XRF signal from In atoms, and blue is the XRF signal from Au atoms. b) XBIC (black line) and XRF (blue line) profile from a line scan along the NW axis. Fitted lines (black) give the characteristic decay lengths of the XBIC peak. The vertical gray lines in these maps and plots indicate the nominal doping junctions of this NW. [Adapted from Paper II]

5.1.2 Vertical *p-i-n* doped InP nanowire devices

Despite the poor photodiode characteristics of the vertical NW devices, they still generate a photocurrent under light conditions, as shown in section 3.5. Figure 5-3(a) shows the XBIC map of a nanowire device, measured at zero bias and $\Phi = 3.99 \times 10^{8}\ s^{-1}$. The scan was done with 100 nm step size and 0.1 s acquisition

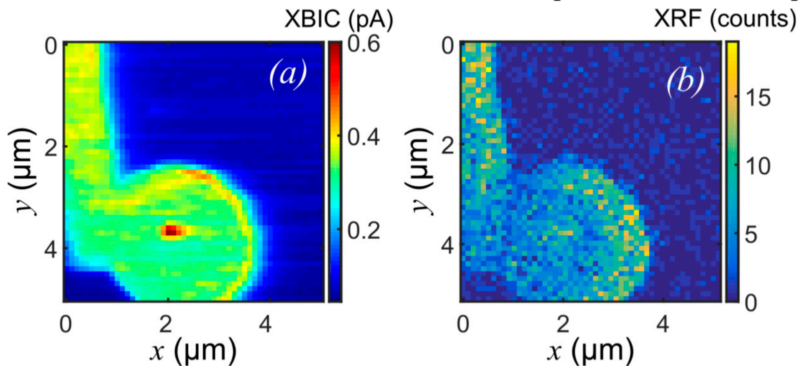

Figure 5-3 XBIC and XRF maps of a vertical NW device. a) XBIC map attained directly from the nanowire device. A strong photocurrent can be detected from the nanowire at the center of the top contact. b) XRF map attained simultaneously with the photocurrent map, as shown in (a). [Adapted from Paper IV]

time. The simultaneous XRF map of Ti is shown in Figure 5-3(b). A strong XBIC signal can be observed from the nanowire at $(x, y) = (2\ \mu m, 3.5\ \mu m)$. There was also a significant background signal from the top contact, due to photoelectrons. This background signal was subtracted in the subsequent analysis of the vertical NW devices (Paper IV).

5.2 Spectrally resolved XBIC and XRF

Although the XBIC signal itself is due to the excited charges collected at the band structure level, the signal originates at the atomic level with the X-ray absorption process (section 2.2.3). The X-ray absorption cross-section varies strongly at specific X-ray energies corresponding to atomic levels, as discussed in section 2.2.2. This variation is thus expected to be observed on the XBIC signal. To investigate this, spectrally resolved measurements were employed (Paper I).

In this experiment, the X-ray beam was located at the center of the XBIC peak on the n^+-i-n^+ doped InGaP NW device (Figure 5-1(c)). The energy of the beam was then varied about the Ga K-edge energy (~10.37 keV) in a range of 250 eV. Then, the XBIC and XRF (Ga K) signals were simultaneously monitored as XAS spectra, as shown in Figure 5-4.

In Figure 5-4(a), the same oscillation can be observed in the post-edge region in both the XBIC and XRF spectra, due to interference between the emitted photoelectron and the neighboring atoms (section 2.2.2). This confirms that photogenerated charges in the XBIC signal originate at the atomic level, just like the XRF signal. The only difference between the two spectra in Figure 5-4(a) is at the pre-edge region, where the XBIC signal in terms of the conductance is not at the minimum level. The reason is that the XBIC charge carriers can also be generated

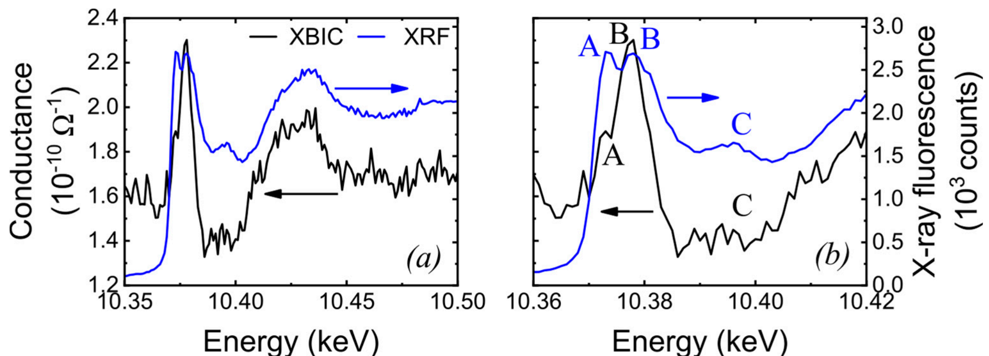

Figure 5-4 XAS spectra. a) XBIC (black) and Ga K XRF (blue) signals. b) A zoom-in plot of (a) about the edge energy to highlight the interesting peaks, A, B, and C. [Adapted from Paper I]

by X-ray absorption in In and P atoms. In contrast, the Ga K XRF signal, in this case, was only possible from the excitation of the Ga K-edge.

Further analysis of these spectra was done qualitatively in this thesis. A quantitative analysis of XAS in terms of XBIC and XRF is beyond the scope of this study. Figure 5-4(b) shows more detail of the spectra at the Ga K-edge energy in which three significant peaks are labelled as peak A, B, and C in both spectra. Peak A (10.374 keV) and B (10.378 keV) correspond to the transition from the 1s state to the 4p state and the continuum, respectively (Figure 2-4(b)) [118,119]. For peak C, which is about 17 eV from the edge energy, this energy from the Ga K-edge energy could be converted into a distance between atoms that corresponds to the zinc blende structure [120].

5.3 X-ray photon flux variation

As discussed in section 2.3, XBIC is a function of the X-ray photon flux. By applying a metal attenuator, the X-ray photon flux at the beamline can be controlled. Various electrical responses were observed between different kinds of NW devices from the variation of X-ray photon flux.

5.3.1 Photogating and photodoping in n^+-i-n^+ doped nanowire device

In this experiment, the X-ray photon flux was increased from $\Phi = 8.0\times10^7$ s^{-1} to $\Phi = 1.6\times10^8$ s^{-1} before the X-ray beam damaged the device. With the doubled X-ray photon flux, the maximum XBIC signal was increased about three times (from 1.32 pA to 4.56 pA), as shown in Figure 5-5(a). This superlinear relationship is in contrast to the linear property of eq. (13). Figure 5-5(b) shows a long saturation time of the device after the X-ray beam was turned on.

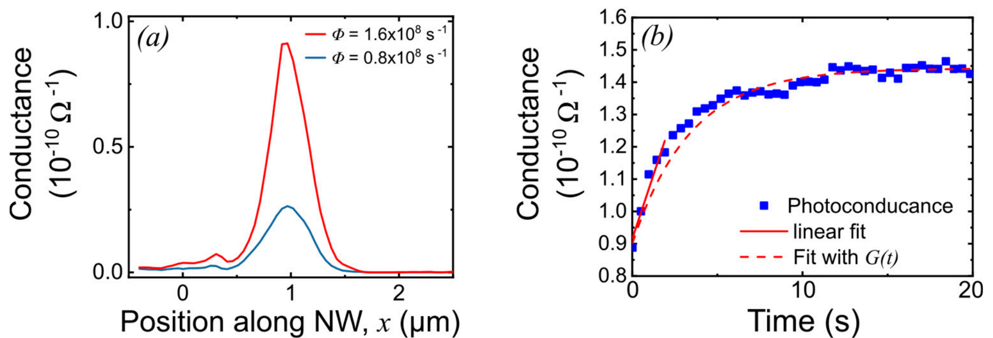

Figure 5-5 Flux variation XBIC measurements. a) XBIC profiles along the axial direction of the NW at two different X-ray photon fluxes. b) The time response of the n^+-i-n^+ NW device. The XBIC signal from the device was measured starting from time t = 0, when the X-ray beam was turned on. [Adapted from Paper I]

This result could be explained by photogating and photodoping effects, which have been observed in similar experiments on NW devices using X-ray [41] and UV excitation [46]. The photogating and photodoping effects are related to trapped charge carriers at the surface states of the NW. The trapped charges form an electrostatic gate of the NW that can change the Fermi level and increase the conductance, a phenomenon called photogating. Additionally, if for instance holes are trapped in long-lived traps, this leaves extra conduction band electrons that can contribute to the conductivity. This latter process is called photodoping.

With the trapped charges, the expression of the photoconductance at time *t* after the X-ray beam is turned on, as discussed in section 2.3.1, is modified as:

$$\sigma_{XBIC}(t) = q\eta p_{abs} p_{trap} \left(\frac{\mu\tau_{tr}}{l^2}\right)\left(1 - \exp\left(-\frac{t}{\tau_{tr}}\right)\right)\Phi \tag{20}$$

where p_{trap} is the trapping probability and τ_{tr} is the detrapping lifetime [41]. For this NW device, the parameters for the XBIC calculation (section 2.3.1) are $\eta = 1867$ and $p_{abs} = 9.7 \times 10^{-3}$. The time, *t,* is measured from when the X-ray shutter opens. When t is small, the rate of the photoconductance or the slope of this plot is constant, which is expressed as $d\sigma_{XBIC}/dt = q\eta p_{abs} p_{trap}(\mu/l^2)\Phi$. Hence, a linear fit of this slope yields $p_{trap} = 1.45 \times 10^{-10}$. Then, the plot in Figure 5-5(b) is fitted by eq. (20), yielding a detrapping lifetime of $\tau_{tr} = 3.41$ s.

Finally, we can calculate the gain of the device, g, by dividing the conductance from the collected charge (eq. (20)) with the term $q\eta p_{abs}\Phi$, which is the absorbed charge [41]. With $t \to \infty$, the gain becomes $g = p_{trap}(\mu\tau_{tr}/l^2)$ resulting in $g = 0.34$ for this device. The low gain is because of the low trapping probability.

5.3.2 Escaping secondary electrons in horizontal *p-i-n* doped nanowire devices

Multiple XBIC line scans at different photon fluxes were measured in the *p-i-n* doped NW device, as shown in Figure 5-6(a). Then, the maximum XBIC values were plotted as a function of the X-ray photon flux in the log-log scale, as shown in Figure 5-6(b). A linear relation can be observed, which is consistent with the theoretical calculation discussed in section 2.3.2.

In contrast to the previous case of the n^+-i-n^+ doped NW devices, the linear function implies that the *p-i-n* doped NW devices are not affected by photogating and photodoping effects. This is further supported by time-dependent measurements shown below. However, the calculation using eq. (19) gave a higher XBIC result comparing to the measurements (Figure 5-6(b)). The measured XBIC result is about 5% of the calculated XBIC, which could be explained by the high probability for secondary electron and photon to escape from nanostructure devices [62].

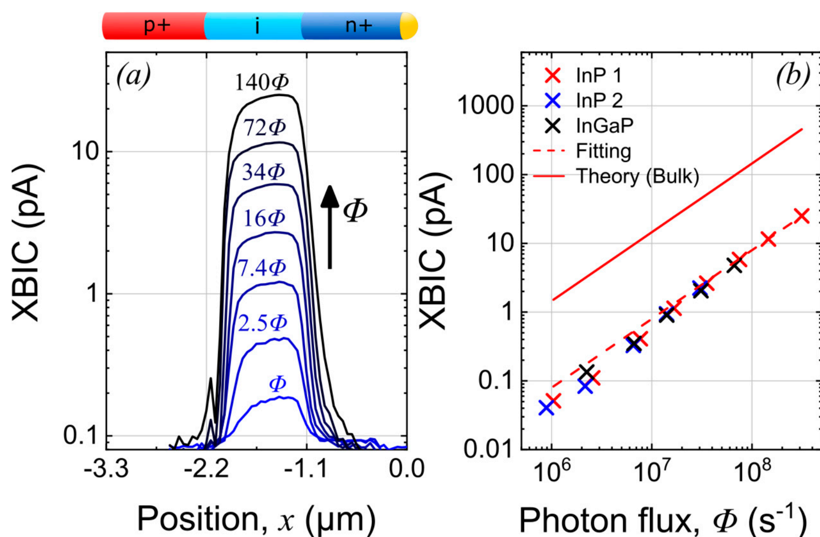

Figure 5-6 X-ray photon flux variation XBIC of *p-i-n* doped InP and InGaP NW devices. a) Multiple XBIC line scans along the NW axis at varying X-ray photon flux, where $\Phi = 2.6\times10^6$ s^{-1}. b) XBIC peak values from the line scans vs. the X-ray photon flux, where the red solid line is from the calculation, and the red dashed line is from the fitting. [Adapted from Paper II]

With this range of the X-ray photon flux, the generation rate of the charge carrier, $G_{n,p}$, is calculated to be about $10^{27} - 10^{30}\ m^{-3}s^{-1}$ using eq. (10). The generation rate is roughly equivalent to the excitation resulting from one sun illumination, which is the relevant excitation level for solar cells [121], indicating that XBIC can be used in the study of NW solar cells.

Figure 5-7 shows the time-dependent XBIC measurements, comparing the n^+-i-n^+ and the *p-i-n* doped InP NW devices. In contrast to the gradual increase in signal over 10 s in the n^+-i-n^+ doped device, the *p-i-n* doped device has a much faster rise time (Figure 5-7), faster than our setup can measure. The fast response time of the

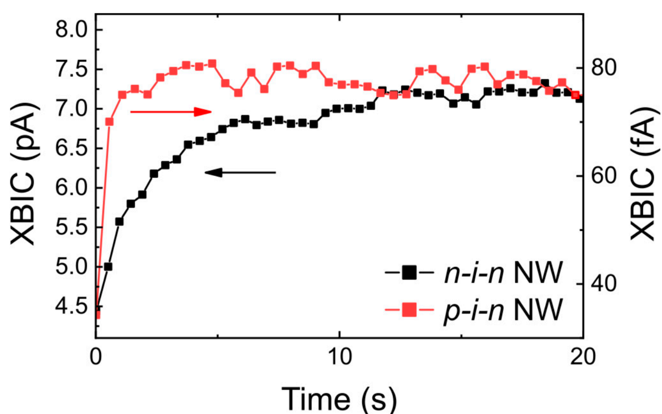

Figure 5-7 Time-dependent signal after switching the X-ray beam on. Comparison between the response time of n^+-i-n^+ NW device (black) and *p-i-n* NW device (red). The beam was switched on a $t = 0$ s. Note that the time resolution was much too poor to capture the fast increase for the *p-i-n* NW device.

p-i-n doped device shows that this device is not dominated by surface traps, as discussed in section 2.3.

5.3.3 Sub-linear XBIC behaviour with X-ray photon flux variation

Similar measurements were made for the vertical device, and the maximum XBIC signal at each X-ray photon flux was plotted as red dots in Figure 5-8. The full set of XBIC maps for this measurement can be found in the supporting information of Paper IV. With the active region of about 1 μm as an absorption length, the parameters for eq. (19) is calculated to be $\eta = 2.35 \times 10^{3}$ and $p_{abs} = 2.48 \times 10^{-2}$. Consequently, the calculated XBIC is more than two orders of magnitude higher than the measured XBIC, which again is probably due to the escape of secondary photons and electrons [62]. Furthermore, the carrier collection probability $S(x, y, z)$ could be lower than 100% along the 1 μm active region (Figure 3-9), as the EBIC measurements suggest.

The XBIC signal exhibits a sublinear behavior as function of the X-ray photon flux. This sublinear behavior can be empirically fitted very well with the power-law equation, $I_{XBIC} = a\Phi^{b}$ (solid red line in Figure 5-8), where $a = 3.24 \times 10^{-18}$, and $b = 0.6$. Thus, the XBIC signal can be expressed as

$$I_{XBIC} = (3.24 \times 10^{-18})\Phi^{0.6} \tag{21}$$

The reason for the sublinear flux dependence is not clear. The high X-ray photon flux increases the amount of generated carriers, which possibly leads to increased Auger recombination [122-124]. Thus, more charge carriers could recombine before they were collected as an XBIC signal at high X-ray photon flux. Another possibility is that the device is affected by surface traps and photogating, as discussed above. A dedicated investigation is required to understand this sub-linear behaviour.

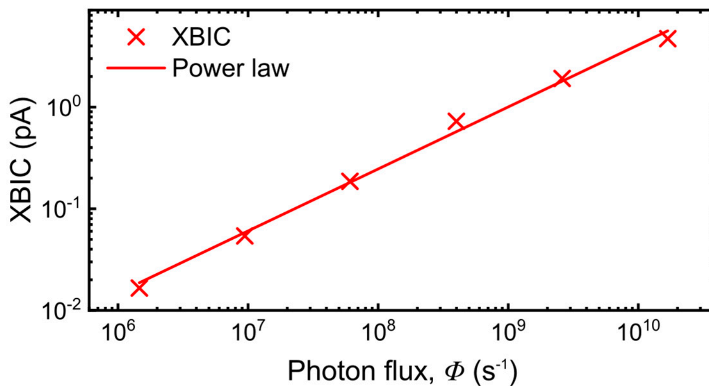

Figure 5-8 X-ray photon flux variation XBIC of a vertical NW device. The measured XBIC (red crosses) from the vertical NW device, fitted with a power-law function, $I_{XBIC} = a\Phi^{b}$ with $a = 3.24 \times 10^{-18}$, and $b = 0.6$ (red line). [Adapted from Paper IV]

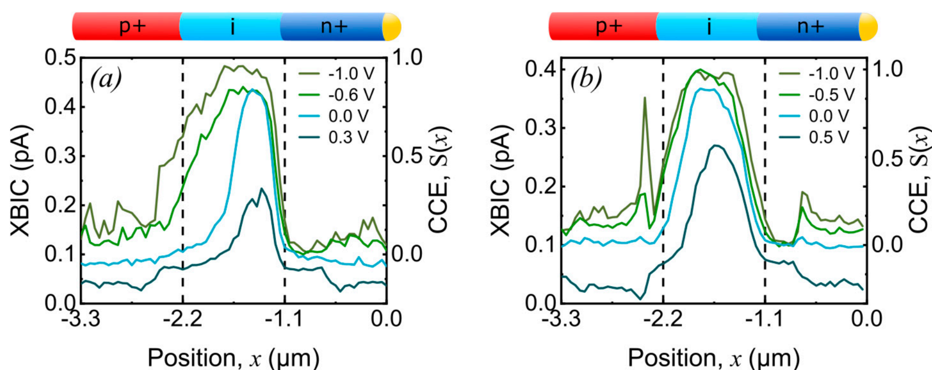

Figure 5-9 Bias dependent XBIC profiles along the axial direction. a) The *p-i-n* doped InP NW device. b) The *p-i-n* doped InGaP NW device. [Adapted from Paper II]

5.4 Bias dependent XBIC and spatial charge collection efficiency (CCE)

The bias dependent XBIC was performed on the *p-i-n* doped NW devices to understand the correlation between the applied bias and the charge collection of the NW devices. The previous X-ray photon flux variation XBIC shows that the horizontal *p-i-n* doped NW devices have a benefit over the horizontal *n-i-n* doped NW devices in terms of the charge collection with the built-in electric field of the depletion region. The electric field is also affected by the applied bias on the device (section 2.3.2). With this bias dependent XBIC, a further insight of charge collection process of this *p-i-n* doped NW devices could be explored.

The XBIC profiles, which were acquired from line scans along the axial of the *p-i-n* doped NW device at different applied biases at $\Phi = 6.5 \times 10^{6}\ s^{-1}$, are shown in Figure 5-9. A similar result can be observed in *p-i-n* doped InP and InGaP NW devices (Paper II). The XBIC peak width increases and the maximum XBIC is saturated at reversed bias. At forward bias, which is relevant to the operation of the solar cells, the XBIC peak is reduced and shifted toward the *n*-segment. Furthermore, the whole XBIC profile is shifted downward due to the increase of the dark current at forward bias.

The saturated photocurrent at reverse bias indicates the maximum of the charge collection even with the increase electric field. At this point, the spatially relative CCE of the device is assumed to be at $S(x) = 100\%$, i.e. practically all generated charges are collected. The current background level at zero bias (V = 0 V) is then defined as the minimum point for $S(x)$. With these two points, the measured XBIC profiles could be converted into CCE (Figure 5-9). Hence, the most efficient charge collection of these NW devices is toward the *n-i* junction, as discussed in Ref. [33,121].

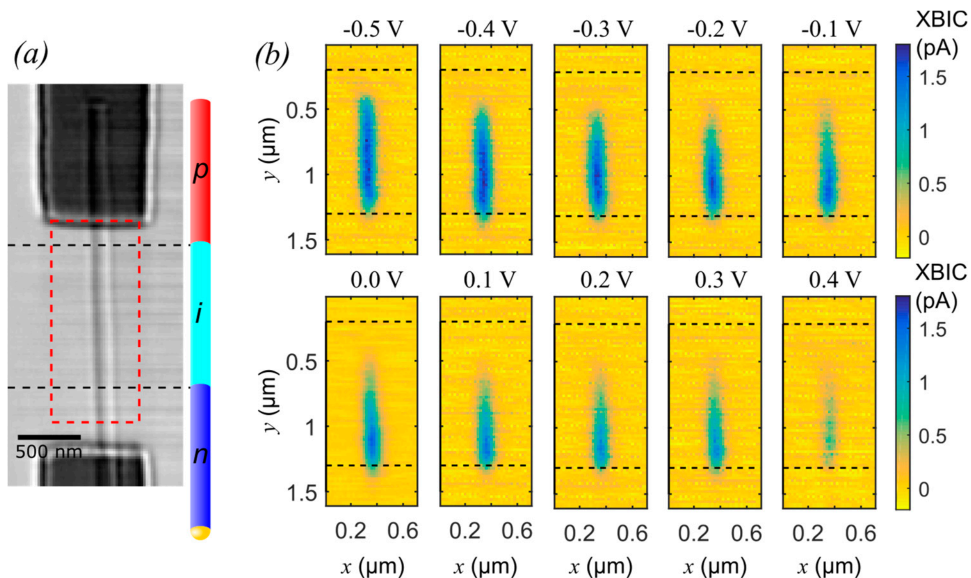

Figure 5-10 Two-dimensional XBIC maps with applied bias variation. a) Holographic image of the NW device, with a schematic showing the nominal doping profile. b) XBIC maps with the applied bias varying from -0.5 V to 0.4 V with an increment of 0.1 V. Dashed lines on these maps indicate the nominal doping profile of the NW.

Figure 5-10 shows high-resolution XBIC maps collected from the bias dependent measurement on similar NW devices at the P10 beamline, PETRA-III ($\Phi = 4.1 \times 10^6\ s^{-1}$). These results will be included in a manuscript that is now in preparation. The step size of the scan was 20 nm and the acquisition time was 0.1 s. Despite the complexity of the beam profile used in the scan, which will be shown in section 6.1, the underlying charge collection process revealed by XBIC is still similar to the results from the ID16B beamline, ESRF, as mentioned above. This two-dimensional map illustrated a completed spatially relative CCE in both axial and radial direction of the NW solar cells.

5.5 Finite element method modelling of XBIC

Here, the finite element method (FEM) was employed to explain the shift of the XBIC peak toward the n-segment at forward bias in Figure 5-9 and Figure 5-10. Figure 5-11 displays the result of this simulation. The first simulation investigated the actual doping in the middle segment. Three NW models with p-doping, intrinsic, and n-doping in the middle segment were investigated, and the corresponding band structures are illustrated in Figure 5-11(a). The doping type within the middle segment significantly affects the band structures of the NW, and leads to the different distributions of the electric field within this segment (Paper II).

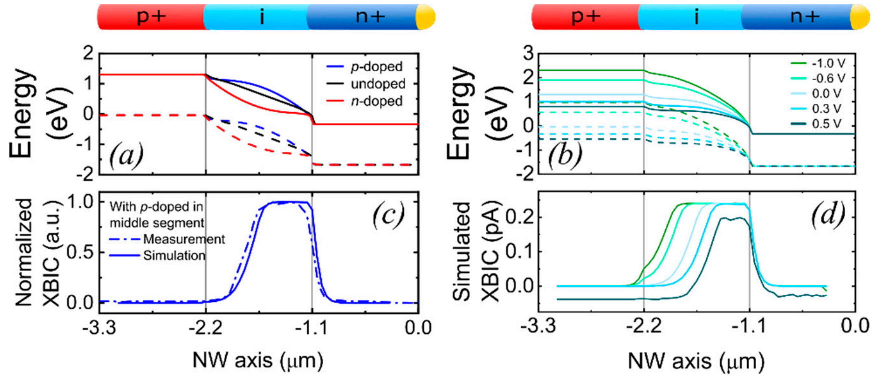

Figure 5-11 Finite element modeling of XBIC. a) The band structures calculated from the NW models with three different doping types in the middle segment: *p*-doped, intrinsic (undoped), and *n*-doped. b) The band structures calculated from the NW model with a *p*-doped middle segment at different applied biases. c) Comparison between simulated and measured XBIC. d) Simulated XBIC profile at different applied biases corresponding to the electric field distribution of the band structure in (b). [Adapted from Paper II]

The XBIC signal without an applied bias (V = 0 V) was calculated from these models using FEM. The simulation result of the *p*-doped middle segment model is shown in comparison with the measurement result in Figure 5-11(c). The results of the other cases can be found in Paper II. According to the simulations, the InP NWs have a *p*-doped middle segment. This is consistent with a separately reported result using the nano-XRF technique where the *p*-doped (Zn) concentration in similar (but not identical) NWs was found to be $5 \times 10^{17}\ cm^{-3}$ in the middle segment [101]. This unintentional doping during the growth of the middle segment could be attributed to the process known as *memory effect*, where Zn remaining in the growth chamber from the previous *p*-segment incorporates in the subsequent middle segment growth [69].

By using this doping NW model with the applied bias, the calculation yields the bias dependent band structures, as shown in Figure 5-11(b). From these band structures, the distribution of electric field within the middle segment, determined by the slope of the band structure (section 2.3.2), extends toward the *p*-segment at reverse bias. In contrast, the electric field is reduced and pushed toward the *n*-segment at forward bias. The same trend also appears in the simulated XBIC profile at different applied bias in Figure 5-11(d). This simulation result can very well describe the shift of the measured XBIC under applied bias discussed in the previous section (Figure 5-9(a)).

5.6 Axial XBIC distribution and carrier transport

In this section, the correlation between X-ray photon flux and applied bias on the characteristic decay length of the axial XBIC profiles were investigated (Paper II). The characteristic decay lengths extracted from the axial XBIC profiles are shown

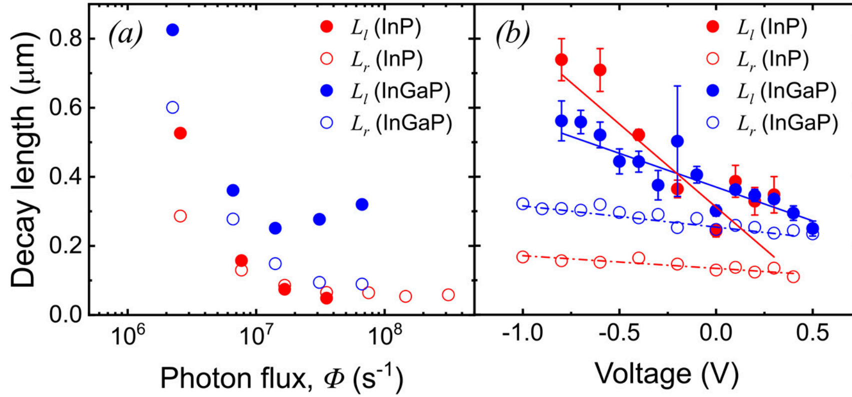

Figure 5-12 Characteristic decay lengths from the axially XBIC profile. a) The characteristic decay length as a function of X-ray photon flux. b) The characteristic decay length as a function of applied biases. The red (blue) filled circles, red (blue) circles are the decay length from the fit of the left and right slopes of XBIC profile in InP (InGaP) NW devices. [Adapted from Paper II]

in Figure 5-12(a) for the X-ray photon flux variation and Figure 5-12(b) for the applied bias dependence.

The decay length as a function of X-ray photon flux converges from hundreds of nm at low flux to the size of the beam at high flux. This result could be explained by higher charge density from the increasing photon flux, which raises the recombination rate and the chance of the carrier scattering. Consequently, the enhanced recombination shortens the transport length of the charge carrier.

In contrast, the result shows a different effect on the decay length from the applied bias (Figure 5-12(b)). The decay on the right slope is almost constant, which is consistent with previous reports [116,117]. However, reducing the applied bias significantly increases the decay length of the left slope. From the FEM results, the right slope corresponds to the diffusion length in the *n*-segment (Figure 5-11(c)), which is independent of the applied bias. In turn, the left slope, which is located inside the middle segment, is mostly dominated by the drift transport due to the changing of the electric field distribution, as shown in Figure 5-11(b).

6 Imaging of nanofocused X-rays using nanowire devices

Both single horizontal and vertical NW devices were employed as X-ray detectors to map nanofocused X-ray beams. First, a single horizontal NW device was used to map the beam waist of nanofocused X-rays from the off-axis MZPs at the P10 beamline, PETRA III. Then, we present the results from our vertical nanowire devices to three-dimensionally map the nanofocused X-ray beam at the NanoMAX beamline (Paper IV).

6.1 MZP focus measured with a horizontal nanowire

The propagation of the nanofocused X-ray beam from the off-axis MZP at the P10 beamline, PETRA III, was ptychographically reconstructed, as shown in Figure 6-1(a) and (b) for the vertical (y-axis) and horizontal (x-axis) direction, respectively. This ptychographic reconstruction used Siemens stars next to the NW devices, mentioned in section 3.2, as test objects. The ptychographic reconstruction itself, which was done after the experiment, is out of the scope of this thesis [82]. At the focal plane, defined as the origin in the z-direction (z = 0 µm), the focus shows an asymmetry where it is 13.3 nm in the vertical and 29.5 nm in the horizontal direction.

Figure 6-1(c) is the XBIC map with the scanning method mentioned in section 4.3.3, showing the beam waist of the nanofocused X-rays. The beam was only scanned horizontally, in x, since the NW axis was oriented along y (Figure 5-10(a)). Note that the center position of the XBIC peak at each z-plane gradually moved in the x-direction due to the off-axis MZP. Hence, the XBIC peaks were re-centered to make it possible to compare with the ptychography in Figure 6-1(b). This plot indicates that the sharpest symmetric XBIC peak is located upstream at position z = -50 µm, called the sample plane, where the bias dependent XBIC maps in section 5.4 were measured.

The comparison between the XBIC profile and the beam profile in the x-direction is shown in Figure 6-1(e) and (f) for the sample plane and the focus plane, respectively. Despite the complicated beam profile on the sample plane, the XBIC

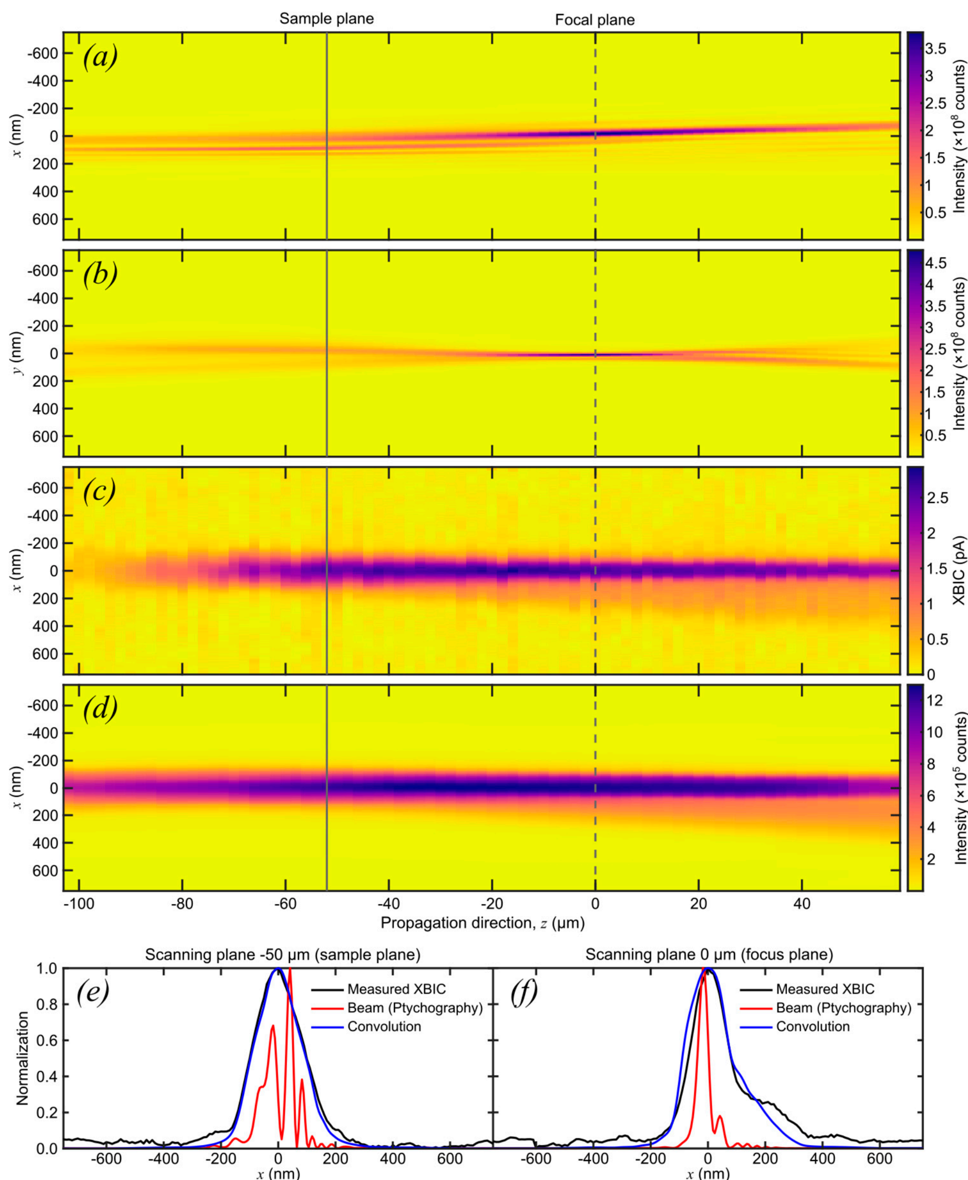

Figure 6-1 Nanofocused X-rays from the off-axis MZP at the P10 beamline, PETRA III. a) and b) Ptychographic reconstruction of the propagated beam viewed along *y* (vertical) and *x* (horizontal), respectively. This reconstruction shows that the focus from the off-axis MZP is different in the vertical and horizontal directions. The focal plane is defined as z = 0 μm (dashed line) with a focus of 13.3 nm × 29.5 nm (vertical × horizontal). c) The beam measured by XBIC, where the sharpest symmetric XBIC peak is at z = -50 μm (solid line) defined as the sample plane. d) The convolution of the beam in (b) and the NW. e) and f) The profiles of the propagating beam from XBIC measurement, ptychography, and convolution on the sample plane and the focal plane, respectively.

profile is sharp and symmetric. In contrast, the asymmetric focus created the broad shoulder on one side of the XBIC profile at the focus plane (Figure 6-1(f)).

To compare, the beam profile from ptychography was convolved with the thickness profile along the radial axis of the NW (not show here), shown as blue lines in Figure 6-1(e) and (f). Figure 6-1(d) is the same convolution along the propagating beam. Generally, the convolution results agree quite well with the XBIC profiles and map, indicating that the NW diameter limits the spatial resolution as expected. However, the FWHM of this XBIC peak is about 110 nm, which is considerably narrower than the NW diameter (180 nm). It is unclear why the radial XBIC profile is narrower than the NW radius, but one possible explanation is that the loss of secondary photons and electrons is stronger at the surface of the nanowire. A study answering this question should be done with an even smaller nanofocused beam. The results with the nanofocused beam from MZP will be included in a manuscript that is now in preparation.

6.2 3D imaging of the NanoMAX focus

The final experiment investigated the KB focus at the NanoMax beamline. The beam had an FWHM at the focus of 88 nm × 86 nm (vertical × horizontal), as revealed by ptychography [16], shown in Figure 6-2(a) and (b). The vertical NW

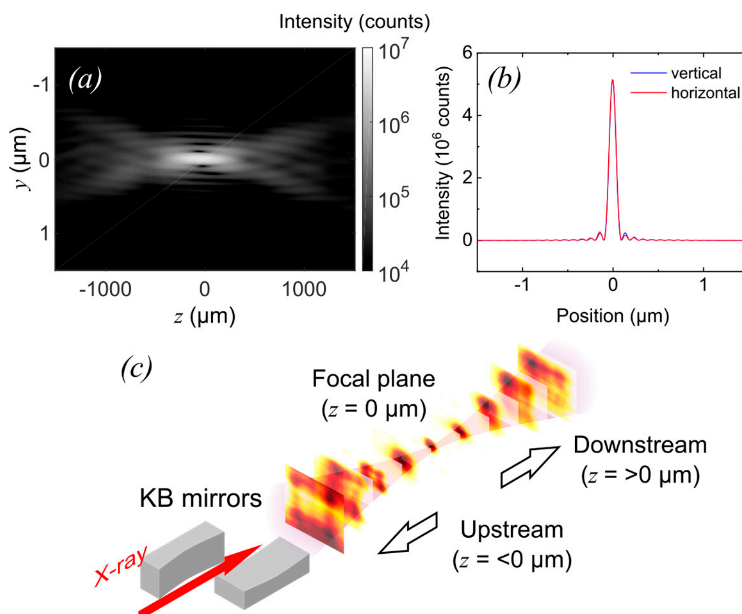

Figure 6-2 Characterization of nanofocused beam with a vertical nanowire device. a) Propagated beam, reconstructed by ptychography. b) Beam profile in vertical and horizontal directions at the focal plane. c) X-ray nanofocus imaging at multiple planes along the beam. [Panel (c) is adapted from Paper IV.]

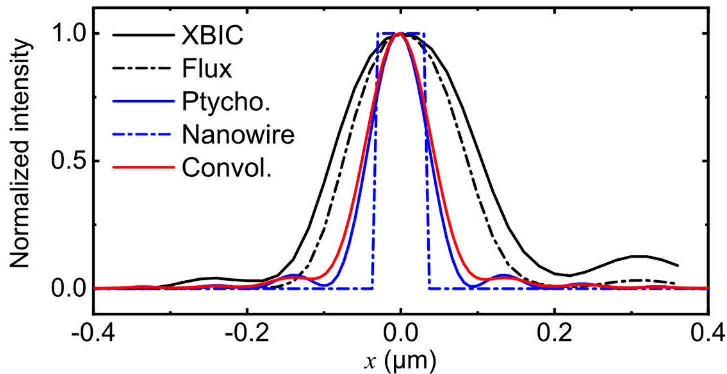

Figure 6-3 Analysis of peak width Convolution (red line) of the beam from ptychography (blue line) and the NW cross-section (dash-doted blue line). The convolution is compared with the XBIC profile from the measurement (black line) and the calculated X-ray photon fluxed using eq. (31). [Adapted from Paper IV]

device was two-dimensionally scanned at various planes along the nanofocused X-ray beam, while the XBIC was measured from the device (Paper IV). These maps were scanned at the maximum X-ray photon flux since the intensity of the beam is strongly reduced away from the focal plane. The scanned planes are schematically represented along the beam from the KB mirrors in Figure 6-2(c). The position z = 0 μm is the focal plane, and the negative (positive) z is the upstream (downstream) direction.

At the focal plane, the average size of the focal beam observed in these XBIC maps is about 190 nm in the horizontal and vertical directions. By converting the XBIC signal map to X-ray flux using eq. (21), the average FWHM of the beam reduces to about 150 nm, which is still larger than the focal size calculated from the ptychography mentioned earlier. To make a better comparison with the measurements, the beam profile from ptychography was convolved with a box function representing the NW cross-section. The convolution has an FWHM of about 95 nm, which is still significantly smaller than the measured flux profile (Figure 6-3). The size of the focal beam on the XBIC map was expected to be limited by the NW diameter like the previous case. However, the instability of the measurement system as observed in the XBIC maps, and the background signal in the top contact could affect the results.

The NW device is unable to reveal any features of the very small beam at the focus, but away from the focus the beam is larger. Figure 6-4(a) shows the comparison of the intensity distribution along the focusing beam from ptychography in the left column and the XBIC map on the right column. The XBIC maps agree well with the ptychography. The beam shows a slightly asymmetric intensity, which is switched from the bottom right corner in the upstream planes to the top left corner in the downstream planes. This is characteristic for a focused beam from KB mirrors [125]. The same distribution could also be observed at the far-field detector (Figure 6-4(b)), which was located 4 m away from the sample. Figure 6-4(c) also shows an

excellent quantitative agreement of the nanowire measurements with the ptychography along the beam axis.

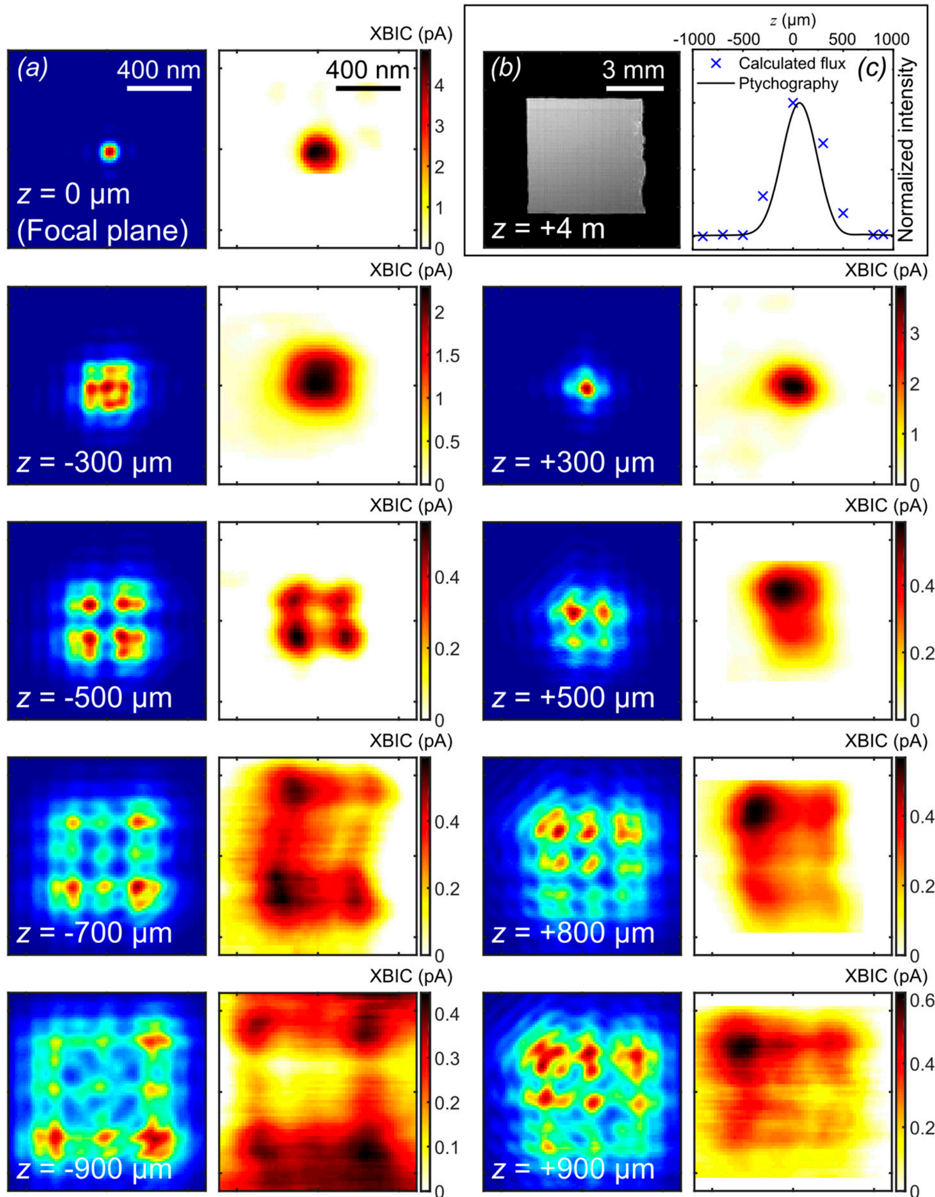

Figure 6-4 Nanofocused X-ray beam characterisation using the vertical nanowire X-ray detector. a) XBIC map (right column, hot color scale) and the calculated intensity map from the ptychography (right column, jet color scale) at the focus plane. b) The intensity of the beam detected at far-field. c) The intensity along the beam from ptychography (black line) and the calculated X-ray flux from XBIC (blue crosses). [From Paper IV]

7 Conclusion and outlook

The main question of this thesis was how NW devices could be used for high-resolution X-ray detection. Although the shape of NWs in principle forms an ideal pixel, with a small cross section for high resolution and absorption along the long axis, it is not trivial to make use of this in a real device. The X-ray microscopy technique XBIC was extensively employed to enhance the understanding of the X-ray interaction with NW devices. XBIC is an interesting method in itself, and this thesis has both improved the spatial resolution of XBIC and shown that it can quantitatively image the carrier collection of NW devices.

The use of XBIC was demonstrated in combined measurements with other X-ray imaging techniques, such as STXM, XRD, and XRF. By using nanofocused X-ray beams, the multimodal X-ray imaging could correlate various aspects of completed nanostructured devices, including morphology, crystal structure, material compositions, and local charge collection (Paper III). An example of the possible uses of multimodal X-ray imaging setup is an investigation of piezoelectric properties in nanostructure devices. Also, the electrical equipment in this setup could apply electrical bias on the devices in which the nanofocused X-ray beam probe the change in crystal structure using XRD [8].

The first experiment in this project was performed on horizontal n^+-i-n^+ doped InGaP NW devices, which is similar to the NW devices previously studied for X-ray detection [41]. An insight into the XBIC process at atomic level was given by the spectrally resolved XBIC and XRF measurements on these NW devices. Although the XBIC process involves a cascade processes to generate secondary electrons, far more complex than the XRF mechanism, the resulting XBIC and XRF spectra exhibited the same oscillation (Paper I). The spectrally resolved XBIC measurement could pave the way to measure the XAS spectrum with an electrical measurement from nanostructure devices.

The photogenerated charges from the XBIC process were trapped at surface states in the horizontal n^+-i-n^+ doped InGaP NW devices, leading to photogating and photodoping effects (section 5.3.1). This trapping also create a nonlinear XBIC signal as function of X-ray photon flux. In contrast, these effects were not observed in the *p*-*i*-*n* doped NW devices, which is an advantage over the n^+-i-n^+ doped InGaP NW devices in terms of X-ray detection.

In the XBIC measurement with moderate X-ray flux (~10^6 - 10^8 s^{-1}) on the *p-i-n* doped NW devices, the carrier generation rate was calculated to be comparable to excitation levels under one sun illumination (Paper II). The XBIC technique could be used to characterize nanostructured solar cells, just like SPCM and EBIC techniques are used in many solar cell studies. To my knowledge, there is only a simulation report on the comparison between the local charge generation using an electron beam and X-rays [95]. It is intriguing to compare the results from SPCM, EBIC, and XBIC using the same generation rate on an identical nanowire device. However, care must be taken in the comparison of these techniques, as discussed in section 3.5.1.

The bias dependent XBIC on the NW solar cells illustrates the ability of XBIC to attain the spatially dependent CCE. The results from this measurement also reveal that the charge collection region of the *p-i-n* doped NWs is bias dependent, and affected by the unintentional Zn doping in the middle segment (Paper II). The unintentional doping in the middle segment of the NW has been measured by scanning XRF in a separate work [101]. Although these measurements were performed separately on different NWs, a more precise correlation between XBIC and XRF could in principle be achieved using simultaneous XBIC and XRF measurements. A problem is that the level of X-ray flux required for a sufficient XRF emission from Zn doping can quickly degrade the electrical performance of the NW device. Subsequent measurements using low flux for XBIC followed by high flux for XRF could circumvent this problem of device degradation [97].

The spatial resolution of the XBIC method is currently limited by the X-ray optics, and could be improved, for instance, with the use of novel optics such as MZP. However, these new optics typically have very short working distances and focal depths. As shown in this thesis, this makes practical use of such optics experimentally challenging.

To take advantage of the NW geometry for the high-resolution X-ray detection, a large part of the work in this thesis was spent on developing a novel fabrication process for the vertical NW devices. Although the preliminary evaluation of the vertical NW devices reveals a low-quality photodiode, the devices can generate relatively high XBIC signals with moderate X-ray photon flux (Paper IV). In contrast to the linear relation between XBIC and X-ray flux from the horizontal *p-i-n* doped NW devices, the XBIC result from the vertical nanowire device exhibited a sub-linear behaviour. Nonetheless, the vertical NW device was able to map the intensity along the nanofocused X-ray beam with a spatial resolution that has never been demonstrated by any X-ray detector before.

An optimization of the NW synthesis is still required before further improvement of the fabrication processes. From the perspective of the device processing, proper metals for the top contact and higher doping in the *n*-segment could reduce the series

resistance. Lower X-ray absorption in the top contact could also be achieved with a thinner layer, or a lighter metal than Au.

The vertical NW device as an X-ray detector has also introduced an alternative method to characterize the nanofocused X-ray beam. This concept of the beam characterization is not only limited to the nanofocused X-ray beams. After modification with an optically transparent top contact, it could be employed to investigate transversal modes of a laser beam, for instance.

Finally, the vertical NW device developed in this thesis is possible to scale up into a multiple-pixel array detector for high-resolution X-ray microscopy. Operating as an array detector, electrical components for the readout system are required. Hence, one of the next challenges is to integrate the individual single pixels with a readout system.

8 References

1. Röntgen, W.C. On a New Kind of Rays. *Science* **1896**, *3*, 227-231.
2. Als-Nielsen, J.; McMorrow, D. *Elements of Modern X-ray Physics*, 2 ed.; Wiley: 2011; http://doi.org/10.1002/9781119998365.
3. Holler, M.; Guizar-Sicairos, M.; Tsai, E.H.R.; Dinapoli, R.; Müller, E.; Bunk, O.; Raabe, J.; Aeppli, G. High-resolution non-destructive three-dimensional imaging of integrated circuits. *Nature* **2017**, *543*, 402-406, doi:http://doi.org/10.1038/nature21698.
4. Khimchenko, A.; Bikis, C.; Pacureanu, A.; Hieber, S.E.; Thalmann, P.; Deyhle, H.; Schweighauser, G.; Hench, J.; Frank, S.; Müller-Gerbl, M., et al. Volumetric Nanoscale Imaging: Hard X-Ray Nanoholotomography: Large-Scale, Label-Free, 3D Neuroimaging beyond Optical Limit (Adv. Sci. 6/2018). *Advanced Science* **2018**, *5*, 1870036, doi:http://doi.org/10.1002/advs.201870036.
5. Diaz, A.; Mocuta, C.; Stangl, J.; Mandl, B.; David, C.; Vila-Comamala, J.; Chamard, V.; Metzger, T.H.; Bauer, G. Coherent diffraction imaging of a single epitaxial InAs nanowire using a focused x-ray beam. *Physical Review B* **2009**, *79*, 125324, doi:http://doi.org/10.1103/PhysRevB.79.125324.
6. Segura-Ruiz, J.; Martínez-Criado, G.; Chu, M.H.; Geburt, S.; Ronning, C. Nano-X-ray Absorption Spectroscopy of Single Co-Implanted ZnO Nanowires. *Nano Letters* **2011**, *11*, 5322-5326, doi:http://doi.org/10.1021/nl202799e.
7. Holt, M.; Harder, R.; Winarski, R.; Rose, V. Nanoscale Hard X-Ray Microscopy Methods for Materials Studies. *Annual Review of Materials Research* **2013**, *43*, 183-211, doi:http://doi.org/10.1146/annurev-matsci-071312-121654.
8. Wallentin, J.; Osterhoff, M.; Salditt, T. In Operando X-Ray Nanodiffraction Reveals Electrically Induced Bending and Lattice Contraction in a Single Nanowire Device. *Advanced Materials* **2016**, *28*, 1788-1792, doi:http://doi.org/10.1002/adma.201504188.
9. Johannes, A.; Salomon, D.; Martinez-Criado, G.; Glaser, M.; Lugstein, A.; Ronning, C. In operando x-ray imaging of nanoscale devices: Composition, valence, and internal electrical fields. *Science Advances* **2017**, *3*, eaao4044, doi:http://doi.org/10.1126/sciadv.aao4044.
10. Wallentin, J.; Jacobsson, D.; Osterhoff, M.; Borgström, M.T.; Salditt, T. Bending and Twisting Lattice Tilt in Strained Core–Shell Nanowires Revealed by Nanofocused X-ray Diffraction. *Nano Letters* **2017**, *17*, 4143-4150, doi:http://doi.org/10.1021/acs.nanolett.7b00918.

11. Mino, L.; Borfecchia, E.; Segura-Ruiz, J.; Giannini, C.; Martinez-Criado, G.; Lamberti, C. Materials characterization by synchrotron x-ray microprobes and nanoprobes. *Reviews of Modern Physics* **2018**, *90*, 025007, doi:http://doi.org/10.1103/RevModPhys.90.025007.
12. Mimura, H.; Handa, S.; Kimura, T.; Yumoto, H.; Yamakawa, D.; Yokoyama, H.; Matsuyama, S.; Inagaki, K.; Yamamura, K.; Sano, Y., et al. Breaking the 10-nm barrier in hard-X-ray focusing. *Nat Phys* **2010**, *6*, 122-125, doi:https://doi.org/10.1038/nphys1457.
13. Döring, F.; Robisch, A.L.; Eberl, C.; Osterhoff, M.; Ruhlandt, A.; Liese, T.; Schlenkrich, F.; Hoffmann, S.; Bartels, M.; Salditt, T., et al. Sub-5 nm hard x-ray point focusing by a combined Kirkpatrick-Baez mirror and multilayer zone plate. *Optics Express* **2013**, *21*, 19311-19323, doi:http://doi.org/10.1364/OE.21.019311.
14. Martínez-Criado, G.; Villanova, J.; Tucoulou, R.; Salomon, D.; Suuronen, J.-P.; Labouré, S.; Guilloud, C.; Valls, V.; Barrett, R.; Gagliardini, E. ID16B: a hard X-ray nanoprobe beamline at the ESRF for nano-analysis. *Journal of synchrotron radiation* **2016**, *23*, 344-352, doi:http://doi.org/10.1107/S1600577515019839.
15. Johansson, U.; Vogt, U.; Mikkelsen, A. NanoMAX: a hard x-ray nanoprobe beamline at MAX IV. In Proceedings of SPIE Optical Engineering + Applications, San Diego, California, United States.
16. Björling, A.; Kalbfleisch, S.; Kahnt, M.; Sala, S.; Parfeniukas, K.; Vogt, U.; Carbone, D.; Johansson, U. Ptychographic characterization of a coherent nanofocused X-ray beam. *Optics Express* **2020**, *28*, 5069-5076, doi:http://doi.org/10.1364/OE.386068.
17. Stampanoni, M.; Borchert, G.; Wyss, P.; Abela, R.; Patterson, B.; Hunt, S.; Vermeulen, D.; Rüegsegger, P. High resolution X-ray detector for synchrotron-based microtomography. *Nuclear Instruments and Methods in Physics Research Section A: Accelerators, Spectrometers, Detectors and Associated Equipment* **2002**, *491*, 291-301, doi:https://doi.org/10.1016/S0168-9002(02)01167-1.
18. Dinapoli, R.; Bergamaschi, A.; Henrich, B.; Horisberger, R.; Johnson, I.; Mozzanica, A.; Schmid, E.; Schmitt, B.; Schreiber, A.; Shi, X., et al. EIGER: Next generation single photon counting detector for X-ray applications. *Nuclear Instruments and Methods in Physics Research Section A: Accelerators, Spectrometers, Detectors and Associated Equipment* **2011**, *650*, 79-83, doi:https://doi.org/10.1016/j.nima.2010.12.005.
19. Henrich, B.; Becker, J.; Dinapoli, R.; Goettlicher, P.; Graafsma, H.; Hirsemann, H.; Klanner, R.; Krueger, H.; Mazzocco, R.; Mozzanica, A., et al. The adaptive gain integrating pixel detector AGIPD a detector for the European XFEL. *Nuclear Instruments and Methods in Physics Research Section A: Accelerators, Spectrometers, Detectors and Associated Equipment* **2011**, *633*, S11-S14, doi:https://doi.org/10.1016/j.nima.2010.06.107.
20. Ballabriga, R.; Alozy, J.; Blaj, G.; Campbell, M.; Fiederle, M.; Frojdh, E.; Heijne, E.H.M.; Llopart, X.; Pichotka, M.; Procz, S., et al. The Medipix3RX: a high resolution, zero dead-time pixel detector readout chip allowing spectroscopic imaging. *Journal of Instrumentation* **2013**, *8*, C02016-C02016, doi:http://dx.doi.org/10.1088/1748-0221/8/02/C02016.

21. Ramdani, M.R.; Gil, E.; Leroux, C.; André, Y.; Trassoudaine, A.; Castelluci, D.; Bideux, L.; Monier, G.; Robert-Goumet, C.; Kupka, R. Fast Growth Synthesis of GaAs Nanowires with Exceptional Length. *Nano Letters* **2010**, *10*, 1836-1841, doi:http://doi.org/10.1021/nl100557d.
22. Qu, Y.; Duan, X. One-dimensional homogeneous and heterogeneous nanowires for solar energy conversion. *Journal of Materials Chemistry* **2012**, *22*, 16171-16181, doi:http://doi.org/10.1039/C2JM32267F.
23. Zeng, X.; Otnes, G.; Heurlin, M.; Mourão, R.T.; Borgström, M.T. InP/GaInP nanowire tunnel diodes. *Nano Research* **2017**, *11*, 2523–2531, doi:http://doi.org/10.1007/s12274-017-1877-8.
24. Leandro, L.; Gunnarsson, C.P.; Reznik, R.; Jöns, K.D.; Shtrom, I.; Khrebtov, A.; Kasama, T.; Zwiller, V.; Cirlin, G.; Akopian, N. Nanowire Quantum Dots Tuned to Atomic Resonances. *Nano Letters* **2018**, *18*, 7217-7221, doi:http://doi.org/10.1021/acs.nanolett.8b03363.
25. Nylund, G.; Storm, K.; Torstensson, H.; Wallentin, J.; Borgström, M.T.; Hessman, D.; Samuelson, L. Transparently wrap-gated semiconductor nanowire arrays for studies of gate-controlled photoluminescence. *AIP Conference Proceedings* **2013**, *1566*, 427-428, doi:http://doi.org/10.1063/1.4848468.
26. Kivisaari, P.; Berg, A.; Karimi, M.; Storm, K.; Limpert, S.; Oksanen, J.; Samuelson, L.; Pettersson, H.; Borgström, M.T. Optimization of Current Injection in AlGaInP Core−Shell Nanowire Light-Emitting Diodes. *Nano Letters* **2017**, *17*, 3599-3606, doi:http://doi.org/10.1021/acs.nanolett.7b00759.
27. Bryllert, T.; Wernersson, L.E.; Froberg, L.E.; Samuelson, L. Vertical high-mobility wrap-gated InAs nanowire transistor. *IEEE Electron Device Letters* **2006**, *27*, 323-325, doi:http://doi.org/10.1109/LED.2006.873371.
28. Yang, B.; Buddharaju, K.D.; Teo, S.H.G.; Singh, N.; Lo, G.Q.; Kwong, D.L. Vertical Silicon-Nanowire Formation and Gate-All-Around MOSFET. *IEEE Electron Device Letters* **2008**, *29*, 791-794, doi:http://doi.org/10.1109/LED.2008.2000617.
29. Wallentin, J.; Ek, M.; Wallenberg, L.R.; Samuelson, L.; Borgström, M.T. Electron Trapping in InP Nanowire FETs with Stacking Faults. *Nano Letters* **2012**, *12*, 151-155, doi:http://doi.org/10.1021/nl203213d.
30. Maslov, A.V.; Ning, C.Z. Reflection of guided modes in a semiconductor nanowire laser. *Applied Physics Letters* **2003**, *83*, 1237-1239, doi:http://doi.org/10.1063/1.1599037.
31. Greytak, A.B.; Barrelet, C.J.; Li, Y.; Lieber, C.M. Semiconductor nanowire laser and nanowire waveguide electro-optic modulators. *Applied Physics Letters* **2005**, *87*, 151103, doi:http://doi.org/10.1063/1.2089157.
32. Pettersson, H.; Zubritskaya, I.; Nghia, N.T.; Wallentin, J.; Borgström, M.T.; Storm, K.; Landin, L.; Wickert, P.; Capasso, F.; Samuelson, L. Electrical and optical properties of InP nanowire ensemble p + –i–n + photodetectors. *Nanotechnology* **2012**, *23*, 135201, doi:https://doi.org/10.1088/0957-4484/23/13/135201.

33. Jain, V.; Nowzari, A.; Wallentin, J.; Borgström, M.T.; Messing, M.E.; Asoli, D.; Graczyk, M.; Witzigmann, B.; Capasso, F.; Samuelson, L., et al. Study of photocurrent generation in InP nanowire-based p+-i-n+ photodetectors. *Nano Research* **2014**, *7*, 544-552, doi:http://doi.org/10.1007/s12274-014-0422-2.
34. Gibson, S.J.; van Kasteren, B.; Tekcan, B.; Cui, Y.; van Dam, D.; Haverkort, J.E.M.; Bakkers, E.P.A.M.; Reimer, M.E. Tapered InP nanowire arrays for efficient broadband high-speed single-photon detection. *Nature Nanotechnology* **2019**, *14*, 473-479, doi:http://doi.org/10.1038/s41565-019-0393-2.
35. Christesen, J.D.; Zhang, X.; Pinion, C.W.; Celano, T.A.; Flynn, C.J.; Cahoon, J.F. Design Principles for Photovoltaic Devices Based on Si Nanowires with Axial or Radial p–n Junctions. *Nano Letters* **2012**, *12*, 6024-6029, doi:http://doi.org/10.1021/nl303610m.
36. Yao, M.; Huang, N.; Cong, S.; Chi, C.-Y.; Seyedi, M.A.; Lin, Y.-T.; Cao, Y.; Povinelli, M.L.; Dapkus, P.D.; Zhou, C. GaAs Nanowire Array Solar Cells with Axial p–i–n Junctions. *Nano Letters* **2014**, *14*, 3293-3303, doi:http://doi.org/10.1021/nl500704r.
37. Zhong, Z.; Li, Z.; Gao, Q.; Li, Z.; Peng, K.; Li, L.; Mokkapati, S.; Vora, K.; Wu, J.; Zhang, G., et al. Efficiency enhancement of axial junction InP single nanowire solar cells by dielectric coating. *Nano Energy* **2016**, *28*, 106-114, doi:http://dx.doi.org/10.1016/j.nanoen.2016.08.032.
38. Gao, Q.; Li, Z.; Li, L.; Vora, K.; Li, Z.; Alabadla, A.; Wang, F.; Guo, Y.; Peng, K.; Wenas, Y.C., et al. Axial p-n junction design and characterization for InP nanowire array solar cells. *Progress in Photovoltaics: Research and Applications* **2019**, *27*, 237-244, doi:http://doi.org/10.1002/pip.3083.
39. Hieslmair, H.; Istratov, A.A.; Sachdeva, R.; Weber, E.R. *New synchrotron-radiation based technique to study localized defects in silicon: 'EBIC' with X-ray excitation*; LBNL/ALS--43453; United States, 2000.
40. Vyvenko, O.F.; Buonassisi, T.; Istratov, A.A.; Weber, E.R. X-ray beam induced current/microprobe x-ray fluorescence: synchrotron radiation based x-ray microprobe techniques for analysis of the recombination activity and chemical nature of metal impurities in silicon. *Journal of Physics: Condensed Matter* **2004**, *16*, S141, doi:https://doi.org/10.1088/0953-8984/16/2/017.
41. Wallentin, J.; Osterhoff, M.; Wilke, R.N.; Persson, K.-M.; Wernersson, L.-E.; Sprung, M.; Salditt, T. Hard X-ray Detection Using a Single 100 nm Diameter Nanowire. *Nano Letters* **2014**, *14*, 7071-7076, doi:https://doi.org/10.1021/nl5040545.
42. Zapf, M.; Ritzer, M.; Liborius, L.; Johannes, A.; Hafermann, M.; Schönherr, S.; Segura-Ruiz, J.; Martínez-Criado, G.; Prost, W.; Ronning, C. Hot electrons in a nanowire hard X-ray detector. *Nature Communications* **2020**, *11*, 4729, doi:http://doi.org/10.1038/s41467-020-18384-x.
43. Buonassisi, T.; Heuer, M.; Vyvenko, O.F.; Istratov, A.A.; Weber, E.R.; Cai, Z.; Lai, B.; Ciszek, T.F.; Schindler, R. Applications of synchrotron radiation X-ray techniques on the analysis of the behavior of transition metals in solar cells and single-crystalline silicon with extended defects. *Physica B: Condensed Matter* **2003**, *340-342*, 1137-1141, doi:https://doi.org/10.1016/j.physb.2003.09.099.

44. Buonassisi, T.; Istratov, A.A.; Pickett, M.D.; Marcus, M.A.; Hahn, G.; Riepe, S.; Isenberg, J.; Warta, W.; Willeke, G.; Ciszek, T.F., et al. Quantifying the effect of metal-rich precipitates on minority carrier diffusion length in multicrystalline silicon using synchrotron-based spectrally resolved x-ray beam-induced current. *Applied Physics Letters* **2005**, *87*, 044101, doi:http://doi.org/10.1063/1.1997274.
45. Seifert, W.; Vyvenko, O.; Arguirov, T.; Kittler, M.; Salome, M.; Seibt, M.; Trushin, M. Synchrotron-based investigation of iron precipitation in multicrystalline silicon. *Superlattices and Microstructures* **2009**, *45*, 168-176, doi:https://doi.org/10.1016/j.spmi.2008.11.025.
46. Soci, C.; Zhang, A.; Xiang, B.; Dayeh, S.A.; Aplin, D.P.R.; Park, J.; Bao, X.Y.; Lo, Y.H.; Wang, D. ZnO Nanowire UV Photodetectors with High Internal Gain. *Nano Letters* **2007**, *7*, 1003-1009, doi:http://doi.org/10.1021/nl070111x.
47. Bambynek, W.; Crasemann, B.; Fink, R.W.; Freund, H.U.; Mark, H.; Swift, C.D.; Price, R.E.; Rao, P.V. X-Ray Fluorescence Yields, Auger, and Coster-Kronig Transition Probabilities. *Reviews of Modern Physics* **1972**, *44*, 716-813, doi:http://doi.org/10.1103/RevModPhys.44.716.
48. Thompson, A.; Attwood, D.; Gullikson, E.; Howells, M.; Kortright, J.; Robinson, A. X-ray data booklet (2009). **2009**.
49. Hayashi, K.; Kawai, J.; Awakura, Y. Extended fine structure in characteristic X-ray fluorescence: A novel structural analysis method of condensed systems. *Spectrochimica Acta Part B: Atomic Spectroscopy* **1997**, *52*, 2169-2172, doi:https://doi.org/10.1016/S0584-8547(97)00097-9.
50. Rodnyi, P.A. *Physical processes in inorganic scintillators*; CRC press: 1997; Vol. 14.
51. Nikl, M. Scintillation detectors for x-rays. *Measurement Science and Technology* **2006**, *17*, R37-R54, doi:http://doi.org/10.1088/0957-0233/17/4/r01.
52. Lecoq, P.; Gektin, A.; Korzhik, M. *Inorganic scintillators for detector systems: physical principles and crystal engineering*; Springer: 2016.
53. Alig, R.C.; Bloom, S. Secondary-electron-escape probabilities. *Journal of Applied Physics* **1978**, *49*, 3476-3480, doi:http://doi.org/10.1063/1.325257.
54. Sze, S.M. *Semiconductor Devices: Physics and Technology*, 3 ed.; John Wiley & Sons Singapore Pte. Limited: 2012.
55. Martínez-Criado, G.; Homs, A.; Alén, B.; Sans, J.A.; Segura-Ruiz, J.; Molina-Sánchez, A.; Susini, J.; Yoo, J.; Yi, G.-C. Probing Quantum Confinement within Single Core–Multishell Nanowires. *Nano Letters* **2012**, *12*, 5829-5834, doi:http://doi.org/10.1021/nl303178u.
56. Smit, G.D.J.; Rogge, S.; Klapwijk, T.M. Scaling of nano-Schottky-diodes. *Applied Physics Letters* **2002**, *81*, 3852-3854, doi:http://doi.org/10.1063/1.1521251.
57. Gutsche, C.; Lysov, A.; Regolin, I.; Münstermann, B.; Prost, W.; Tegude, F.J. Scalable Electrical Properties of Axial GaAs Nanowire pn-Diodes. *Journal of Electronic Materials* **2012**, *41*, 809-812, doi:http://doi.org/10.1007/s11664-011-1824-5.
58. Calarco, R.; Stoica, T.; Brandt, O.; Geelhaar, L. Surface-induced effects in GaN nanowires. *Journal of Materials Research* **2011**, *26*, 2157-2168, doi:http://doi.org/10.1557/jmr.2011.211.

59. Weert, M.H.M.v.; Wunnicke, O.; Roest, A.L.; Eijkemans, T.J.; Silov, A.Y.; Haverkort, J.E.M.; Hooft, G.W.t.; Bakkers, E.P.A.M. Large redshift in photoluminescence of p-doped InP nanowires induced by Fermi-level pinning. *Applied Physics Letters* **2006**, *88*, 043109, doi:http://doi.org/10.1063/1.2168255.
60. Saleh, B.E.A.; Teich, M.C.; Teich, M.C. *Fundamentals of Photonics*; John Wiley & Sons, Incorporated: Somerset, UNITED STATES, 2013.
61. Sah, C.; Noyce, R.N.; Shockley, W. Carrier Generation and Recombination in P-N Junctions and P-N Junction Characteristics. *Proceedings of the IRE* **1957**, *45*, 1228-1243, doi:http://doi.org/10.1109/JRPROC.1957.278528.
62. Stuckelberger, M.; West, B.; Nietzold, T.; Lai, B.; Maser, J.M.; Rose, V.; Bertoni, M.I. Engineering solar cells based on correlative X-ray microscopy. *Journal of Materials Research* **2017**, *32*, 1825-1854, doi:http://doi.org/10.1557/jmr.2017.108.
63. Martin, T.; Koch, A. Recent developments in X-ray imaging with micrometer spatial resolution. *Journal of Synchrotron Radiation* **2006**, *13*, 180-194, doi:http://doi.org/10.1107/S0909049506000550.
64. Gruner, S.M. Synchrotron Area X-ray Detectors, Present and Future. *AIP Conference Proceedings* **2010**, *1234*, 69-72, doi:http://doi.org/10.1063/1.3463304.
65. Kamehama, H.; Kawahito, S.; Shrestha, S.; Nakanishi, S.; Yasutomi, K.; Takeda, A.; Tsuru, T.G.; Arai, Y. A low-noise X-ray astronomical silicon-on-insulator pixel detector using a pinned depleted diode structure. *Sensors* **2018**, *18*, 27, doi:http://doi.org/10.3390/s18010027.
66. Yan, X.; Li, B.; Wu, Y.; Zhang, X.; Ren, X. A single crystalline InP nanowire photodetector. *Applied Physics Letters* **2016**, *109*, 053109, doi:http://doi.org/10.1063/1.4960713.
67. Borgström, M.T.; Norberg, E.; Wickert, P.; Nilsson, H.A.; Trägårdh, J.; Dick, K.A.; Statkute, G.; Ramvall, P.; Deppert, K.; Samuelson, L. Precursor evaluation for in situ InP nanowire doping. *Nanotechnology* **2008**, *19*, 445602, doi:https://doi.org/10.1088/0957-4484/19/44/445602.
68. Borgström, M.T.; Wallentin, J.; Heurlin, M.; Fält, S.; Wickert, P.; Leene, J.; Magnusson, M.H.; Deppert, K.; Samuelson, L. Nanowires with promise for photovoltaics. *Ieee Journal of selected topics in quantum electronics* **2011**, *17*, 1050-1061, doi:http://doi.org/10.1109/JSTQE.2010.2073681.
69. Wallentin, J.; Borgström, M.T. Doping of semiconductor nanowires. *Journal of Materials Research* **2011**, *26*, 2142-2156, doi:http://doi.org/10.1557/jmr.2011.214.
70. Heurlin, M.; Anttu, N.; Camus, C.; Samuelson, L.; Borgström, M.T. In Situ Characterization of Nanowire Dimensions and Growth Dynamics by Optical Reflectance. *Nano Letters* **2015**, *15*, 3597-3602, doi:http://doi.org/10.1021/acs.nanolett.5b01107.
71. Otnes, G.; Borgström, M.T. Towards high efficiency nanowire solar cells. *Nano Today* **2017**, *12*, 31-45, doi:https://doi.org/10.1016/j.nantod.2016.10.007.
72. Dagytė, V.; Heurlin, M.; Zeng, X.; Borgström, M.T. Growth kinetics of Ga x In(1−x)P nanowires using triethylgallium as Ga precursor. *Nanotechnology* **2018**, *29*, 394001, doi:http://doi.org/10.1088/1361-6528/aad1d2.

73. Wallentin, J.; Anttu, N.; Asoli, D.; Huffman, M.; Åberg, I.; Magnusson, M.H.; Siefer, G.; Fuss-Kailuweit, P.; Dimroth, F.; Witzigmann, B., et al. InP Nanowire Array Solar Cells Achieving 13.8% Efficiency by Exceeding the Ray Optics Limit. *Science* **2013**, *339*, 1057-1060, doi:http://doi.org/10.1126/science.1230969.
74. Otnes, G.; Heurlin, M.; Graczyk, M.; Wallentin, J.; Jacobsson, D.; Berg, A.; Maximov, I.; Borgström, M.T. Strategies to obtain pattern fidelity in nanowire growth from large-area surfaces patterned using nanoimprint lithography. *Nano Research* **2016**, *9*, 2852-2861, doi:http://doi.org/10.1007/s12274-016-1165-z.
75. Otnes, G.; Barrigón, E.; Sundvall, C.; Svensson, K.E.; Heurlin, M.; Siefer, G.; Samuelson, L.; Åberg, I.; Borgström, M.T. Understanding InP Nanowire Array Solar Cell Performance by Nanoprobe-Enabled Single Nanowire Measurements. *Nano Letters* **2018**, *18*, 3038-3046, doi:http://doi.org/10.1021/acs.nanolett.8b00494.
76. Borgström, M.T.; Wallentin, J.; Trägårdh, J.; Ramvall, P.; Ek, M.; Wallenberg, L.R.; Samuelson, L.; Deppert, K. In situ etching for total control over axial and radial nanowire growth. *Nano Research* **2010**, *3*, 264-270, doi:http://doi.org/10.1007/s12274-010-1029-x.
77. Wallentin, J.; Wickert, P.; Ek, M.; Gustafsson, A.; Reine Wallenberg, L.; Magnusson, M.H.; Samuelson, L.; Deppert, K.; Borgström, M.T. Degenerate p-doping of InP nanowires for large area tunnel diodes. *Applied Physics Letters* **2011**, *99*, 253105, doi:http://doi.org/10.1063/1.3669697.
78. Otnes, G.; Heurlin, M.; Zeng, X.; Borgström, M.T. InxGa1–xP Nanowire Growth Dynamics Strongly Affected by Doping Using Diethylzinc. *Nano Letters* **2017**, *17*, 702-707, doi:http://doi.org/10.1021/acs.nanolett.6b03795.
79. Björk, M.T.; Ohlsson, B.J.; Sass, T.; Persson, A.I.; Thelander, C.; Magnusson, M.H.; Deppert, K.; Wallenberg, L.R.; Samuelson, L. One-dimensional heterostructures in semiconductor nanowhiskers. *Applied Physics Letters* **2002**, *80*, 1058-1060, doi:http://doi.org/10.1063/1.1447312.
80. Lorek, E. Electron Beam Lithography on Ultra-thin Silicon Nitride Membranes-Target Manufacturing for Digital Holography. *Lund Reports in Atomic Physics* **2010**.
81. Bruce, R.; Clark, D.; Eicher, S. Low resistance Pd/Zn/Pd Au ohmic contacts to P-type gaas. *Journal of Electronic Materials* **1990**, *19*, 225-229, doi:http://doi.org/10.1007/bf02733810.
82. Rodenburg, J.M. Ptychography and Related Diffractive Imaging Methods. In *Advances in Imaging and Electron Physics*, Elsevier: 2008; Vol. 150, pp. 87-184.
83. Koutsonikolas, D.E.; Kaldis, S.P.; Pantoleontos, G.T. Chapter 3 - Preparation of Silica Membranes by Atomic Layer Deposition. In *Current Trends and Future Developments on (Bio-) Membranes*, Basile, A., Ghasemzadeh, K., Eds. Elsevier: 2017; https://doi.org/10.1016/B978-0-444-63866-3.00003-0pp. 45-62.
84. Johnson, R.W.; Hultqvist, A.; Bent, S.F. A brief review of atomic layer deposition: from fundamentals to applications. *Materials Today* **2014**, *17*, 236-246, doi:https://doi.org/10.1016/j.mattod.2014.04.026.
85. Ni, G.; Han, B.; Cheng, H. Effect of Al Electronic Configuration on the SiO2 Thin Film Growth via Catalytic Self-Assembling Deposition. *The Journal of Physical Chemistry C* **2013**, *117*, 22705-22713, doi:http://doi.org/10.1021/jp405847r.

86. Barrigon, E.; Otnes, G.; Chen, Y.; Zhang, Y.; Hrachowina, L.; Zeng, X.; Samuelson, L.; Borgström, M. Nanoprobe-Enabled Electron Beam Induced Current Measurements on III-V Nanowire-Based Solar Cells. In Proceedings of 2019 IEEE 46th Photovoltaic Specialists Conference (PVSC), 16-21 June 2019; pp. 2730-2733.
87. Timm, R.; Persson, O.; Engberg, D.L.J.; Fian, A.; Webb, J.L.; Wallentin, J.; Jönsson, A.; Borgström, M.T.; Samuelson, L.; Mikkelsen, A. Current–Voltage Characterization of Individual As-Grown Nanowires Using a Scanning Tunneling Microscope. *Nano Letters* **2013**, *13*, 5182-5189, doi:http://doi.org/10.1021/nl402570u.
88. Peelaers, H.; Partoens, B.; Peeters, F.M. Formation and Segregation Energies of B and P Doped and BP Codoped Silicon Nanowires. *Nano Letters* **2006**, *6*, 2781-2784, doi:http://doi.org/10.1021/nl061811p.
89. Fernández-Serra, M.V.; Adessi, C.; Blase, X. Surface Segregation and Backscattering in Doped Silicon Nanowires. *Physical Review Letters* **2006**, *96*, 166805, doi:http://doi.org/10.1103/PhysRevLett.96.166805.
90. Ahn, Y.H.; Tsen, A.W.; Kim, B.; Park, Y.W.; Park, J. Photocurrent Imaging of p−n Junctions in Ambipolar Carbon Nanotube Transistors. *Nano Letters* **2007**, *7*, 3320-3323, doi:http://doi.org/10.1021/nl071536m.
91. Lysov, A.; Vinaji, S.; Offer, M.; Gutsche, C.; Regolin, I.; Mertin, W.; Geller, M.; Prost, W.; Bacher, G.; Tegude, F.-J. Spatially resolved photoelectric performance of axial GaAs nanowire pn-diodes. *Nano Research* **2011**, *4*, 987-995, doi:http://doi.org/10.1007/s12274-011-0155-4.
92. Gu, Y.; Kwak, E.-S.; Lensch, J.L.; Allen, J.E.; Odom, T.W.; Lauhon, L.J. Near-field scanning photocurrent microscopy of a nanowire photodetector. *Applied Physics Letters* **2005**, *87*, 043111, doi:http://doi.org/10.1063/1.1996851.
93. Shi-Qiu, Z.; Rau, E.I.; Fu-Hua, Y. A novel method of determining semiconductor parameters in EBIC and SEBIV modes of SEM. *Semiconductor Science and Technology* **2003**, *18*, 361, doi:https://doi.org/10.1088/0268-1242/18/4/329.
94. Ong, V.K.S.; Wu, D. Determination of diffusion length from within a confined region with the use of EBIC. *IEEE Transactions on Electron Devices* **2001**, *48*, 332-337, doi:http://doi.org/10.1109/16.902735.
95. Stuckelberger, M.; West, B.; Husein, S.; Guthrey, H.; Al-Jassim, M.; Chakraborty, R.; Buonassisi, T.; Maser, J.M.; Lai, B.; Stripe, B. Latest developments in the x-ray based characterization of thin-film solar cells. In Proceedings of Photovoltaic Specialist Conference (PVSC); pp. 1-6.
96. West, B.; Husein, S.; Stuckelberger, M.; Lai, B.; Maser, J.; Stripe, B.; Rose, V.; Guthrey, H.; Al-Jassim, M.; Bertoni, M. Correlation between grain composition and charge carrier collection in Cu(In,Ga)Se2 solar cells. In Proceedings of 2015 IEEE 42nd Photovoltaic Specialist Conference (PVSC), 14-19 June 2015; pp. 1-4.
97. Stuckelberger, M.; Nietzold, T.; Hall, G.N.; West, B.; Werner, J.; Niesen, B.; Ballif, C.; Rose, V.; Fenning, D.P.; Bertoni, M.I. Elemental distribution and charge collection at the nanoscale on perovskite solar cells. In Proceedings of 2016 IEEE 43rd Photovoltaic Specialists Conference (PVSC), 5-10 June 2016; pp. 1191-1196.

98. Ossig, C.; Nietzold, T.; West, B.; Bertoni, M.; Falkenberg, G.; Schroer, C.G.; Stuckelberger, M.E. X-ray Beam Induced Current Measurements for Multi-Modal X-ray Microscopy of Solar Cells. *Journal of visualized experiments* **2019**, *150*, e60001, doi:http://doi.org/10.3791/60001.
99. Bunk, O.; Bech, M.; Jensen, T.H.; Feidenhans'l, R.; Binderup, T.; Menzel, A.; Pfeiffer, F. Multimodal x-ray scatter imaging. *New Journal of Physics* **2009**, *11*, 123016, doi:http://doi.org/10.1088/1367-2630/11/12/123016.
100. Solé, V.A.; Papillon, E.; Cotte, M.; Walter, P.; Susini, J. A multiplatform code for the analysis of energy-dispersive X-ray fluorescence spectra. *Spectrochimica Acta Part B: Atomic Spectroscopy* **2007**, *62*, 63-68, doi:https://doi.org/10.1016/j.sab.2006.12.002.
101. Troian, A.; Otnes, G.; Zeng, X.; Chayanun, L.; Dagytė, V.; Hammarberg, S.; Salomon, D.; Timm, R.; Mikkelsen, A.; Borgström, M.T., et al. Nanobeam X-ray Fluorescence Dopant Mapping Reveals Dynamics of in Situ Zn-Doping in Nanowires. *Nano Letters* **2018**, *18*, 6461-6468, doi:http://doi.org/10.1021/acs.nanolett.8b02957.
102. Miao, J.; Ishikawa, T.; Robinson, I.K.; Murnane, M.M. Beyond crystallography: Diffractive imaging using coherent x-ray light sources. *Science* **2015**, *348*, 530-535, doi:http://doi.org/10.1126/science.aaa1394.
103. Lazarev, S.; Dzhigaev, D.; Bi, Z.; Nowzari, A.; Kim, Y.Y.; Rose, M.; Zaluzhnyy, I.A.; Gorobtsov, O.Y.; Zozulya, A.V.; Lenrick, F., et al. Structural Changes in a Single GaN Nanowire under Applied Voltage Bias. *Nano Letters* **2018**, *18*, 5446-5452, doi:http://doi.org/10.1021/acs.nanolett.8b01802.
104. Eymery, J.; Rieutord, F.; Favre-Nicolin, V.; Robach, O.; Niquet, Y.-M.; Fröberg, L.; Mårtensson, T.; Samuelson, L. Strain and Shape of Epitaxial InAs/InP Nanowire Superlattice Measured by Grazing Incidence X-ray Techniques. *Nano Letters* **2007**, *7*, 2596-2601, doi:http://doi.org/10.1021/nl070888q.
105. Newton, M.C.; Leake, S.J.; Harder, R.; Robinson, I.K. Three-dimensional imaging of strain in a single ZnO nanorod. *Nature Materials* **2009**, *9*, 120, doi:http://doi.org/10.1038/nmat2607.
106. Favre-Nicolin, V.; Mastropietro, F.; Eymery, J.; Camacho, D.; Niquet, Y.M.; Borg, B.M.; Messing, M.E.; Wernersson, L.E.; Algra, R.E.; Bakkers, E.P.A.M., et al. Analysis of strain and stacking faults in single nanowires using Bragg coherent diffraction imaging. *New Journal of Physics* **2010**, *12*, 035013, doi:http://doi.org/10.1088/1367-2630/12/3/035013.
107. Haag, S.T.; Richard, M.-I.; Welzel, U.; Favre-Nicolin, V.; Balmes, O.; Richter, G.; Mittemeijer, E.J.; Thomas, O. Concentration and Strain Fields inside a Ag/Au Core–Shell Nanowire Studied by Coherent X-ray Diffraction. *Nano Letters* **2013**, *13*, 1883-1889, doi:http://doi.org/10.1021/nl303206u.
108. Stankevič, T.; Mickevičius, S.; Schou Nielsen, M.; Kryliouk, O.; Ciechonski, R.; Vescovi, G.; Bi, Z.; Mikkelsen, A.; Samuelson, L.; Gundlach, C. Measurement of strain in InGaN/GaN nanowires and nanopyramids. *Journal of Applied Crystallography* **2015**, *48*, 344-349, doi:http://doi.org/10.1107/S1600576715000965.

109. Hammarberg, S.; Dagytė, V.; Chayanun, L.; Hill, M.O.; Wyke, A.; Björling, A.; Johansson, U.; Kalbfleisch, S.; Heurlin, M.; Lauhon, L.J., et al. High resolution strain mapping of a single axially heterostructured nanowire using scanning X-ray diffraction. *Nano Research* **2020**, *13*, 2460–2468, doi:http://doi.org/10.1007/s12274-020-2878-6.
110. Haensel, R. European Synchrotron Radiation Facility (ESRF). *Review of Scientific Instruments* **1992**, *63*, 1571-1572, doi:http://doi.org/10.1063/1.1143024.
111. Eriksson, M.; Malmgren, L.; Al-Dmour, E.; Thorin, S.; Johansson, M.; Leemann, S.; Andersson, Å.; Tavares, P. Commissioning of the MAX IV light source. In Proceedings of 7th International Particle Accelerator Conference, IPAC 2016, Busan, Korea; pp. 11-15.
112. Osterhoff, M.; Krebs, H.-U. Multilayer Zone Plates for Hard X-ray Imaging. In *Nanoscale Photonic Imaging*, Salditt, T., Egner, A., Luke, D.R., Eds. Springer International Publishing: 2020; Vol. 134, pp. 561-581.
113. Zienkiewicz, O.C.; Taylor, R.L.; Zhu, J.Z. Chapter 1 - The Standard Discrete System and Origins of the Finite Element Method. In *The Finite Element Method: its Basis and Fundamentals*, 7 ed.; Zienkiewicz, O.C., Taylor, R.L., Zhu, J.Z., Eds. Butterworth-Heinemann: Oxford, 2013; pp. 1-20.
114. Whiteley, J. Finite Element Methods. *A Practical Guide* **2014**, *1*, doi:https://doi.org/10.1007/978-3-319-49971-0.
115. Wallander, H.; Wallentin, J. Simulated sample heating from a nanofocused X-ray beam. *Journal of synchrotron radiation* **2017**, *24*, 925-933, doi:http://doi.org/10.1107/S1600577517008712.
116. Gutsche, C.; Niepelt, R.; Gnauck, M.; Lysov, A.; Prost, W.; Ronning, C.; Tegude, F.-J. Direct Determination of Minority Carrier Diffusion Lengths at Axial GaAs Nanowire p–n Junctions. *Nano Letters* **2012**, *12*, 1453-1458, doi:http://doi.org/10.1021/nl204126n.
117. Mohite, A.D.; Perea, D.E.; Singh, S.; Dayeh, S.A.; Campbell, I.H.; Picraux, S.T.; Htoon, H. Highly Efficient Charge Separation and Collection across in Situ Doped Axial VLS-Grown Si Nanowire p–n Junctions. *Nano Letters* **2012**, *12*, 1965-1971, doi:http://doi.org/10.1021/nl204505p.
118. Dalba, G.; Diop, D.; Fornasini, P.; Kuzmin, A.; Rocca, F. EXAFS and XANES study of GaAs on Ga and As K edges. *Journal of Physics: Condensed Matter* **1993**, *5*, 1643, doi:https://doi.org/10.1088/0953-8984/5/11/005.
119. Nishi, K.; Shimizu, K.-i.; Takamatsu, M.; Yoshida, H.; Satsuma, A.; Tanaka, T.; Yoshida, S.; Hattori, T. Deconvolution Analysis of Ga K-Edge XANES for Quantification of Gallium Coordinations in Oxide Environments. *The Journal of Physical Chemistry B* **1998**, *102*, 10190-10195, doi:http://doi.org/10.1021/jp982704p.
120. Perlin, P.; Jauberthie-Carillon, C.; Itie, J.P.; San Miguel, A.; Grzegory, I.; Polian, A. Raman scattering and x-ray-absorption spectroscopy in gallium nitride under high pressure. *Physical Review B* **1992**, *45*, 83-89, doi:https://doi.org/10.1103/PhysRevB.45.83.

121. Chen, Y.; Kivisaari, P.; Pistol, M.-E.; Anttu, N. Optimization of the short-circuit current in an InP nanowire array solar cell through opto-electronic modeling. *Nanotechnology* **2016**, *27*, 435404, doi:https://doi.org/10.1088/0957-4484/27/43/435404.
122. Liu, A.; Rosenwaks, Y. Excess carriers lifetime in InP single crystals: Radiative versus nonradiative recombination. *Journal of Applied Physics* **1999**, *86*, 430-437, doi:http://doi.org/10.1063/1.370748.
123. Schroder, D.K. Carrier Lifetimes. In *Semiconductor Material and Device Characterization*, Schroder, D.K., Ed. John Wiley & Sons, Inc.: 2005; pp. 389-464.
124. Walker, A.W.; Heckelmann, S.; Karcher, C.; Höhn, O.; Went, C.; Niemeyer, M.; Bett, A.W.; Lackner, D. Nonradiative lifetime extraction using power-dependent relative photoluminescence of III-V semiconductor double-heterostructures. *Journal of Applied Physics* **2016**, *119*, 155702, doi:http://doi.org/10.1063/1.4945772.
125. Mimura, H.; Matsuyama, S.; Yumoto, H.; Hara, H.; Yamamura, K.; Sano, Y.; Shibahara, M.; Endo, K.; Mori, Y.; Nishino, Y., et al. Hard X-ray Diffraction-Limited Nanofocusing with Kirkpatrick-Baez Mirrors. *Japanese Journal of Applied Physics* **2005**, *44*, L539-L542, doi:http://doi.org/10.1143/jjap.44.l539.